3. Sesamol-derived O-acetamides & extended carbohydrazones: design, synthesis and biological evaluation as dual MAO and AChE inhibitors

3.1. Rationale, objectives and plan of work

3.1.1. Rationale

Molecules containing 1,3-benzodioxole scaffold have been documented as potential neuroprotective, antioxidant agents and MAO and AChE inhibitors (compounds **I**, **Figure 3.1**) [73, 100-102, 181]. Several 1,3-benzodioxole-bearing molecules of natural origin have been reported as inhibitors of MAO and AChE (e.g., piperine and avicine) [31-34]. Considering the benzodioxole scaffold's multifunctional and neuroprotective potential, we designed a new set of sesamol-derived acetamides using a molecular hybridization approach (**Figure 3.1**). The 4-atom carbohydrazone (-CO-NH-N=C<) of compound **I** was replaced with a 4-atom oxy acetamide (-O-CH_2-CO-NH-) linker (compounds **SMA01-SMA11**) to investigate the role of the linker with variable hydrogen bonding capabilities in mediating the dual MAO-ChE inhibition activity. Moreover, the newly designed benzodioxole-based compounds possess the standard four-point pharmacophoric features, namely, two hydrophobic rings, one or two H-bond donors, and one H-bond acceptor essential for MAO and AChE inhibition activity [35, 36].

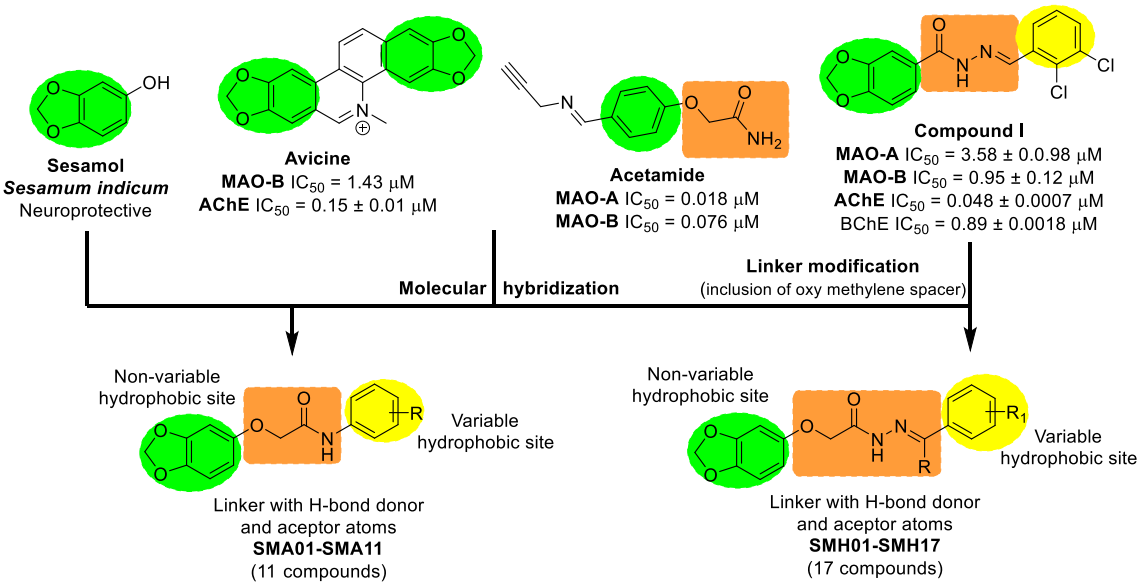

Figure 3.1. Design rationale for compounds **SMA01-SMA11** & **SMH01-SMH17**

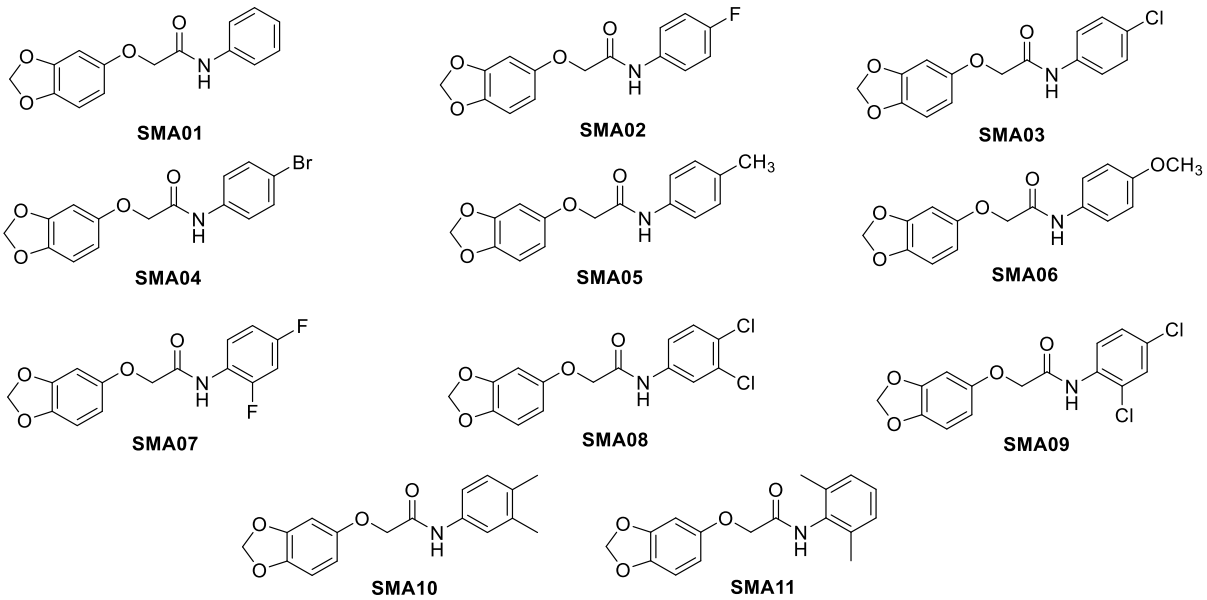

Figure 3.2. 2D chemical structure of designed compounds **SMA01-SMA11**

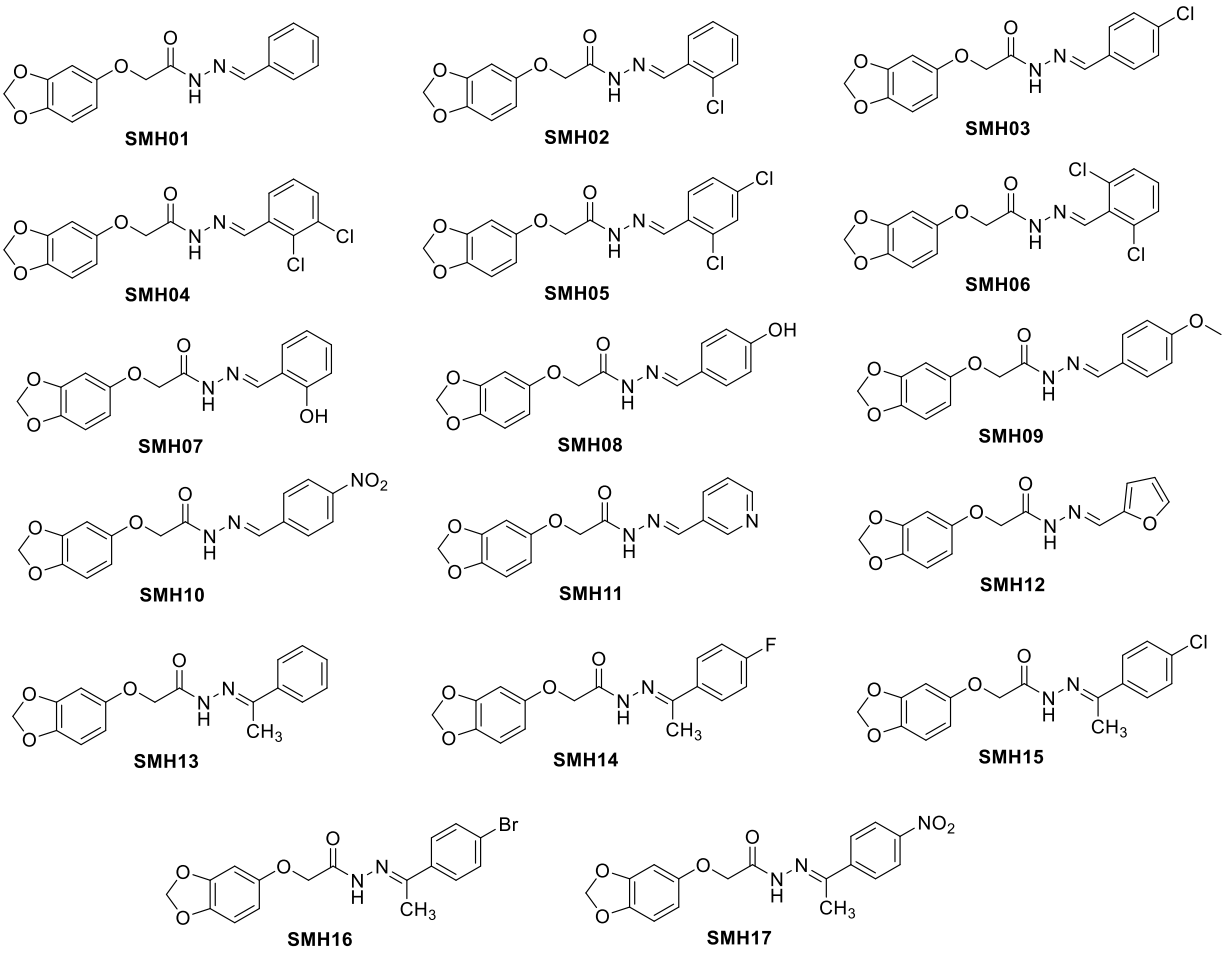

Figure 3.3. 2D chemical structure of designed compounds **SMH01-SMH17**

3.1.2. Objectives

- To design, synthesize and characterize a library of sesamol-derived O-acetamides
- To perform *in vitro* biological evaluation of synthesized compounds against MAOs (MAO-A/B) and ChEs (AChE and BChE) along with antioxidant and metal chelation assay of selected compounds
- To carry out enzyme kinetics and reversibility studies on lead molecule(s) against MAO-B and AChE
- To perform *in vitro* PAMPA-BBB assay for brain accessibility potential of the lead molecule
- To evaluate lead compound(s) for their *in vitro* cellular toxicity in fibroblast (L929), neurotoxicity and neuroprotective potential in neuroblastoma (SH-SY5Y) cell line
- To perform post-screening computational studies (MD simulation) and *in vivo* neuroprotective potential of lead molecule.

3.1.3. Plan of work

The plan for the design, synthesis and evaluation of the current series (**SMA** and **SMH series**) of compounds (**SMA01-SMA11** & **SMH01-SMH17**) is schematically given in **Figure 3.4.** The molecular hybridization and linker modification strategies were used for the design of the **SMA** and **SMH series** of compounds. A library of 11 sesamol-derived O-acetamides and 17 sesamol-derived extended carbohydrazones was synthesized and evaluated by using *in vitro*, *in cellulo*, *in vivo* and *ex vivo* studies. The workflow is schematically given in **Figure 3.4** and the detailed methodologies are described in the following section.

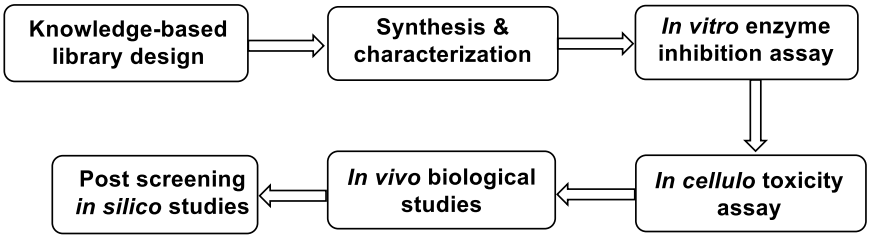

Figure 3.4. Schematic workflow for plan of work

3.2. Experimental Work

3.2.1. Chemistry

3.2.1.1. Synthesis

The chemicals and reagents utilized for synthesis purposes were procured from authentic sources. The synthetic reagents were obtained from Sigma-Aldrich Chemical Private Limited India, TCI India, Merck India, Fischer Scientific Limited., Sisco Research Laboratories (SRL) Private Limited, and Spectrochem Private Limited; and were used as such without any purification.

A. Synthesis sesamol-derived acetamides

Step 1: Synthesis of phenyl chloroacetamide (1-11) fragments

The powdered and activated potassium carbonate (10.0 mmol) and chloroacetyl chloride (10.0 mmol) were added to a magnetically stirred solution of substituted aniline (5.0 mmol) in dimethyl formamide (DMF, 10 mL) at 0˚C. The resultant reaction mixture was further stirred for about 1 h and the progress of the reaction was monitored by TLC. On completion of the reaction (as confirmed by TLC), the reaction mixture was poured on ice and an equal volume of water (50 mL) was added to quench excess chloroacetyl chloride and DMF present in the reaction mixture. The content was stirred for about 10 min and then filtered under reduced pressure to yield a solid product and it was used in the next step without further purification and characterization.

Step 2: Synthesis of final compounds (SMA01-SMA11)

An equimolar solution of sesamol (2 mmol) and appropriate fragment **1-11** (2 mmol) was added to a flat bottom flask containing 20 mL of acetonitrile and potassium carbonate (4 mmol). The reaction mixture was refluxed for 12-16 h and the reaction progress was monitored with TLC. After completion of the reaction, the solvent was evaporated under reduced pressure and the resultant solid was partitioned with 20 mL dichloromethane three times. The organic layer was collected and dried over anhydrous sodium sulfate. Finally, the dried organic layer was evaporated under reduced pressure to yield the solid product. The obtained solid was purified by column chromatography using 20 % ethyl acetate and *n*-hexane (**Scheme 3.1A**).

B. Synthesis of sesamol-derived extended carbohydrazones

Step 1: Synthesis of ethyl 2-(benzo[*d*][1,3]dioxol-5-yloxy)acetate (SME IM 01)

To a magnetically stirred solution of sesamol (40 mmol) in acetone (50 mL), activated powdered potassium carbonate (80 mmol) and ethyl bromoacetate (80 mmol) was added. The resultant reaction mixture was stirred at room temperature for 48 h. The progress of the reaction was monitored by TLC (20 % ethyl acetate: *n*-hexane). After completion of the reaction, the acetone was evaporated and residue was partitioned with ethyl acetate and water. The solid product was purified by removing excess ethyl bromoacetate through column chromatography (ethyl acetate: *n*-hexane, 1:9). The synthetic scheme for intermediates **SME IM 01** is given in **Scheme 3.1B**.

Step 2: Synthesis of 2-(benzo[*d*][1,3]dioxol-5-yloxy)acetohydrazide (SME IM 02)

To a magnetically stirred solution of **SME IM 01** (40 mmol) in ethanol (50 mL) hydrazine hydrate (120 mmol) was added and the resultant solution was refluxed for 8 h. The progress of the reaction was recorded using TLC (60 % ethyl acetate: *n*-hexane). Workup was done

by cooling the reaction to 0 ºC and the precipitated solid product was filtered under reduced pressure using a Buchner funnel.

Step 3: Synthesis of final compounds SMH01-SMH17

To a magnetically stirred solution of 2-(benzo[*d*][1,3]dioxol-5-yloxy)acetohydrazide (**SME IM 02**, 1 mmol) in ethanol (10 mL) suitable substituted aldehyde/ketone (1.1 mmol) was added and the pH of the reaction mixture was adjusted to 5-6 using glacial acetic acid and stirred at RT (for aldehydes) or reflux (for ketones) for about 5-24 h. The progress of the reaction was monitored by TLC (60 % ethyl acetate: *n*-hexane) and after completion, the reaction mixture was cooled to 0 ºC and the solid precipitated product was filtered under reduced pressure.

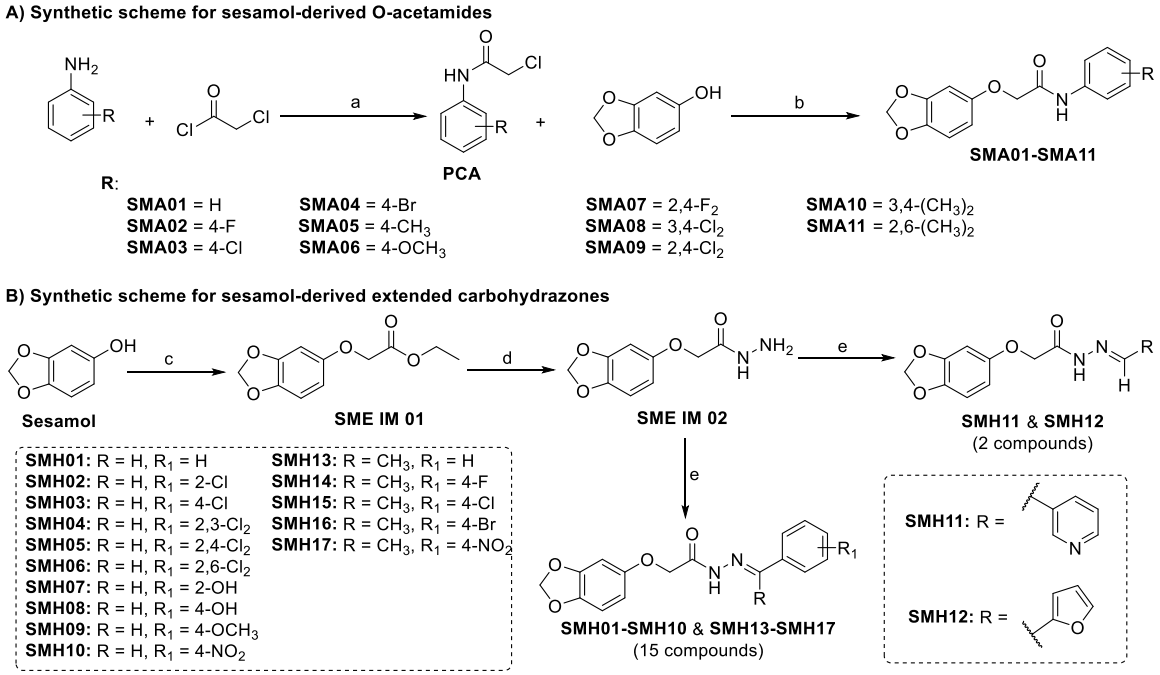

Scheme 3.1. Synthetic scheme for sesamol-derived O-acetamides and extended carbohydrazones (**SMA01-SMA11** & **SMH01-SMH17**) [182]; Reagents and reaction conditions: a) K_2CO_3, DMF, 0-5 ˚C, 1 h; b) K_2CO_3, ACN, reflux, 12-16 h*;* c) Ethyl bromoacetate, acetone, K_2CO_3, 0 ˚C to RT, 48 h; d) hydrazine hydrate, EtOH, reflux, 8 h; and e) substituted aldehydes/ketones, EtOH, RT-reflux, 5-24 h.

3.2.1.2. Physicochemical characterization

The physicochemical characterization of synthesized compounds SMA was carried out for appearance, solubility, retardation factor (R_f), melting point (MP), calculated logP and experimental logP of final compounds (**SMA01-SMA11** & **SMH01-SMH17**) using methods discussed earlier (**Section 2.3.2**).

3.2.1.3. Spectral characterization

The chemical structures of intermediates and final compounds of **SMA** and **SMH series** (**SMA01-SMA11** & **SMH01-SMH17**) were elucidated and confirmed using different advanced spectroscopic techniques including FTIR, ^{1}H, ^{13}C NMR and HRMS as discussed in the previous section (**Section 2.3.3**).

3.2.2. Biological studies

3.2.2.1. *In vitro* studies

3.2.2.1.1. *In vitro* MAO inhibition assay

The *in vitro* enzyme inhibition study was carried out to evaluate the inhibitory potential of compounds (**SMA01-SMA11** & **SMH01-SMH17**) against ratMAO-A and ratMAO-B. The peroxidase-linked colorimetric method described by Holt *et al* was used for the MAO screening study. The assay is based on the colorimetric detection of 'quinoneimine dye' at 490 nm, formed by the reaction of vanillic acid and the oxidized product of 4-aminoantipyrine, the chromogenic substrate for this assay. The oxidation of 4-aminoantipyrine, in turn, is brought about by the action of MAO-A/B on its amine substrate i.e., serotonin and benzylamine, respectively, via the formation of the ROS (H_2O_2) through the cascade reaction. A complete protocol for MAO-A/B assay using the peroxidase-linked spectrometric method is mentioned in the earlier section (**Section 2.4.1.1**).

3.2.2.1.2. *In vitro* ChEs inhibition assay

Test compounds (**SMA01-SMA11** & **SMH01-SMH17**) were studied against cholinesterases (*ee*AChE and *eq*BChE) using a well-known spectrometric method described by Ellman *et al.* The method is based on the hydrolysis of acetylthiocholine iodide (ATCI) and butyrylthiocholine iodide (BTCI) and the formation of nitro thiobenzoate (yellow) from 5,5-Dithiobis(2-Nitro Benzoic Acid) (DTNB) and thiocholine. The color intensity of the yellow complex of DTNB and thiocholine was measured at λ 415 nm. A complete protocol for AChE and BChE enzyme inhibition is discussed in the previous section (**Section 2.4.1.3**).

3.2.2.1.3. Enzyme kinetics and reversibility

Enzyme kinetics and time-dependent reversibility study of compounds **SMA09** and **SMH06** were performed using different substrate (2.5, 5.0, 7.5, 10.0, and 15 mM) and inhibitor concentrations (1, 5 and 10 μM) by employing peroxidase-linked colorimetric method while time-dependent reversibility study was also performed to access the type of inhibition. To determine the AChE inhibitory mechanism of the lead compounds **SMA09** and **SMH06**, reciprocal plots of 1/[V] versus 1/[S] were constructed using five different concentrations of the substrate acetylthiocholine iodide (ATCI) (0.5, 1.0, 1.5, 2.0, and 2.5 mM) using Ellman's method whereas the time-dependent reversibility study was performed using variable incubation time up to 60 min. A detailed protocol and detailed method for enzyme kinetics and reversibility study are given earlier (**Section 2.4.1.4**).

3.2.2.1.4. *In vitro* antioxidant assay

Antioxidant or free radical scavenging activity of selected test compounds along with donepezil, selegiline and tranylcypromine was performed by using 1,1-diphenyl-2-picrylhydrazyl (DPPH) assay. The method is based on the reductive capacity of a test molecule that can reduce 1,1-diphenyl-2-picrylhydrazyl (DPPH, deep purple color) to 1,1-

diphenyl-2-picrylhydrazine (DPPH-H, pale yellow color) which shows absorbance at 517 nm. A complete detailed procedure for the antioxidant assay is discussed earlier (**Section 2.4.1.5**).

3.2.2.1.5. *In vitro* metal chelation assay

Iron chelation study of selected test compounds was carried out using the UV-based spectrophotometric method. An assay was performed in methanol while ferric chloride hexahydrate was used as the source of iron ions. The detailed procedure for the metal chelation study is described earlier (**Section 2.4.1.6**).

3.2.2.1.6. *In vitro* blood-brain-barrier permeation assay

The *in vitro* blood-brain-barrier permeability assay of compounds **SMA09** and **SMH06** was performed using the PAMPA-BBB assay to evaluate the brain accessibility potential of the compound. The assay was carried out in a 96-well plate equipped with a microfilter device at its bottom and coated with a hydrophobic material (porcine brain lipid) that mimics BBB. A detailed step-by-step protocol for PAMPA-BBB assay is discussed earlier (**Section 2.4.1.7**).

3.2.2.1.7. Cell-based neurotoxicity assay

Compounds **SMA09** and **SMH06** were evaluated for their cytotoxicity in fibroblast (L929) cells and neurotoxicity in the neuroblastoma cell line (SH-SY5Y). The cells were treated with the different concentrations (0.1, 1, 10, 50 and 100 μM) of the test compound for 24 h. Further, an MTT assay was performed to estimate the percent cell viability. A detailed method for cell culture and MTT assay is described earlier (**Section 2.4.1.8**)

3.2.2.1.8. Neuroprotection assay using neuroblastoma cell line

The neuroprotective potential of compound **SMA09** was evaluated against dexamethasone-induced oxidative stress and apoptosis. The cells were treated for 3 days (72 h) with

different concentrations (0.25, 100 and 200 nM) of compound **SMA09** prepared in media containing 2 μM of dexamethasone (HiMedia Laboratories Private Limited, India, Cat. TCL211) solution. Furthermore, an MTT assay was performed to assess the cell survival and neuroprotective potential of the compound. A more detailed method is described earlier (**Section 2.4.1.9**).

3.2.2.2. *In vivo* studies

3.2.2.2.1. Scopolamine induced amnesia model

The *in vivo* neuroprotective efficacy of the compounds **SMA09** & **SMH06** was evaluated using a scopolamine-induced amnesia model and Y-maze test. A 7-day prophylactic treatment of 5 mg/kg (i.p.) of test compounds **SMA09** and **SMH06** and 5 mg/kg (i.p.) of donepezil was given to the mice and on the 7^{th} day animals were treated with 3 mg/kg (i.p.) of scopolamine 30 min post-treatment with test compound or vehicle. After 15 min of scopolamine administration, the animals were subjected to a Y-maze test. The spontaneous alteration behavior of each animal was recorded and the obtained results were analyzed. A detailed method for scopolamine-induced amnesia and the Y-maze test is described earlier (**Section 2.4.2.1**).

3.2.2.2.2. Y-maze test

The spontaneous alternation (SA) score was recorded using a three-arm maze, where each arm was separated by an angle of 120°. The three arms were labeled A, B, and C. During the test, each mouse was placed at the center of the maze and allowed to explore freely for a duration of 8 min. The entry into each arm was recorded using a video camera. Data from each mouse was analyzed to calculate the percentage of spontaneous alteration. A detailed method for the Y-maze test is discussed earlier section (**Section 2.4.2.2**).

3.2.2.2.3. *Ex vivo* biochemical analysis

The brain samples (hippocampus and cortex region) were collected and biochemical analysis was performed after homogenization and centrifugation. Supernatant from centrifuged brain tissue was collected and the level of ACh, AChE, MDA and CAT was determined by using methods described earlier (**Section 2.4.2.3**).

3.2.2.2.4. *In vivo* acute oral toxicity evaluation of compound SMA09

The *in vivo* acute oral toxicity was performed in adult female albino mice as per OECD guidelines 423 (Acute Toxicity Class Method). The median lethal dose (LD_{50}) was determined with a single dose of 300 mg/kg and 2000 mg/kg BW. Animals were divided into groups and a single dose of test compound was given to each group whereas the control group received vehicle (0.5 % sodium carboxymethyl cellulose). A detailed step-by-step protocol is discussed in the earlier section (**Section 2.4.2.4**).

3.3. Computational studies

3.3.1. Molecular docking

Molecular docking studies of all the test compounds **SMA01-SMA11** & **SMH01-SMH17** and co-crystallized inhibitors were carried out using AutoDock Tools 4.2 (ADT) software (The Scripps Research Institute, California, USA). A descriptive method for molecular docking using AutoDock Tools 4.2 software is mentioned earlier (**Section 2.5.1**).

3.3.2. Molecular dynamics simulation

Molecular dynamic simulation of the selected compound was performed using Desmond software (Schrodinger Release 2021.1). Preparation of input files from the protein-ligand complex and analysis of simulated results and trajectory analysis were completed in the Maestro graphical user interface (Maestro, Schrodinger, LLC, New York, NY, 2021).

Detailed protocol for molecular dynamic simulation using Desmond software is discussed earlier (**Section 2.5.2**).

3.3.3. Ligand binding efficiency

Ligand binding efficiency for all the synthesized compounds **SMA01-SMA11** & **SMH01-SMH17** along with reference inhibitors (clorgyline, selegiline and donepezil) was calculated from a web-based server (MedChem calculators) by feeding IC_{50} value and number of heavy atoms (http://www.vulpinescience.co.uk/uploads/MedChem%20Calculators_Ver3.2/MedChem%20Calculators.htm) accessed on 07 October 2024.

3.3.4. Predicted ADMET properties

Compounds **SMA01-SMA11** & **SMH01-SMH17** were screened for *in silico* ADMET (absorption, distribution, metabolism, excretion and toxicity) property prediction. The 'PreADMET' server (web-based) was used for the calculation of ADMET parameters. The server employs various algorithms for ADME and toxicity prediction (https://preadmet.bmdrc.kr/). The .mol coordinates of each compound were generated from sketched 2D chemical structures and fed into the PreADMET server for properties calculation.

3.4. Results and Discussion

3.4.1. Chemistry

A. SMA Series

3.4.1.1. Physicochemical characterization of final compounds (SMA series)

All the final compounds were characterized for different physicochemical parameters including experimental yield, appearance, solubility, retardation factor analysis, melting point and experimental logP. Compounds **SMA01-SMA11** were soluble in DCM, chloroform and ethyl acetate. The results of physicochemical characterization are given in **Table 3.1**.

Table 3.1. Physicochemical characterization results of compounds **SMA01-SMA11**

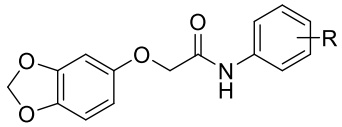

SMA01-SMA11

Compd. Code	R	MW	ClogP[a]	logP[b]	% Yield	R_f[c]	MP (°C)	Appearance
SMA01	H	271.27	2.71	1.93	84	0.72	100-102	White solid
SMA02	4-F	289.26	3.11	1.48	60	0.75	123-125	Off-white solid
SMA03	4-Cl	305.71	3.68	2.03	75	0.84	115-117	White solid
SMA04	4-Br	350.16	3.83	2.23	86	0.51	128-130	White solid
SMA05	4-CH_3	285.29	3.21	2.39	80	0.85	112-114	Off white solid
SMA06	4-OCH_3	301.29	2.79	2.13	83	0.77	93-95	Off white solid
SMA07	2,4-F_2	307.25	2.74	1.96	68	0.90	140-142	Pale yellow solid
SMA08	3,4-Cl_2	340.15	4.36	1.99	76	0.64	130-132	White solid
SMA09	2,4-Cl_2	340.15	3.63	1.28	61	0.51	148-149	Colorless crystals
SMA10	3,4-$(CH_3)_2$	299.32	3.66	1.66	73	0.75	97-99	Off white solid
SMA11	2,6-$(CH_3)_2$	299.32	2.41	1.93	70	0.54	111-113	Off white solid

[a] Computationally calculated logP using ChemDraw Professional 17.1.0; [b] Experimental logP determined using *n*-octanol/water; [c] TLC mobile phase (40 % ethyl acetate: *n*-hexane).

3.4.1.2. Spectral characterization of final compounds (SMA series)

The characteristic stretching vibrations at *v* 1196-1174 cm^{-1} in the FTIR spectra confirmed the formation of C-O bond in the final compounds (compounds **SMA01-SMA11**). Further,

the carbonyl stretching and amide NH stretching vibrations were seen at *v* 3410-3253 cm^{-1} and *v* 1778-1664 cm^{-1}, respectively. In proton NMR, methylene and NH protons were observed at δ 4.54-4.66 ppm and δ 7.82-8.97 ppm, respectively. The ^{13}C NMR spectra further confirmed the presence of methylene carbon and carbonyl carbon in the final compounds at δ 68.55-68.78 ppm and δ 166.05-166.69 ppm, respectively. The HRMS spectra accurately estimated the mass of final compounds, and the obtained spectra of all compounds are included in the supplementary document. The accuracy of the obtained HRMS spectra was found to be between 0.0001-0.0032 ppm from the calculated $(M+H)^+$ mass of the compounds.

2-(benzo[*d*][1,3]dioxol-5-yloxy)-*N*-phenylacetamide (SMA01): White solid; Yield: 84 %; MP: 100-102 ˚C; R_f: 0.72 in 40 % ethyl acetate-*n*-hexane; λ_{max} = 295 nm; FTIR (KBr, *v,* cm^{-1}): 3408 (N-H str), 2895 (cyclic CH_2 str), 2782 (aliphatic CH_2 str), 1692 (C=O str), 1193 (C-O str); ^1H NMR (500 MHz, $CDCl_3$) δ 8.25 (s, 1H, amide -NH), 7.61 (d, *J* = 8.7 Hz, 2H, Ar-C2, C6), 7.38 (t, *J* = 7.9 Hz, 2H, Ar-C3, C5), 7.23 – 7.15 (m, 1H, Ar-C4), 6.77 (d, *J* = 8.5 Hz, 1H, benzo[*d*][1,3]dioxol C6), 6.61 (s, 1H, benzo[*d*][1,3]dioxol C4), 6.43 (d, *J* = 8.5 Hz, 1H, benzo[*d*][1,3]dioxol C7), 5.98 (s, 2H, benzo[*d*][1,3]dioxol C2), 4.56 (s, 2H, aliphatic CH_2); ^{13}C NMR (126 MHz, $CDCl_3$) δ 166.26 (-C=O), 152.46 (benzo[*d*][1,3]dioxol C5), 148.65 (benzo[*d*][1,3]dioxol C3a), 143.05 (benzo[*d*][1,3]dioxol C7a), 136.83 (Ar-C1), 129.12 (Ar-C3, C5), 124.90 (Ar-C4), 120.10 (Ar-C2, C6), 108.20 (benzo[*d*][1,3]dioxol C7), 106.32 (benzo[*d*][1,3]dioxol C6), 101.54 (benzo[*d*][1,3]dioxol C2), 98.48 (benzo[*d*][1,3]dioxol C4), 68.77 (aliphatic CH_2); HRMS Calcd for $C_{15}H_{13}NO_4$ $(M+H)^+$ 272.0923, found 272.0922.

2-(benzo[*d*][1,3]dioxol-5-yloxy)-*N*-(4-fluorophenyl)acetamide (SMA02): Off-white solid; Yield: 60 %; MP: 123-125 ˚C; R_f: 0.75 in 40 % ethyl acetate-*n*-hexane; λ_{max} = 290 nm; FTIR (KBr, *v,* cm^{-1}): 3394 (N-H str), 3046 (aromatic C-H str), 2914 (cyclic CH_2 str),

2851 (aliphatic CH_2 str), 1693 (C=O str), 1181 (C-O str), 1033 (aromatic C-F str); ^{1}H NMR (500 MHz, $CDCl_3$) δ 8.23 (s, 1H, amide -NH), 7.57 (dd, J = 9.2, 4.7 Hz, 2H, Ar-C2, C6), 7.13 – 7.04 (m, 2H, Ar-C3, C5), 6.77 (d, J = 8.5 Hz, 1H, benzo[*d*][1,3]dioxol C6), 6.60 (d, J = 2.6 Hz, 1H, benzo[*d*][1,3]dioxol C4), 6.42 (dd, J = 8.4, 2.6 Hz, 1H, benzo[*d*][1,3]dioxol C7), 5.98 (s, 2H, benzo[*d*][1,3]dioxol C2), 4.56 (s, 2H, aliphatic CH_2); ^{13}C NMR (126 MHz, $CDCl_3$) δ 166.22 (-C=O), 160.70 (Ar-C4), 158.76 (Ar-C4), 152.39 (benzo[*d*][1,3]dioxol C5), 148.66 (benzo[*d*][1,3]dioxol C3a), 143.09 (benzo[*d*][1,3]dioxol C7a), 132.85 (Ar-C1), 121.97 (Ar-C4), 115.88 (Ar-C2, C6), 115.70 (Ar-C3, C5), 108.21 (benzo[*d*][1,3]dioxol C7), 106.29 (benzo[*d*][1,3]dioxol C6), 101.56 (benzo[*d*][1,3]dioxol C2), 98.45 (benzo[*d*][1,3]dioxol C4), 68.70 (aliphatic CH_2); HRMS Calcd for $C_{15}H_{12}FNO_4$ $(M+H)^+$ 290.0828, found 290.0831.

2-(benzo[*d*][1,3]dioxol-5-yloxy)-*N*-(4-chlorophenyl)acetamide (SMA03): White solid; Yield: 75 %; MP: 115-117 ˚C; R_f: 0.84 in 40 % ethyl acetate-*n*-hexane; λ_{max} = 290 nm; FTIR (KBr, *v,* cm^{-1}): 3390 (N-H str), 3099 (aromatic C-H str), 2921 (cyclic CH_2 str), 2852 (aliphatic CH_2 str), 1778 (C=O str), 1200 (aromatic C-Cl), 1183 (C-O str); ^{1}H NMR (500 MHz, $CDCl_3$) δ 8.26 (s, 1H, amide -NH), 7.57 (d, J = 8.9 Hz, 2H, Ar-C2, C6), 7.34 (d, J = 8.9 Hz, 2H, Ar-C3, C5), 6.77 (d, J = 8.5 Hz, 1H, benzo[*d*][1,3]dioxol C6), 6.60 (d, J = 2.6 Hz, 1H, benzo[*d*][1,3]dioxol C4), 6.42 (dd, J = 8.4, 2.6 Hz, 1H, benzo[*d*][1,3]dioxol C7), 5.98 (s, 2H, benzo[*d*][1,3]dioxol C2), 4.55 (s, 2H, aliphatic CH_2); ^{13}C NMR (126 MHz, $CDCl_3$) δ 166.27 (-C=O), 152.33 (benzo[*d*][1,3]dioxol C5), 148.67 (benzo[*d*][1,3]dioxol C3a), 143.13 (benzo[*d*][1,3]dioxol C7a), 135.43 (Ar-C1), 129.93 (Ar-C4), 129.15 (Ar-C3, C5), 121.29 (Ar-C2, C6), 108.21 (benzo[*d*][1,3]dioxol C7), 106.31 (benzo[*d*][1,3]dioxol C6), 101.57 (benzo[*d*][1,3]dioxol C2), 98.46 (benzo[*d*][1,3]dioxol C4), 68.72 (aliphatic CH_2); HRMS Calcd for $C_{15}H_{12}ClNO_4$ $(M+H)^+$ 306.0533, found 306.0540.

2-(benzo[*d*][1,3]dioxol-5-yloxy)-*N*-(4-bromophenyl)acetamide (SMA04): White solid; Yield: 86 %; MP: 128-130 ˚C; R_f: 0.51 in 40 % ethyl acetate-*n*-hexane; λ_{max} = 290 nm; FTIR (KBr, *v,* cm^{-1}): 3364 (N-H str), 3068 (aromatic C-H str), 2891 (cyclic CH_2 str), 2774 (aliphatic CH_2 str), 1672 (C=O str), 1181 (C-O str), 1034 (aromatic C-Br); ^{1}H NMR (500 MHz, $CDCl_3$) δ 8.25 (s, 1H, amide -NH), 7.57 – 7.46 (m, 4H, Ar-C2, C3, C5, C6), 6.77 (d, *J* = 8.5 Hz, 1H, benzo[*d*][1,3]dioxol C6), 6.60 (d, *J* = 2.6 Hz, 1H, benzo[*d*][1,3]dioxol C4), 6.42 (dd, *J* = 8.5, 2.6 Hz, 1H, benzo[*d*][1,3]dioxol C7), 5.98 (s, 2H, benzo[*d*][1,3]dioxol C2), 4.55 (s, 2H, aliphatic CH_2); ^{13}C NMR (126 MHz, $CDCl_3$) δ 166.28 (-C=O), 152.32 (benzo[*d*][1,3]dioxol C5), 148.68 (benzo[*d*][1,3]dioxol C3a), 143.14 (benzo[*d*][1,3]dioxol C7a), 135.93 (Ar-C1), 132.11 (Ar-C3, C5), 121.60 (Ar-C2, C6), 117.54 (Ar-C4), 108.21 (benzo[*d*][1,3]dioxol C7), 106.32 (benzo[*d*][1,3]dioxol C6), 101.57 (benzo[*d*][1,3]dioxol C2), 98.47 (benzo[*d*][1,3]dioxol C4), 68.73 (aliphatic CH_2); HRMS Calcd for $C_{15}H_{12}BrNO_4$ $(M+H)^+$ 350.0028, found 350.0045; HPLC purity: 95.99 %.

2-(benzo[*d*][1,3]dioxol-5-yloxy)-*N*-(*p*-tolyl)acetamide (SMA05): Off-white solid; Yield: 80 %; MP: 112-114 ˚C; R_f: 0.85 in 40 % ethyl acetate-*n*-hexane; λ_{max} = 290 nm; FTIR (KBr, *v,* cm^{-1}): 3396 (N-H str), 2918 (cyclic CH_2 str), 2851 (aliphatic CH_2 str), 1675 (C=O str), 1187 (C-O str); ^{1}H NMR (500 MHz, $CDCl_3$) δ 8.19 (s, 1H, amide -NH), 7.48 (d, *J* = 8.4 Hz, 2H, Ar-C2, C6), 7.18 (d, *J* = 8.5 Hz, 2H, Ar-C3, C5), 6.76 (d, *J* = 8.5 Hz, 1H, benzo[*d*][1,3]dioxol C6), 6.60 (d, *J* = 2.6 Hz, 1H, benzo[*d*][1,3]dioxol C4), 6.43 (dd, *J* = 8.4, 2.6 Hz, 1H, benzo[*d*][1,3]dioxol C7), 5.98 (s, 2H, benzo[*d*][1,3]dioxol C2), 4.55 (s, 2H, aliphatic CH_2), 2.35 (s, 3H, Ar-CH_3); ^{13}C NMR (126 MHz, $CDCl_3$) δ 166.10 (-C=O), 152.50 (benzo[*d*][1,3]dioxol C5), 148.63 (benzo[*d*][1,3]dioxol C3a), 143.00 (benzo[*d*][1,3]dioxol C7a), 134.57 (Ar-C1), 134.28 (Ar-C4), 129.60 (Ar-C3, C5), 120.15 (Ar-C2, C6), 108.19 (benzo[*d*][1,3]dioxol C7), 106.30 (benzo[*d*][1,3]dioxol C6), 101.52

(benzo[*d*][1,3]dioxol C2), 98.46 (benzo[*d*][1,3]dioxol C4), 68.76 (aliphatic CH_2), 20.89 (Ar-CH_3); HRMS Calcd for $C_{16}H_{15}NO_4$ $(M+H)^+$ 286.1079, found 286.1080.

2-(benzo[*d*][1,3]dioxol-5-yloxy)-*N*-(4-methoxyphenyl)acetamide (SMA06): Off-white solid; Yield: 83 %; MP: 93-95 ˚C; R_f: 0.77 in 40 % ethyl acetate-*n*-hexane; λ_{max} = 285 nm; FTIR (KBr, *v,* cm^{-1}): 3329 (N-H str), 2904 (cyclic CH_2 str), 1664 (C=O str), 1174 (C-O str); ^1H NMR (500 MHz, $CDCl_3$) δ 8.15 (s, 1H, amide -NH), 7.50 (d, *J* = 9.0 Hz, 2H, Ar-C2, C6), 6.91 (d, *J* = 9.0 Hz, 2H, Ar-C3, C5), 6.77 (d, *J* = 8.5 Hz, 1H, benzo[*d*][1,3]dioxol C6), 6.60 (d, *J* = 2.6 Hz, 1H, benzo[*d*][1,3]dioxol C4), 6.42 (dd, *J* = 8.4, 2.6 Hz, 1H, benzo[*d*][1,3]dioxol C7), 5.98 (s, 2H, benzo[*d*][1,3]dioxol C2), 4.55 (s, 2H, aliphatic CH_2), 3.83 (s, 3H, -OCH_3); ^{13}C NMR (126 MHz, $CDCl_3$) δ 166.05 (-C=O), 156.87 (Ar-C4), 152.51 (benzo[*d*][1,3]dioxol C5), 148.63 (benzo[*d*][1,3]dioxol C3a), 142.99 (benzo[*d*][1,3]dioxol C7a), 129.91 (Ar-C1), 121.95 (Ar-C2, C6), 114.28 (Ar-C3, C5), 108.19 (benzo[*d*][1,3]dioxol C7), 106.28 (benzo[*d*][1,3]dioxol C6), 101.52 (benzo[*d*][1,3]dioxol C2), 98.45 (benzo[*d*][1,3]dioxol C4), 68.73 (aliphatic -CH_2), 55.50 (-OCH_3); HRMS Calcd for $C_{16}H_{15}NO_5$ $(M+H)^+$ 302.1028, found 302.1030.

2-(benzo[*d*][1,3]dioxol-5-yloxy)-*N*-(2,4-difluorophenyl)acetamide (SMA07): Pale yellow solid; Yield: 68 %; MP: 140-142 ˚C; R_f: 0.90 in 40 % ethyl acetate-*n*-hexane; λ_{max} = 285 nm; FTIR (KBr, *v,* cm^{-1}): 3405 (N-H str), 3112 (aromatic C-H str), 2909 (cyclic CH_2 str), 2792 (aliphatic CH_2 str), 1694 (C=O str), 1189 (C-O str); ^1H NMR (500 MHz, $CDCl_3$) δ 8.47 (s, 1H, amide -NH), 8.33 (td, *J* = 9.1, 5.9 Hz, 1H, Ar-C6), 6.98 – 6.89 (m, 2H, Ar-C3, C5), 6.77 (d, *J* = 8.5 Hz, 1H, benzo[*d*][1,3]dioxol C6), 6.60 (d, *J* = 2.6 Hz, 1H, benzo[*d*][1,3]dioxol C4), 6.46 – 6.40 (m, 1H, benzo[*d*][1,3]dioxol C7), 5.98 (s, 2H, benzo[*d*][1,3]dioxol C2), 4.59 (s, 2H, aliphatic -CH_2); ^{13}C NMR (126 MHz, $CDCl_3$) δ 166.34 (-C=O), 152.33 (Ar-C4), 148.66 (Ar-C4), 143.13 (Ar-C2), 122.79 (benzo[*d*][1,3]dioxol C3a), 111.43 (benzo[*d*][1,3]dioxol C7a), 108.18 (benzo[*d*][1,3]dioxol

C7), 106.30 (benzo[*d*][1,3]dioxol C6), 103.77 (Ar-C5), 103.56 (Ar-C3), 101.55 (benzo[*d*][1,3]dioxol C2), 98.49 (benzo[*d*][1,3]dioxol C4), 68.69 (aliphatic CH_2); HRMS Calcd for $C_{15}H_{11}F_2NO_4$ $(M+H)^+$ 308.0734, found 308.0745.

2-(benzo[*d*][1,3]dioxol-5-yloxy)-*N*-(3,4-dichlorophenyl)acetamide (SMA08): White solid; Yield: 76 %; MP: 130-132 ˚C; R_f: 0.64 in 40 % ethyl acetate-*n*-hexane; λ_{max} = 290 nm; FTIR (KBr, *v,* cm^{-1}): 3390 (N-H str), 2915 (cyclic CH_2 str), 1698 (C=O str), 1185 (C-O str), 1034 (aromatic C-Cl str); ^{1}H NMR (600 MHz, $CDCl_3$) δ 8.27 (s, 1H, amide -NH), 7.85 (d, *J* = 2.5 Hz, 1H, Ar-C2), 7.49 – 7.40 (m, 2H, Ar-C5, C6), 6.77 (dd, *J* = 8.7, 2.1 Hz, 1H, benzo[*d*][1,3]dioxol C6), 6.59 (d, *J* = 2.6 Hz, 1H, benzo[*d*][1,3]dioxol C4), 6.41 (dd, *J* = 6.8, 4.2 Hz, 1H, benzo[*d*][1,3]dioxol C7), 5.99 (s, 2H, benzo[*d*][1,3]dioxol C2), 4.55 (d, *J* = 2.1 Hz, 2H, (aliphatic -CH_2); ^{13}C NMR (151 MHz, $CDCl_3$) δ 166.38 (-C=O), 152.18 (benzo[*d*][1,3]dioxol C5), 148.69 (benzo[*d*][1,3]dioxol C3a), 143.19 (benzo[*d*][1,3]dioxol C7a), 136.28 (Ar-C1), 132.97 (Ar-C5), 130.65 (Ar-C3), 128.16 (Ar-C4), 121.70 (Ar-C6), 119.22 (Ar-C2), 108.23 (benzo[*d*][1,3]dioxol C7), 106.26 (benzo[*d*][1,3]dioxol C6), 101.61 (benzo[*d*][1,3]dioxol C2), 98.45 (benzo[*d*][1,3]dioxol C4), 68.63 (aliphatic CH_2); HRMS Calcd for $C_{15}H_{11}Cl_2NO_4$ $(M+H)^+$ 340.0143, found 340.0158.

2-(benzo[*d*][1,3]dioxol-5-yloxy)-*N*-(2,4-dichlorophenyl)acetamide (SMA09): White crystals; Yield: 61 %; MP: 148-149 ˚C; R_f: 0.51 in 40 % ethyl acetate-*n*-hexane; λ_{max} = 290 nm; FTIR (KBr, *v,* cm^{-1}): 3372 (N-H str), 3090 (aromatic C-H str), 2914 (cyclic CH_2 str), 1701 (C=O str), 1190 (C-O str), 1036 (aromatic C-Cl str); ^{1}H NMR (500 MHz, $CDCl_3$) δ 8.97 (s, 1H, amide -NH), 8.46 (d, *J* = 8.9 Hz, 1H, Ar-C2), 7.43 (d, *J* = 2.4 Hz, 1H, Ar-C5), 7.30 (dd, *J* = 8.9, 2.4 Hz, 1H, Ar-C3), 6.77 (d, *J* = 8.4 Hz, 1H, benzo[*d*][1,3]dioxol C6), 6.61 (d, *J* = 2.6 Hz, 1H, benzo[*d*][1,3]dioxol C4), 6.43 (dd, *J* = 8.4, 2.6 Hz, 1H, benzo[*d*][1,3]dioxol C7), 5.98 (s, 2H, benzo[*d*][1,3]dioxol C2), 4.60 (s, 2H, aliphatic -CH_2); ^{13}C NMR (126 MHz, $CDCl_3$) δ 166.35 (-C=O), 152.29 (benzo[*d*][1,3]dioxol C5),

148.66 (benzo[*d*][1,3]dioxol C3a), 143.13 (benzo[*d*][1,3]dioxol C7a), 132.63 (Ar-C1), 129.59 (Ar-C5), 128.89 (Ar-C4), 127.99 (Ar-C3), 123.65 (Ar-C6), 121.97 (Ar-C2), 108.17 (benzo[*d*][1,3]dioxol C7), 106.20 (benzo[*d*][1,3]dioxol C6), 101.56 (benzo[*d*][1,3]dioxol C2), 98.44 (benzo[*d*][1,3]dioxol C4), 68.67 (aliphatic CH_2); HRMS Calcd for $C_{15}H_{11}Cl_2NO_4$ $(M+H)^+$ 340.0143, found 340.0175; HPLC purity: 99.66 %.

2-(benzo[*d*][1,3]dioxol-5-yloxy)-*N*-(3,4-dimethylphenyl)acetamide (SMA10): Off-white solid; Yield: 73 %; MP: 97-99 ˚C; R_f: 0.75 in 40 % ethyl acetate-*n*-hexane; λ_{max} = 285 nm; FTIR (KBr, *v,* cm^{-1}): 3410 (N-H str), 3084 (aromatic C-H str), 2919 (cyclic CH_2 str), 2773 (aliphatic CH_2 str), 1691 (C=O str), 1196 (C-O str); ^{1}H NMR (500 MHz, $CDCl_3$) δ 8.15 (s, 1H, amide -NH), 7.37 (s, 1H, Ar-C6), 7.33 (d, *J* = 8.1 Hz, 1H, Ar-C2), 7.13 (d, *J* = 8.1 Hz, 1H, Ar-C3), 6.76 (d, *J* = 8.5 Hz, 1H, benzo[*d*][1,3]dioxol C6), 6.60 (d, *J* = 2.6 Hz, 1H, benzo[*d*][1,3]dioxol C4), 6.42 (dd, *J* = 8.5, 2.6 Hz, 1H, benzo[*d*][1,3]dioxol C7), 5.98 (s, 2H, benzo[*d*][1,3]dioxol C2), 4.54 (s, 2H, aliphatic -CH_2), 2.27 (d, *J* = 14.0 Hz, 6H, Ar-CH_3); ^{13}C NMR (126 MHz, $CDCl_3$) δ 166.06 (-C=O), 152.53 (benzo[*d*][1,3]dioxol C5), 148.62 (benzo[*d*][1,3]dioxol C3a), 142.98 (benzo[*d*][1,3]dioxol C7a), 137.38 (Ar-C3), 134.53 (Ar-C1), 133.28 (Ar-C4), 130.07 (Ar-C5), 121.43 (Ar-C2), 117.63 (Ar-C6), 108.18 (benzo[*d*][1,3]dioxol C7), 106.28 (benzo[*d*][1,3]dioxol C6), 101.51 (benzo[*d*][1,3]dioxol C2), 98.46 (benzo[*d*][1,3]dioxol C4), 68.78 (aliphatic CH_2), 19.86 (Ar-C3 -CH_3), 19.21 (Ar-C4 -CH_3); HRMS Calcd for $C_{17}H_{17}NO_4$ $(M+H)^+$ 300.1236, found 300.1235.

2-(benzo[*d*][1,3]dioxol-5-yloxy)-*N*-(2,6-dimethylphenyl)acetamide (SMA11): Off-white solid; Yield: 70 %; MP: 111-113 ˚C; R_f: 0.54 in 40 % ethyl acetate-*n*-hexane; λ_{max} = 285 nm; FTIR (KBr, *v,* cm^{-1}): 3253 (N-H str), 3036 (aromatic C-H str), 2922 (cyclic CH_2 str), 1678 (C=O str), 1187 (C-O str); ^{1}H NMR (500 MHz, $CDCl_3$) δ 7.82 (s, 1H, amide -NH), 7.18 – 7.10 (m, 3H, Ar-C3, C4, C5), 6.78 (d, *J* = 8.5 Hz, 1H, benzo[*d*][1,3]dioxol C6), 6.62 (d, *J* = 2.6 Hz, 1H, benzo[*d*][1,3]dioxol C4), 6.45 (dd, *J* = 8.4, 2.6 Hz, 1H,

benzo[*d*][1,3]dioxol C7), 5.99 (s, 2H, benzo[*d*][1,3]dioxol C2), 4.66 (s, 2H, aliphatic -CH_2), 2.24 (s, 6H, Ar-CH_3); ^{13}C NMR (126 MHz, $CDCl_3$) δ 166.69 (-C=O), 152.64 (benzo[*d*][1,3]dioxol C5), 148.68 (benzo[*d*][1,3]dioxol C3a), 142.92 (benzo[*d*][1,3]dioxol C7a), 135.40 (Ar-C1), 132.66 (Ar-C2, C6), 128.33 (Ar-C3, C5), 127.67 (Ar-C4), 108.17 (benzo[*d*][1,3]dioxol C7), 105.93 (benzo[*d*][1,3]dioxol C6), 101.52 (benzo[*d*][1,3]dioxol C2), 98.31 (benzo[*d*][1,3]dioxol C4), 68.55 (aliphatic -CH_2), 18.42 (Ar-C2, C6 -CH_3); HRMS Calcd for $C_{17}H_{17}NO_4$ $(M+H)^+$ 300.1236, found 300.1240.

B. SMH Series

3.4.1.3. Physicochemical characterization of final compounds (SMH series)

The synthesized compounds were characterized for different physicochemical parameters including experimental yield, appearance, solubility, retardation factor analysis and melting point. The compounds **SMH01-SMH12** were soluble in DCM, methanol, chloroform and ethyl acetate while compounds **SMH13-SMH17** were soluble in DMF and DMSO. The results of physicochemical characterization are given in **Table 3.2**.

Table 3.2. Physicochemical characterization results of compounds **SMH01-SMH17**

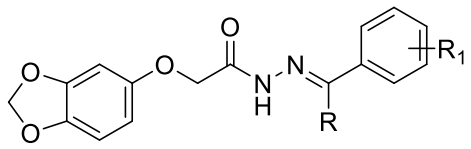

Compd. Code	R	R_1	MW	ClogP[a]	% Yield	R_f[b]	MP (°C)	Appearance
SMH01	H	H	298.10	2.72	90	0.87	152-154	White solid
SMH02	H	2-Cl	332.74	2.83	70	0.83	136-138	White solid
SMH03	H	4-Cl	332.74	3.43	91	0.85	161-163	White solid
SMH04	H	2,3-Cl_2	367.18	3.42	90	0.77	140-142	White solid
SMH05	H	2,4-Cl_2	367.18	3.54	89	0.76	110-112	White solid
SMH06	H	2,6-Cl_2	367.18	2.94	85	0.76	155-157	White solid
SMH07	H	2-OH	314.30	3.32	88	0.57	138-140	Off white solid
SMH08	H	4-OH	314.30	2.69	93	0.56	209-211	White solid
SMH09	H	4-OCH_3	328.32	2.94	91	0.52	128-130	White solid

SMH10	H	4-NO_2	343.30	2.46	92	0.88	170-172	Pale yellow solid
SMH11	H	3-Pyridyl	299.29	1.40	70	0.85	141-143	White solid
SMH12	H	2-furfuryl	288.26	1.89	92	0.89	125-127	Off white solid
SMH13	CH_3	H	312.33	3.98	76	0.71	112-114	Colorless crystals
SMH14	CH_3	4-F	330.32	4.12	72	0.72	132-134	White solid
SMH15	CH_3	4-Cl	346.77	4.69	72	0.70	171-173	White solid
SMH16	CH_3	4-Br	391.22	4.84	87	0.76	142-144	White solid
SMH17	CH_3	4-NO_2	357.32	3.72	87	0.65	172-174	Pale yellow solid

[a] Computationally calculated logP using ChemDraw Professional 17.1.0; [b] TLC mobile phase (60 % ethyl acetate: *n*-hexane).

3.4.1.4. Spectral characterization of final compounds (SMH series)

The synthesized molecules (compounds **SMH01**-**SMH17**) were characterized by FTIR, ^{1}H & ^{13}C NMR analysis. The spectral data of the first and second intermediate (**SME IM 01** & **SME IM 02**) are given below. The first intermediate was confirmed by the presence of signals at δ 5.95 ppm, δ 4.56 ppm and δ 4.29 ppm which correspond to dioxole methylene protons (-O-C**H**$_2$-O), O-alkyl protons (-O-C**H**$_2$-CO) and terminal ester methylene protons (-O-C**H**$_2$-CH_3). The formation of hydrazide from ester was confirmed by the disappearance of the peak at δ 4.29 ppm and the appearance of a new peak at δ 9.29 ppm corresponding to hydrazide proton (-CO-N**H**-NH_2).

Ethyl 2-(benzo[*d*][1,3]dioxol-5-yloxy)acetate (SME IM 01): ^{1}H NMR (500 MHz, $CDCl_3$) δ 6.72 (d, J = 8.4 Hz, 1H), 6.56 (d, J = 2.5 Hz, 1H), 6.34 (dd, J = 8.5, 2.5 Hz, 1H), 5.95 (s, 2H), 4.56 (s, 2H), 4.29 (q, J = 7.1 Hz, 2H), 1.32 (t, J = 7.2 Hz, 3H); ^{13}C NMR (126 MHz, $CDCl_3$) δ 169.02, 153.37, 148.35, 142.49, 107.91, 106.01, 101.32, 98.61, 66.52, 61.36, 14.18.

2-(benzo[*d*][1,3]dioxol-5-yloxy)acetohydrazide (SME IM 02): ^{1}H NMR (500 MHz, DMSO) δ 9.29 (s, 1H), 6.81 (d, J = 8.4 Hz, 1H), 6.67 (d, J = 2.6 Hz, 1H), 6.39 (dd, J = 8.5, 2.6 Hz, 1H), 5.96 (s, 2H), 4.40 (s, 2H), 4.32 (s, 2H); ^{13}C NMR (126 MHz, DMSO) δ 167.11, 153.66, 148.28, 142.02, 108.41, 106.46, 101.55, 98.59, 67.62.

The NMR analysis of all the compounds indicated the presence of rotational isomers or rotamers (*synperiplanar* or *antiperiplanar,* **Figure 3.5**) in varying ratios of *syn* to *anti* isomer. The rotamerism in the acyl hydrazones has previously been reported by Munir *et al.*, where a key stereochemical factor was ascertained to be restricted rotation about the C-N bond of the amide linkage, C(O)NH. The theoretical possibility of geometrical isomers (*E* and *Z* isomer) due to rotation about imine C=N bond which is not favored in our study due to steric overcrowding (**Figure 3.5**) and also due to the absence of intramolecular hydrogen bonding of *Z*-isomer in polar solvent like DMSO-d_6 [183-185]. In the current study, we did not observe *Z*-isomer in any of our molecules of the library even in low polarity solvents like $CDCl_3$ suggesting the predominant steric effect which means only *E*-isomer is the dominant outcome. To further infer the above scenario, it can be pointed out that NH protons of *Z*-isomers of acyl hydrazones are reported to have chemical shift around δ 14 ppm, whereas not even a single compound of our library has displayed a signal in this region [186]. Finally, the presence of *Z*-isomer was unequivocally ruled out by the results of thin-layer chromatography of each compound where only a single spot was obtained [187].

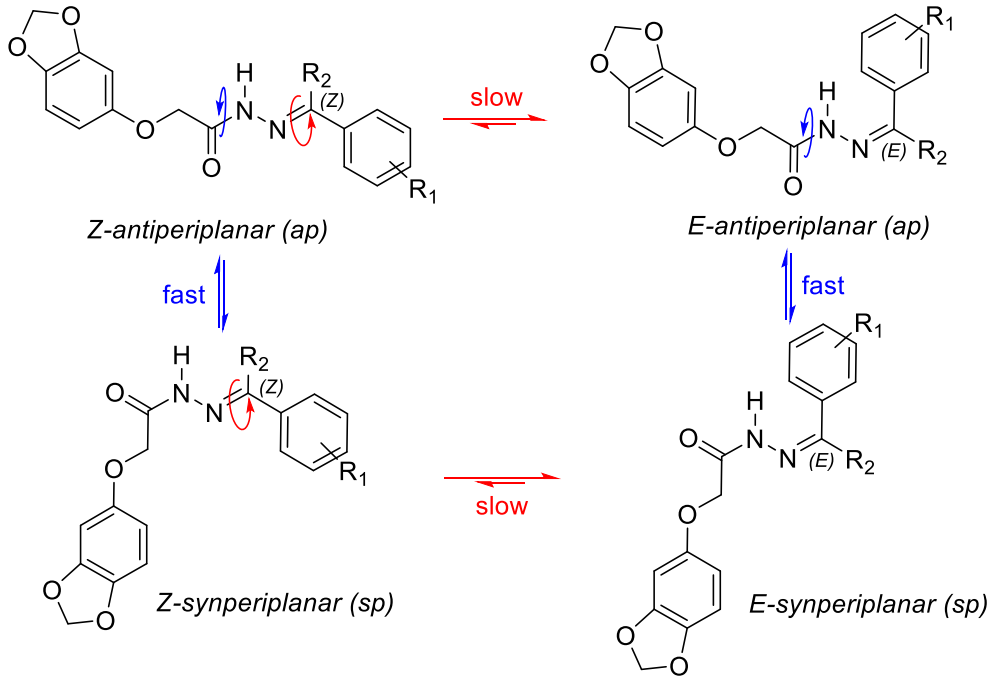

Figure 3.5. Possible rotational isomers in the synthesized compounds arising due to C-N bond and -CO-NH bond rotation.

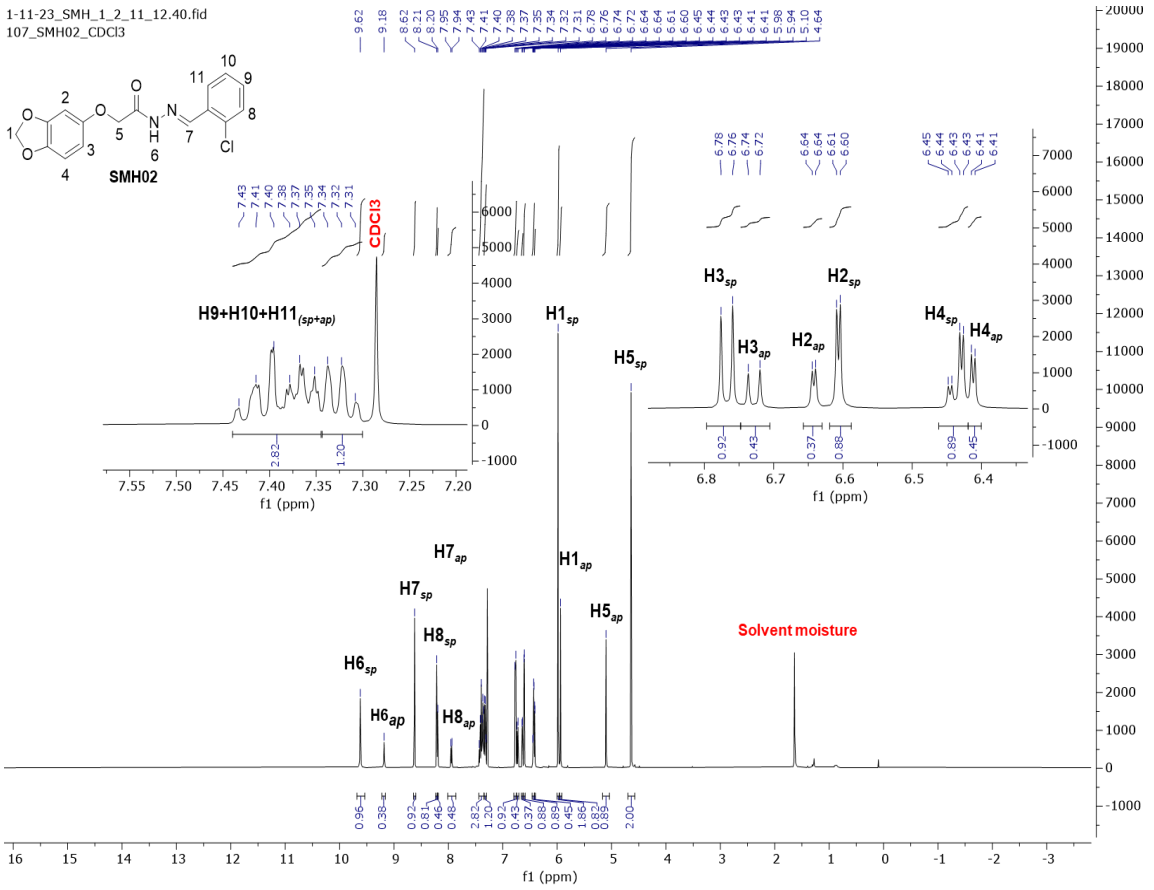

Figure 3.6. Representative ^{1}H NMR spectrum of compound **SMH02** in $CDCl_3$ displays the *synperiplanar (sp) and antiperiplanar (ap)* signals. The H-suffix denotes the same protons as mentioned in the structure of the compound **SMH02** in the inset of the figure.

All the duplicated signals/peaks observed in the ^{1}H NMR spectroscopy of compounds **SMH01-SMH17** are listed in **Table 3.3**. A separate set of signals was observed for the amide -C(O)-NH, imine -N=C**H**, methylene -C**H**$_2$-CO protons, and dioxole -O-C**H**$_2$-O. All other protons of individual functional groups in different analogs displayed signal duplicity in the same way. The ratio of rotamer was not dependent on the NMR solvent and was purely due to the electronegative and steric effect of substituents. Each analog displayed a different ratio of *syn* vs. *anti* isomer.

Table 3.3. Chemical shift of duplicated signals/peaks in ^{1}H NMR of compounds **SMH01-SMH17**

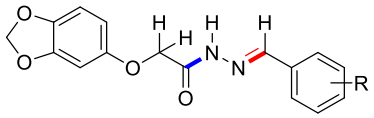

SMH01-SMH12

SMH13-SMH17

Compound Details			**Chemical Shift δ (ppm)**									
Compd. code	**R**	**NMR Solvent**	-C(O)-N**H**-		-N=C**H**/N=C(C**H**$_3$)		-O-C**H**$_2$-O-		-C**H**$_2$-CO-		Ar-**H** **Range**	**Ratio (*syn:anti*)**
			syn-	***anti-***	***syn-***	***anti-***	***syn-***	***anti-***	***syn-***	***anti-***		
SMH01	H	$CDCl_3$	8.35	--[a]	8.00	--[b]	5.96	5.97	5.05	4.58	6.35-7.70	1:0.7
SMH02	2-Cl	DMSO-d_6	9.62	9.18	8.62	8.21	5.98	5.94	4.64	5.10	6.41-8.20	1:0.4
SMH03	4-Cl	$CDCl_3$	9.46	9.34	8.24	7.77	5.98	5.94	4.63	5.10	6.40-7.74	1:0.4
SMH04	2,3-Cl_2	DMSO-d_6	11.82	11.88	8.40	8.79	5.96	5.98	5.09	4.62	6.37-8.00	1:0.6
SMH05	2,4-Cl_2	DMSO-d_6	11.79	11.83	8.71	8.33	5.96	5.98	5.08	4.61	6.36-8.03	1:0.7
SMH06	2,6-Cl_2	$CDCl_3$	9.42	9.69	8.07	8.55	5.93	5.99	5.08	4.64	6.40-7.42	1:0.8
SMH07	2-OH	DMSO-d_6	11.76	11.51	8.58	8.31	5.98	5.96	4.62	5.03	6.36-7.71	1:0.6
SMH08	4-OH	DMSO-d_6	11.36	11.30	7.90	8.23	5.96	5.98	5.02	4.55	6.35-7.54	1:0.8
SMH09	4-OCH_3	$CDCl_3$	9.38	--[a]	8.17	--[b]	5.98	5.93	4.61	5.10	6.41-7.75	1:0.5
SMH10	4-NO_2	DMSO-d_6	11.86	11.83	8.10	8.45	5.97	5.98	5.11	4.63	6.38-8.30	1:0.7
SMH11	3-Pyridyl	$CDCl_3$	9.74	10.50	8.35	7.91	5.96	5.92	4.51	4.62	6.37-8.83	1:0.7
SMH12	2-Furfuryl	$CDCl_3$	9.58	10.31	8.36	7.77	5.96	5.92	4.59	5.08	6.36-7.54	1:0.6
SMH13	H	$CDCl_3$	9.10	9.40	2.26	2.30	5.93	5.98	5.14	4.67	6.41-7.87	1:0.9
SMH14	4-F	$CDCl_3$	9.37	8.97	2.28	2.24	5.99	5.94	4.67	5.12	6.41-7.87	1:0.8
SMH15	4-Cl	$CDCl_3$	9.37	8.87	2.25	2.21	5.96	5.91	4.64	5.09	6.38-7.79	1:0.8
SMH16	4-Br	$CDCl_3$	9.40	8.93	2.27	2.23	5.99	5.97	4.67	4.52	6.32-7.75	1:0.8
SMH17	4-NO_2	DMSO-d_6	11.08	10.74	2.32	2.36	5.97	5.97	5.14	4.73	6.36-8.28	1:0.4

[a] Very weak or no signal detected; not integrable; [b] Signal overlapped with aromatic signals

(*E*)-2-(benzo[*d*][1,3]dioxol-5-yloxy)-*N′*-benzylideneacetohydrazide (SMH01): White solid; Yield: 90 %; MP: 152-154 ˚C; R_f: 0.87 in 60 % ethyl acetate-*n*-hexane; FTIR (KBr, *v,* cm^{-1}): 2916 (cyclic CH_2 str), 1698 (C=O str), 1178 (C-O str); ^{1}H NMR (500 MHz, $CDCl_3$) δ 8.35 (s, 1H), 8.00 (s, 1H), 7.70 (s, 1H), 7.69 (s, 2H), 7.44 (d, *J* = 7.3 Hz, 3H), 7.42 (s, 2H), 6.83 (d, *J* = 8.4 Hz, 1H), 6.80 (d, *J* = 8.5 Hz, 1H), 6.71 (d, *J* = 2.6 Hz, 1H), 6.67 – 6.63 (m, 1H), 6.44 (dd, *J* = 8.5, 2.5 Hz, 1H), 6.37 (dd, *J* = 8.5, 2.5 Hz, 1H), 5.97 (s, 1H), 5.96 (s, 2H), 5.05 (s, 2H), 4.58 (s, 1H); ^{13}C NMR (126 MHz, CDCl3) δ 174.32, 171.87, 169.50, 158.90, 158.43, 158.35, 153.28, 153.13, 153.08, 148.98, 146.96, 146.78, 146.54, 139.33, 139.20, 135.40, 135.16, 134.00, 132.39, 132.18, 132.10, 113.23, 113.15, 111.32, 111.08, 106.38, 106.25, 103.42, 103.24, 72.70, 72.39, 70.81.

(*E*)-2-(benzo[*d*][1,3]dioxol-5-yloxy)-*N′*-(2-chlorobenzylidene)acetohydrazide (SMH02): White solid; Yield: 70 %; MP: 136-138 ˚C; R_f: 0.83 in 60 % ethyl acetate-*n*-hexane; FTIR (KBr, *v,* cm^{-1}): 3097 (cyclic CH_2 str), 1692 (C=O str), 1186 (C-O str); ^{1}H NMR (500 MHz, $CDCl_3$) δ 9.62 (s, 1H), 8.62 (s, 1H), 8.20 (s, 1H), 7.44 – 7.34 (m, 3H), 7.32 (t, *J* = 7.4 Hz, 1H), 6.77 (d, *J* = 8.4 Hz, 1H), 6.61 (d, *J* = 2.6 Hz, 1H), 6.44 (dd, *J* = 8.4, 2.6 Hz, 1H), 5.98 (s, 2H), 5.94 (s, 1H), 5.10 (s, 1H), 4.64 (s, 2H); ^{13}C NMR (126 MHz, $CDCl_3$) δ 169.81, 164.43, 153.75, 152.36, 148.67, 148.31, 145.66, 143.13, 141.28, 134.50, 131.70, 131.42, 130.69, 130.09, 129.79, 128.12, 127.16, 108.20, 107.92, 106.14, 101.58, 101.28, 98.73, 98.44, 68.34, 66.68.

(*E*)-2-(benzo[*d*][1,3]dioxol-5-yloxy)-*N′*-(4-chlorobenzylidene)acetohydrazide (SMH03): White solid; Yield: 91 %; MP: 161-163 ˚C; R_f: 0.85 in 60 % ethyl acetate-*n*-hexane; FTIR (KBr, *v,* cm^{-1}): 3084 (cyclic CH_2 str), 2973 (aliphatic CH_2 str), 1681 (C=O str), 1183 (C-O str); ^{1}H NMR (500 MHz, $CDCl_3$) δ 9.46 (s, 1H), 8.24 (s, 1H), 7.73 (d, *J* = 8.5 Hz, 2H), 7.61 (d, *J* = 8.5 Hz, 1H), 7.42 (d, *J* = 5.0 Hz, 2H), 7.40 (s, 1H), 6.77 (d, *J* = 8.4 Hz, 1H), 6.58 (d, *J* = 2.6 Hz, 1H), 6.40 (d, *J* = 8.5 Hz, 1H), 5.98 (s, 2H), 5.94 (s, 1H),

5.10 (s, 1H), 4.63 (s, 2H); ^{13}C NMR (126 MHz, $CDCl_3$) δ 164.39, 152.31, 148.68, 148.16, 143.13, 136.84, 131.74, 129.21, 129.10, 129.02, 128.42, 108.22, 107.94, 106.28, 106.09, 101.59, 101.30, 98.71, 98.36, 68.30, 66.64.

(*E*)-2-(benzo[*d*][1,3]dioxol-5-yloxy)-*N′*-(2,3-dichlorobenzylidene)acetohydrazide (SMH04): White solid; Yield: 90 %; MP: 140-142 ˚C; R_f: 0.77 in 60 % ethyl acetate-*n*-hexane; FTIR (KBr, *v,* cm^{-1}): 3446 (N-H str), 3062 (cyclic CH_2 str), 1654 (C=O str), 1191 (C-O str); ^{1}H NMR (500 MHz, DMSO) δ 11.86 (s, 1H), 11.82 (s, 1H), 8.79 (s, 1H), 8.40 (s, 1H), 7.99 (d, *J* = 9.5 Hz, 1H), 7.93 (d, *J* = 7.9 Hz, 1H), 7.72 (d, *J* = 6.4 Hz, 1H), 7.69 (s, 1H), 7.46 (d, *J* = 7.5 Hz, 1H), 7.42 (d, *J* = 7.8 Hz, 1H), 6.85 (d, *J* = 8.4 Hz, 1H), 6.80 (d, *J* = 8.5 Hz, 1H), 6.73 (d, *J* = 2.6 Hz, 1H), 6.67 (d, *J* = 2.4 Hz, 1H), 6.45 (dd, *J* = 8.5, 2.6 Hz, 1H), 6.38 (dd, *J* = 8.5, 2.6 Hz, 1H), 5.98 (s, 1H), 5.96 (s, 2H), 5.09 (s, 2H), 4.62 (s, 1H); ^{13}C NMR (126 MHz, DMSO) δ 169.85, 165.17, 154.07, 153.51, 148.39, 148.32, 144.18, 141.81, 140.00, 134.35, 134.16, 132.83, 131.26, 128.86, 126.04, 108.57, 106.27, 101.65, 101.51, 98.80, 98.59, 98.37, 67.95, 66.05.

(*E*)-2-(benzo[*d*][1,3]dioxol-5-yloxy)-*N′*-(2,4-dichlorobenzylidene)acetohydrazide (SMH05): White solid; Yield: 89 %; MP: 110-112 ˚C; R_f: 0.76 in 60 % ethyl acetate-*n*-hexane; FTIR (KBr, *v,* cm^{-1}): 3567 (N-H str), 2897 (cyclic CH_2 str), 2787 (aliphatic CH_2 str), 1665 (C=O str), 1184 (C-O str); ^{1}H NMR (500 MHz, DMSO) δ 11.83 (s, 1H), 11.79 (s, 1H), 8.71 (s, 1H), 8.33 (s, 1H), 8.03 (d, *J* = 8.5 Hz, 1H), 7.97 (d, *J* = 8.7 Hz, 1H), 7.72 (d, *J* = 2.1 Hz, 1H), 7.71 (d, *J* = 2.0 Hz, 1H), 7.51 (d, *J* = 6.6 Hz, 1H), 7.49 (s, 1H), 6.84 (d, *J* = 8.5 Hz, 1H), 6.80 (d, *J* = 8.5 Hz, 1H), 6.72 (d, *J* = 2.6 Hz, 1H), 6.66 (s, 1H), 6.44 (dd, *J* = 8.5, 2.6 Hz, 1H), 6.38 (dd, *J* = 8.5, 2.6 Hz, 1H), 5.98 (s, 1H), 5.96 (s, 2H), 5.08 (s, 2H), 4.61 (s, 1H); ^{13}C NMR (126 MHz, DMSO) δ 169.79, 165.10, 154.07, 153.52, 148.38, 148.31, 143.33, 143.27, 142.25, 141.80, 139.24, 139.11, 135.69, 135.42, 134.42, 131.00,

130.82, 129.94, 129.71, 128.82, 128.67, 128.45, 128.34, 108.56, 108.48, 108.31, 106.70, 106.50, 106.27, 101.65, 101.51, 101.40, 98.79, 98.58, 98.36, 67.95, 66.04.

(*E*)-2-(benzo[*d*][1,3]dioxol-5-yloxy)-*N′*-(2,6-dichlorobenzylidene)acetohydrazide (SMH06): White solid; Yield: 85 %; MP: 155-157 ˚C; R_f: 0.76 in 60 % ethyl acetate-*n*-hexane; FTIR (KBr, *v,* cm^{-1}): 3202 (N-H str), 2908 (cyclic CH_2 str), 1693 (C=O str), 1181 (C-O str); ^{1}H NMR (500 MHz, $CDCl_3$) δ 9.69 (s, 1H), 9.42 (s, 1H), 8.55 (s, 1H), 8.07 (s, 1H), 7.41 (d, *J* = 8.1 Hz, 2H), 7.38 (d, *J* = 7.9 Hz, 2H), 7.28 – 7.27 (m, 1H), 7.27 – 7.24 (m, 1H), 6.77 (d, *J* = 8.4 Hz, 1H), 6.71 (d, *J* = 8.5 Hz, 1H), 6.62 (d, *J* = 2.6 Hz, 1H), 6.61 (d, *J* = 2.6 Hz, 1H), 6.44 – 6.42 (m, 1H), 6.41 (d, *J* = 6.0 Hz, 1H), 5.99 (s, 2H), 5.93 (s, 2H), 5.08 (s, 2H), 4.64 (s, 2H); ^{13}C NMR (126 MHz, $CDCl_3$) δ 170.41, 164.52, 153.70, 152.31, 148.66, 148.29, 144.84, 142.26, 135.28, 135.16, 130.67, 129.22, 128.79, 101.58, 101.25, 98.53, 68.35, 66.54; HPLC purity: 98.39 %.

(*E*)-2-(benzo[*d*][1,3]dioxol-5-yloxy)-*N′*-(2-hydroxybenzylidene)acetohydrazide (SMH07): Off white solid; Yield: 88 %; MP: 138-140 ˚C; R_f: 0.57 in 60 % ethyl acetate-*n*-hexane; FTIR (KBr, *v,* cm^{-1}): 3096 (cyclic CH_2 str), 2989 (aliphatic CH_2 str), 1673 (C=O str), 1186 (C-O str); ^{1}H NMR (500 MHz, DMSO) δ 11.76 (s, 1H), 11.51 (s, 1H), 11.07 (s, 1H), 10.05 (s, 1H), 8.58 (s, 1H), 8.31 (s, 1H), 7.70 (d, *J* = 9.6 Hz, 1H), 7.53 (d, *J* = 7.6 Hz, 1H), 7.30 (t, *J* = 6.9 Hz, 1H), 7.25 (t, *J* = 7.7 Hz, 1H), 6.95 – 6.91 (m, 2H), 6.91 – 6.86 (m, 1H), 6.85 (d, *J* = 8.5 Hz, 1H), 6.81 (d, *J* = 8.5 Hz, 1H), 6.73 (d, *J* = 2.4 Hz, 1H), 6.65 (d, *J* = 2.6 Hz, 1H), 6.46 (dd, *J* = 8.5, 2.6 Hz, 1H), 6.37 (dd, *J* = 8.5, 2.6 Hz, 1H), 5.98 (s, 2H), 5.96 (s, 1H), 5.03 (s, 1H), 4.62 (s, 2H); ^{13}C NMR (126 MHz, DMSO) δ 169.22, 164.69, 157.85, 156.87, 154.12, 153.53, 148.85, 148.39, 142.25, 141.95, 141.80, 132.00, 131.65, 129.84, 129.71, 120.46, 119.92, 119.78, 119.08, 116.93, 116.79, 116.51, 108.56, 108.49, 108.40, 106.71, 106.48, 106.18, 101.65, 101.50, 98.79, 98.60, 98.35, 67.84, 66.12.

(*E*)-2-(benzo[*d*][1,3]dioxol-5-yloxy)-*N′*-(4-hydroxybenzylidene)acetohydrazide (SMH08): White solid; Yield: 93 %; MP: 209-211 ˚C; R_f: 0.56 in 60 % ethyl acetate-*n*-hexane; FTIR (KBr, *v,* cm^{-1}): 3662 (N-H str), 2884 (aliphatic CH_2 str), 1660 (C=O str), 1186 (C-O str); ^{1}H NMR (500 MHz, DMSO) δ 11.36 (s, 1H), 11.30 (s, 1H), 9.94 (s, 1H), 9.90 (s, 1H), 8.23 (s, 1H), 7.90 (s, 1H), 7.54 (s, 2H), 7.52 (s, 2H), 6.84 (d, *J* = 2.4 Hz, 1H), 6.83 (d, *J* = 2.6 Hz, 2H), 6.81 (s, 1H), 6.80 (s, 1H), 6.71 (s, 1H), 6.64 (s, 1H), 6.43 (dd, *J* = 8.5, 2.6 Hz, 1H), 6.36 (dd, *J* = 8.4, 2.6 Hz, 1H), 5.02 (s, 2H), 4.55 (s, 2H); ^{13}C NMR (126 MHz, DMSO) δ 169.19, 164.32, 159.97, 159.74, 154.17, 153.61, 148.82, 148.31, 144.61, 144.44, 142.17, 141.75, 129.43, 129.16, 125.46, 116.21, 116.05, 108.48, 108.32, 106.38, 106.16, 101.72, 101.62, 101.49, 98.75, 98.56, 98.35, 67.94, 66.01.

(*E*)-2-(benzo[*d*][1,3]dioxol-5-yloxy)-*N′*-(4-methoxybenzylidene)acetohydrazide (SMH09): White solid; Yield: 91 %; MP: 128-130 ˚C; R_f: 0.52 in 60 % ethyl acetate-*n*-hexane; FTIR (KBr, *v,* cm^{-1}): 2965 (cyclic CH_2 str), 2867 (aliphatic CH_2 str), 1668 (C=O str), 1168 (C-O str); ^{1}H NMR (500 MHz, $CDCl_3$) δ 9.36 (s, 1H), 8.17 (s, 1H), 7.77 – 7.71 (m, 2H), 7.61 (d, *J* = 8.9 Hz, 1H), 6.96 (d, *J* = 6.1 Hz, 2H), 6.93 (s, 1H), 6.76 (d, *J* = 8.4 Hz, 1H), 6.58 (s, 1H), 6.41 (d, *J* = 8.4 Hz, 1H), 5.98 (s, 2H), 5.93 (s, 1H), 5.10 (s, 1H), 4.61 (s, 2H), 3.88 (s, 1H), 3.87 (s, 3H); ^{13}C NMR (126 MHz, $CDCl_3$) δ 164.10, 161.85, 152.44, 149.33, 143.05, 129.55, 128.86, 125.84, 114.34, 114.23, 108.20, 107.92, 106.29, 106.13, 101.54, 101.25, 98.71, 98.38, 68.34, 66.64, 55.39.

(*E*)-2-(benzo[*d*][1,3]dioxol-5-yloxy)-*N′*-(4-nitrobenzylidene)acetohydrazide (SMH10): Pale yellow solid; Yield: 92 %; MP: 170-172 ˚C; R_f: 0.88 in 60 % ethyl acetate-*n*-hexane; FTIR (KBr, *v,* cm^{-1}): 965 (cyclic CH_2 str), 1681 (C=O str), 1187 (C-O str); ^{1}H NMR (500 MHz, DMSO) δ 11.86 (s, 1H), 11.83 (s, 1H), 8.45 (s, 1H), 8.29 (d, *J* = 8.9 Hz, 1H), 8.27 (d, *J* = 8.9 Hz, 2H), 8.10 (s, 1H), 7.98 (s, 1H), 7.96 (d, *J* = 7.5 Hz, 2H), 6.84 (d, *J* = 8.5 Hz, 1H), 6.81 (d, *J* = 8.4 Hz, 1H), 6.72 (d, *J* = 2.6 Hz, 1H), 6.67 (d, *J* = 2.6 Hz, 1H), 6.44 (d, *J*

= 8.5 Hz, 1H), 6.41 – 6.37 (m, 1H), 5.98 (s, 1H), 5.97 (s, 2H), 5.11 (s, 2H), 4.63 (s, 1H); ^{13}C NMR (126 MHz, DMSO) δ 170.00, 165.26, 154.07, 153.53, 148.39, 148.21, 146.02, 142.24, 141.83, 140.90, 140.75, 128.63, 128.45, 128.26, 124.59, 124.36, 108.48, 108.31, 106.67, 106.51, 106.27, 101.65, 101.52, 98.76, 98.59, 98.38, 67.89, 66.05, 65.87.

(*E*)-2-(benzo[*d*][1,3]dioxol-5-yloxy)-*N*′-(pyridin-3-ylmethylene)acetohydrazide (SMH11): White solid; Yield: 70 %; MP: 141-143 ˚C; R_f: 0.85 in 60 % ethyl acetate-*n*-hexane; FTIR (KBr, *v,* cm^{-1}): 2989 (cyclic CH_2 str), 1683 (C=O str), 1189 (C-O str); ^{1}H NMR (500 MHz, $CDCl_3$) δ 10.50 (s, 1H), 9.74 (s, 1H), 8.83 (d, *J* = 1.5 Hz, 1H), 8.82 (d, *J* = 1.5 Hz, 1H), 8.66 (dd, *J* = 3.2, 1.7 Hz, 1H), 8.65 (d, *J* = 1.7 Hz, 1H), 8.35 (s, 1H), 8.22 (dt, *J* = 8.1, 2.0 Hz, 1H), 8.00 (dt, *J* = 7.9, 2.0 Hz, 1H), 7.91 (s, 1H), 7.38 (d, *J* = 7.2 Hz, 1H), 7.37 – 7.34 (m, 1H), 6.74 (d, *J* = 8.5 Hz, 1H), 6.72 (d, *J* = 8.5 Hz, 1H), 6.63 (d, *J* = 2.4 Hz, 1H), 6.56 (d, *J* = 2.6 Hz, 1H), 6.42 (dd, *J* = 8.5, 2.6 Hz, 1H), 6.39 (dd, *J* = 8.5, 2.6 Hz, 1H), 5.96 (s, 2H), 5.92 (s, 1H), 5.11 (s, 1H), 4.62 (s, 2H); ^{13}C NMR (126 MHz, $CDCl_3$) δ 170.91, 164.69, 153.66, 152.30, 151.57, 151.23, 149.69, 149.06, 148.65, 148.35, 146.39, 143.11, 142.44, 133.97, 133.64, 129.43, 129.29, 123.81, 108.24, 107.99, 107.90, 106.09, 106.01, 101.58, 101.33, 98.71, 98.42, 98.32, 68.28.

(*E*)-2-(benzo[*d*][1,3]dioxol-5-yloxy)-*N*′-(furan-2-ylmethylene)acetohydrazide (SMH12): Off white solid; Yield: 92 %; MP: 125-127 ˚C; R_f: 0.89 in 60 % ethyl acetate-*n*-hexane; FTIR (KBr, *v,* cm^{-1}): 3262 (N-H str), 2913 (cyclic CH_2 str), 1669 (C=O str), 1195 (C-O str); ^{1}H NMR (500 MHz, $CDCl_3$) δ 10.31 (s, 1H), 9.58 (s, 1H), 8.36 (s, 1H), 7.77 (s, 1H), 7.54 (s, 1H), 7.54 (s, 1H), 6.85 (d, *J* = 3.5 Hz, 1H), 6.63 (d, *J* = 2.4 Hz, 1H), 6.55 (d, *J* = 2.6 Hz, 1H), 6.51 (d, *J* = 1.5 Hz, 1H), 6.51 – 6.49 (m, 1H), 6.43 (dd, *J* = 8.5, 2.6 Hz, 1H), 6.37 (dd, *J* = 8.4, 2.6 Hz, 1H), 5.96 (s, 2H), 5.92 (s, 1H), 5.08 (s, 1H), 4.59 (s, 2H); ^{13}C NMR (126 MHz, $CDCl_3$) δ 164.58, 153.71, 152.37, 148.88, 148.27, 145.07, 144.75,

143.01, 142.29, 139.56, 114.18, 112.13, 108.21, 107.85, 106.34, 105.99, 101.54, 101.26, 98.66, 98.30, 68.25, 66.47.

(*E*)-2-(benzo[*d*][1,3]dioxol-5-yloxy)-*N′*-(1-phenylethylidene)acetohydrazide (SMH13): Colorless crystals; Yield: 76 %; MP: 112-114 ˚C; R_f: 0.71 in 60 % ethyl acetate-*n*-hexane; FTIR (KBr, *v,* cm^{-1}): 3205 (N-H str), 2906 (cyclic CH_2 str), 1675 (C=O str), 1180 (C-O str); ^{1}H NMR (500 MHz, $CDCl_3$) δ 9.40 (s, 1H), 9.10 (s, 1H), 7.88 – 7.84 (m, 2H), 7.77 – 7.72 (m, 2H), 7.46 – 7.43 (m, 3H), 7.41 (dd, *J* = 5.2, 2.0 Hz, 3H), 6.77 (d, *J* = 8.5 Hz, 1H), 6.73 (d, *J* = 8.5 Hz, 1H), 6.64 (d, *J* = 2.6 Hz, 1H), 6.59 (d, *J* = 2.6 Hz, 1H), 6.45 – 6.43 (m, 1H), 6.43 – 6.40 (m, 1H), 5.98 (s, 2H), 5.93 (s, 2H), 5.14 (s, 2H), 4.67 (s, 2H), 2.30 (s, 3H), 2.26 (s, 3H).

^{13}C NMR (126 MHz, $CDCl_3$) δ 170.46, 164.04, 153.84, 152.36, 148.80, 148.27, 143.08, 142.22, 137.43, 129.74, 128.59, 126.83, 126.20, 108.29, 106.03, 101.59, 101.25, 98.70, 98.34, 98.23, 68.49, 66.91, 13.32, 12.73.

(*E*)-2-(benzo[*d*][1,3]dioxol-5-yloxy)-*N′*-(1-(4-fluorophenyl)ethylidene)acetohydrazide (SMH14): White solid; Yield: 72 %; MP: 132-134 ˚C; R_f: 0.72 in 60 % ethyl acetate-*n*-hexane; FTIR (KBr, *v,* cm^{-1}): 3209 (N-H str), 1668 (C=O str), 1188 (C-O str); ^{1}H NMR (500 MHz, $CDCl_3$) δ 9.39 (s, 1H), 8.90 (s, 1H), 7.81 (d, *J* = 8.7 Hz, 2H), 7.68 (d, *J* = 8.7 Hz, 1H), 7.43 – 7.36 (m, 3H), 6.77 (d, *J* = 8.4 Hz, 1H), 6.73 (d, *J* = 8.5 Hz, 1H), 6.63 (s, 1H), 6.58 (s, 1H), 6.42 (t, *J* = 5.9 Hz, 2H), 5.98 (s, 2H), 5.94 (s, 1H), 5.11 (s, 1H), 4.67 (s, 2H), 2.27 (s, 3H), 2.23 (s, 2H); ^{13}C NMR (126 MHz, $CDCl_3$) δ 164.06, 135.84, 128.81, 128.66, 128.07, 127.42, 108.25, 107.92, 106.30, 106.14, 101.60, 101.26, 98.68, 98.29, 68.53, 66.83, 13.08, 12.51.

(*E*)-2-(benzo[*d*][1,3]dioxol-5-yloxy)-*N′*-(1-(4-chlorophenyl)ethylidene)acetohydrazide (SMH15): White solid; Yield: 72 %; MP: 171-173 ˚C; R_f: 0.70 in 60 % ethyl acetate-*n*-

hexane; FTIR (KBr, *v,* cm^{-1}): 1656 (C=O str), 1190 (C-O str); ^{1}H NMR (500 MHz, $CDCl_3$) δ 9.37 (s, 1H), 8.87 (s, 1H), 7.78 (d, *J* = 8.7 Hz, 2H), 7.66 (d, *J* = 8.7 Hz, 2H), 7.38 (d, *J* = 8.7 Hz, 2H), 7.36 (d, *J* = 8.7 Hz, 2H), 6.74 (d, *J* = 8.4 Hz, 1H), 6.70 (d, *J* = 8.5 Hz, 1H), 6.61 (d, *J* = 2.6 Hz, 1H), 6.56 (d, *J* = 2.6 Hz, 1H), 6.43 – 6.40 (m, 1H), 6.40 – 6.37 (m, 1H), 5.96 (s, 2H), 5.91 (s, 2H), 5.09 (s, 2H), 4.64 (s, 2H), 2.25 (s, 3H), 2.21 (s, 3H), 2.17 (s, 1H); ^{13}C NMR (126 MHz, $CDCl_3$) δ 164.06, 135.84, 128.81, 128.66, 128.07, 127.42, 108.25, 107.92, 106.30, 106.14, 101.60, 101.26, 98.68, 98.29, 68.53, 66.83, 13.08, 12.51.

(*E*)-2-(benzo[*d*][1,3]dioxol-5-yloxy)-*N′*-(1-(4-bromophenyl)ethylidene)acetohydrazide (SMH16): White solid; Yield: 87 %; MP: 142-144 ˚C; R_f: 0.76 in 60 % ethyl acetate-*n*-hexane; FTIR (KBr, *v,* cm^{-1}): 3197 (N-H str), 1667 (C=O str), 1186 (C-O str); 1H NMR (500 MHz, CDCl3) δ 9.40 (s, 1H), 8.93 (s, 1H), 7.74 (d, *J* = 8.7 Hz, 3H), 7.61 (d, *J* = 8.9 Hz, 2H), 7.58 – 7.52 (m, 4H), 6.77 (d, *J* = 8.5 Hz, 1H), 6.73 (dd, *J* = 8.5, 5.0 Hz, 1H), 6.63 (s, 1H), 6.58 (s, 1H), 6.51 (d, *J* = 2.6 Hz, 1H), 6.43 (dd, *J* = 5.7, 2.5 Hz, 1H), 6.41 – 6.38 (m, 1H), 6.33 (dd, *J* = 8.5, 2.6 Hz, 1H), 5.99 (s, 2H), 5.97 (s, 2H), 5.94 (s, 2H), 5.11 (s, 2H), 4.67 (s, 2H), 4.52 (s, 2H), 2.27 (s, 3H), 2.23 (s, 2H); ^{13}C NMR (126 MHz, $CDCl_3$) δ 170.28, 168.61, 164.09, 152.29, 148.70, 148.57, 147.51, 136.26, 131.61, 128.34, 127.67, 124.48, 124.16, 101.50, 101.28, 98.33, 98.15, 68.47, 67.94; HPLC purity: 99.45 %.

(*E*)-2-(benzo[*d*][1,3]dioxol-5-yloxy)-*N′*-(1-(4-nitrophenyl)ethylidene)acetohydrazide (SMH17): Pale yellow solid; Yield: 87 %; MP: 172-174 ˚C; R_f: 0.65 in 60 % ethyl acetate-*n*-hexane; FTIR (KBr, *v,* cm^{-1}): 3181 (N-H str), 2885 (cyclic CH_2 str), 1680 (C=O str), 1170 (C-O str); ^{1}H NMR (500 MHz, DMSO) δ 11.08 (s, 1H), 8.27 (d, *J* = 9.6 Hz, 1H), 8.24 (d, *J* = 8.9 Hz, 2H), 8.07 (s, 1H), 8.05 (s, 1H), 6.80 (d, *J* = 8.5 Hz, 1H), 6.66 (d, *J* = 2.6 Hz, 1H), 6.37 (dd, *J* = 8.4, 2.6 Hz, 1H), 5.97 (s, 1H), 5.97 (s, 2H), 5.14 (s, 2H), 4.73 (s, 1H), 2.36 (s, 1H), 2.32 (s, 3H); ^{13}C NMR (126 MHz, DMSO) δ 170.75, 154.11, 148.32, 147.90,

146.56, 144.53, 141.75, 127.87, 127.72, 124.06, 123.94, 108.47, 108.31, 106.38, 106.16, 101.51, 98.54, 98.35, 66.61, 66.44, 13.96.

3.4.2. Biological Studies

3.4.2.1. *In vitro* studies

A. SMA Series

3.4.2.1.1. *In vitro* MAO inhibition assay (SMA series)

The enzyme inhibition assay of compounds **SMA01-SMA11** was performed against MAO-A and MAO-B; the obtained results indicate that most of the compounds displayed IC_{50} values less than 1 µM and ranged between 1.267 ± 0.051 µM (**SMA07**) and 0.053 ± 0.001 µM (**SMA08**) for MAO-A while for MAO-B the IC_{50} values ranged from 0.541 ± 0.020 µM (**SMA02**) to 0.019 ± 0.001 µM (**SMA05**). Compound **SMA08** (IC_{50} = 0.053 ± 0.001 µM) was identified as the most potent MAO-A inhibitor while compound **SMA05** (IC_{50} = 0.019 ± 0.001 µM) emerged as the lead MAO-B inhibitor among tested compounds. The obtained results of the *in vitro* enzyme inhibition assay are given in **Table 3.4**.

Table 3.4. *In vitro* enzyme inhibition results of compounds **SMA01-SMA11**

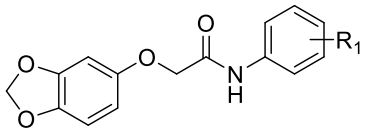

SMA01-SMA11

Compd. code	R_1	MAO-A IC_{50} (µM)[a]	MAO-B IC_{50} (µM)[a]	SI[c]	AChE IC_{50} (µM)[b]	BChE IC_{50} (µM)[b]
SMA01	H	0.064 ± 0.020	0.122 ± 0.003	0.52	9.925 ± 0.018	NT
SMA02	4-F	0.221 ± 0.094	0.541 ± 0.020	0.40	6.483 ± 1.751	NT
SMA03	4-Cl	0.830 ± 0.015	0.101 ± 0.010	8.21	9.900 ± 0.033	NT
SMA04	4-Br	1.105 ± 0.023	0.149 ± 0.006	7.41	2.541 ± 0.120	NT
SMA05	4-CH_3	1.023 ± 0.048	0.019 ± 0.001	53.84	9.889 ± 0.018	NT
SMA06	4-OCH_3	0.409 ± 0.026	0.229 ± 0.001	1.78	2.988 ± 0.286	NT
SMA07	2,4-F_2	1.267 ± 0.051	0.301 ± 0.015	4.21	6.996 ± 2.846	NT
SMA08	3,4-Cl_2	0.053 ± 0.001	0.083 ± 0.007	0.64	8.231 ± 1.658	NT
SMA09	2,4-Cl_2	0.160 ± 0.009	0.071 ± 0.002	2.25	2.611 ± 0.086	4.223 ± 0.162

SMA10	3,4-$(CH_3)_2$	1.100 ± 0.190	0.382 ± 0.034	2.88	9.887 ± 0.029	NT
SMA11	2,6-$(CH_3)_2$	1.099 ± 0.005	0.152 ± 0.005	7.23	9.919 ±0.038	NT

[a] Mean IC_{50} (μM) ± SEM of 2 independent experiments; [b] Values are the mean ± SEM of 3 independent experiments; [c] Selectivity index (SI): ratio of experimental IC_{50} (MAO-A)/IC_{50} (MAO-B); CLO = Clorgyline, SEL = Selegiline, PCPA = Tranylcypromine; NT = Not tested.

SAR of MAO-A inhibition

- The obtained IC_{50} values of the compounds (**SMA01-SMA11**) against MAO-A lies in the range of micromolar (1.267 ± 0.051 μM, compound **SMA07**) to nanomolar (0.053 ± 0.001 μM, compound **SMA08**) concentration and are shown in **Table 3.2**.
- The 3,4-dichloro analog (compound **SMA08**, 2-(benzo[*d*][1,3]dioxol-5-yloxy)-*N*-(3,4-dichlorophenyl)acetamide) emerged as the lead MAO-A inhibitor with an IC_{50} value of 0.053 ± 0.001 μM.
- The attempted modifications at the N-terminal aryl ring yielded compounds with variable MAO-A inhibitory potential.
- Introduction of mono-methyl (compound **SMA05**), dimethyl (compounds **SMA10** and **SMA11**), mono-bromo (compound **SMA04**) and difluoro (compound **SMA07**) groups significantly reduced MAO-A inhibitory activity.
- Analogs bearing 4-fluoro (compound **SMA02**), 4-chloro (compound **SMA03**), 4-methoxyl (compound **SMA06**), and 2,4-dichloro (compounds **SMA09**) groups on the aryl ring though showing inhibition activity at an IC_{50} of less than 1 μM, were less active than the parent (ring-un-substituted) analog (compound **SMA01**).
- Moreover, enrichment of the terminal aryl ring with two electronegative F atoms (compound **SMA07**) significantly decreased the inhibition activity whereas two chlorine atoms enhanced the inhibition activity.
- Notably, compounds **SMA01** and **SMA08** were relatively more potent than the reference MAO-A inhibitors, clorgyline and tranylcypromine.

SAR of MAO-B inhibition

- The compounds **SMA01-SMA11** were also assessed for their MAO-B inhibition properties, and the obtained IC_{50} values (**Table 3.2**) range from 0.019 ± 0.001 µM (compound **SMA05**) to 0.541 ± 0.020 µM (compound **SMA02**).
- In general, the compounds have displayed a better activity profile (IC_{50} less than 1 µM) against MAO-B than MAO-A. Among the tested compounds, compound **SMA05** (2-(benzo[*d*][1,3]dioxol-5-yloxy)-*N*-(*p*-tolyl)acetamide) displayed the highest inhibitory potential against MAO-B with an IC_{50} value of 0.019 ± 0.001 µM.
- Substitution of the N-terminal aryl ring with mono-methyl (compound **SMA05**) and di-chloro (compounds **SMA08** and **SMA09**) groups significantly enhanced the inhibition potency while mono-chloro substitution (compound **SMA03**) moderately enhanced the inhibition potency.
- On the other hand, substituents like 4-fluoro (compound **SMA02**), 4-bromo (compound **SMA04**), 4-methoxyl (compound **SMA06**), 2,4-difluoro (compound **SMA07**) and isomeric dimethyl groups (compounds **SMA10** and **SMA11**) decreased the MAO-B inhibition activity.
- Further, alteration of lipophilicity of the phenyl ring either by replacing the methyl group (compound **SMA05**) with a methoxy group (compound **SMA06**) or incorporating additional methyl groups (compounds **SMA10** and **SMA11**) drastically decreased the MAO-B inhibition activity.
- The lead MAO-B inhibitor (compound **SMA05**) was slightly more potent than the reference MAO-B inhibitor selegiline.

- These results suggest that the enhanced lipophilicity of the N-terminal aryl ring, either with a 4-methyl group or isomeric di-chloro groups, highly favored the MAO-B inhibitory activity of the tested sesamol-derived acetamides.

3.4.2.1.2. *In vitro* ChEs inhibition assay (SMA series)

SAR of ChE inhibition

- The compounds **SMA01-SMA11** were also evaluated for their inhibition activity against *ee*AChE and the obtained inhibition data are shown in **Table 3.2**. Compared to MAOs, the compounds were less potent against AChE and the IC_{50} values range from 2.541 ± 0.120 µM (compound **SMA04**) to 9.925 ± 0.018 µM (compound **SMA01**).
- Among the tested compounds, compound **SMA04** (2-(benzo[*d*][1,3]dioxol-5-yloxy)-*N*-(4-bromophenyl)acetamide) showed the most potent activity against AChE with an IC_{50} value of 2.541 ± 0.120 µM.
- Variations attempted on the N-terminal aryl ring highly influenced the AChE inhibition activity of compounds. Alteration of lipophilicity by the introduction of mono-chloro (compound **SMA03**), mono-methyl (compound **SMA05**) and isomeric dimethyl groups (compounds **SMA10** and **SMA11**) at the terminal aryl ring did not alter the inhibition activity.
- However, analogs bearing mono-fluoro (compound **SMA02**), and di-fluoro groups (compound **SMA07**) were more potent than the mono- and di-methyl analogs (compound **SMA02** and **SMA07**).
- Replacement of the methyl group (compound **SMA05**) with the methoxy group has significantly enhanced the activity of the resulting compound (compound **SMA06**).

- The introduction of additional chlorine atoms on the terminal aryl ring produced compounds with improved activity (compare compound **SMA08** and **SMA09** with compound **SMA03**).

SAR of dual MAO-AChE inhibition

- Analysis of the activity profile of compounds against both MAOs and ChEs led to the following observations. The R-unsubstituted parent compound (compound **SMA01**) exhibited better activity against MAO-A and was more potent than the reference inhibitor, clorgyline.
- Substitution of the N-terminal aryl ring with 4-fluoro or 2,4-difluoro groups relatively decreased the MAO inhibitory activity, while these variations resulted in an enhanced AChE inhibition activity.
- The incorporation of the 4-chloro group (compound **SMA03**) at the aryl ring caused a 13-fold reduction in MAO-A inhibition activity but did not alter the MAO-B and AChE inhibitory activity.
- Further, introducing a heavier electronegative atom (Br) reduced the MAO-A inhibition activity but increased the AChE inhibition activity (~4-fold).
- The inclusion of the steric methyl group (compound **SMA05**) significantly attenuated the MAO-A inhibition activity (~16-fold) but enhanced the MAO-B inhibition activity (~4-fold).
- However, enrichment of the lipophilicity of the aryl ring with two steric methyl groups (compounds **SMA10** and **SMA11**) decreased MAO-A inhibition activity, but this did not affect the MAO-B and AChE inhibition activity.
- Further, the replacement of the methyl group (sigma donor, compound **SMA06**) with the methoxy group (pi donor, compound **SMA06**) at the aryl ring enhanced the AChE inhibition activity (~3-fold) but decreased MAO-B inhibition activity.

- Among the isomeric dichloro substituted analogs (compounds **SMA08** and **SMA09**), the 3,4-dichloro analog (compound **SMA08**) displayed non-selective MAO inhibition activity.
- In contrast, the 2,4-dichloro analog (compound **SMA09**) displayed superior MAO-B and AChE inhibition activity compared to its parent analog (compound **SMA01**) and, thus, emerged as the lead dual MAO-B and AChE inhibitor of the series.

Moreover, the potency of this lead inhibitor (compound **SMA09**) was higher against both MAO-A and B compared to its analogous carbohydrazone derivative (compound **I** shown in **Figure 3.1**) reported earlier. However, this compound was less potent against AChE (~54-fold) and BuChE (~4.8-fold) than compound **I**. These results altogether suggest that the replacement of a 4-atom carbohydrazone linker consisting of three H-bonding atoms and a pi-donor group (compound **I**) with a 4-atom linker (compound **SMA09**) with less or altered H-bonding features significantly enhanced the MAO inhibition activity but decreased the ChE inhibition properties. From these observations, it can be concluded that a linker enriched with a higher degree of H-bonding (H-bond acceptor and donor atoms) features that bridges two distinct hydrophobic binding sites, one being a larger site and another being a smaller moiety, is highly desired for the potent MAO-A and B inhibition activity. In contrast, a linker endowed with rich H-bonding features and a pi-donor group is crucial for potent ChE inhibition activity.

B. SMH Series

3.4.2.1.3. *In vitro* MAO inhibition assay (SMH series)

The *in vitro* enzyme inhibition studies for compounds **SMH01-SMH17** were carried out against MAO-A and MAO-B enzymes and obtained results indicate that most of the compounds displayed IC_{50} values ranging from 14.275 ± 0.015 μM (compound **SMH17**) to 0.076 ± 0.009 μM (compound **SMH07**) against MAO-A while compound **SMH07** was

identified as most potent compound among all the test ligands with an IC_{50} value of 0.076 ± 0.009 μM (more potent than its reference inhibitor, clorgyline). However, the obtained IC_{50} for MAO-B ranged from 10.405 ± 0.085 μM (compound **SMH16**) to 0.064 ± 0.003 μM (compound **SMH06**). Compound **SMH06** emerged as the lead MAO-B inhibitor among all the tested molecules with an IC_{50} value of 0.064 ± 0.003 μM. The obtained results are listed in the **Table 3.5**.

Table 3.5. *In vitro* enzyme inhibition results of compounds **SMH01-SMH17**

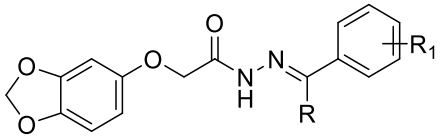

Compd. code	R	R_1	MAO-A IC_{50} (μM)[a]	MAO-B IC_{50} (μM)[a]	SI[c]	AChE IC_{50} (μM)[b]	BChE IC_{50} (μM)[b]
SMH01	H	H	4.930 ± 0.278	9.761 ± 0.080	0.51	1.341 ± 0.008	NT
SMH02	H	2-Cl	2.958 ± 0.113	3.915 ± 0.111	0.76	1.395 ± 0.025	NT
SMH03	H	4-Cl	3.249 ± 0.011	0.363 ± 0.016	8.95	1.316 ± 0.001	NT
SMH04	H	2,3-Cl_2	10.160 ± 0.040	0.654 ± 0.047	15.54	1.367 ± 0.007	NT
SMH05	H	2,4-Cl_2	3.598 ± 0.200	0.104 ± 0.005	34.60	1.375 ± 0.015	NT
SMH06	H	2,6-Cl_2	11.145 ± 0.305	0.064 ± 0.003	174.14	1.555 ± 0.013	9.936 ± 0.105
SMH07	H	2-OH	0.076 ± 0.009	0.655 ± 0.010	0.12	1.396 ± 0.003	NT
SMH08	H	4-OH	0.439 ± 0.060	1.622 ± 0.097	0.27	1.325 ± 0.012	NT
SMH09	H	4-OCH_3	0.313 ± 0.041	2.380 ± 0.114	0.13	1.399 ± 0.001	NT
SMH10	H	4-NO_2	8.959 ± 0.432	2.822 ± 0.059	3.17	1.257 ± 0.001	NT
SMH11	H	3-Pyridyl	0.637 ± 0.010	0.568 ± 0.044	1.12	1.269 ± 0.001	NT
SMH12	H	2-furfuryl	0.607 ± 0.063	0.832 ± 0.035	0.73	1.227 ± 0.001	NT
SMH13	CH_3	H	0.246 ± 0.012	2.222 ± 0.059	0.11	1.346 ± 0.008	NT
SMH14	CH_3	4-F	0.712 ± 0.080	0.283 ± 0.026	2.52	1.297 ± 0.011	NT
SMH15	CH_3	4-Cl	0.847 ± 0.041	1.933 ± 0.027	0.44	1.370 ± 0.002	NT
SMH16	CH_3	4-Br	14.275 ± 0.015	10.405 ± 0.085	1.37	1.342 ± 0.009	NT
SMH17	CH_3	4-NO_2	9.670 ± 0.067	5.894 ±0.203	1.64	1.565 ± 0.007	NT
Compd I	-	-	3.58 ± 0.98	0.95 ± 0.12	-	0.048 ± 0.007	0.89 ± 0.018
CLO	-	-	0.096 ± 0.003	-	-	-	-
SEL	-	-	-	0.021 ± 0.002	-	-	-

PCPA	-	-	0.141 ± 0.002	0.201 ± 0.001	0.70	-	-
DPZ	-	-	-	-	-	0.084 ± 0.002	1.597 ± 0.034

[a] Mean IC_{50} (µM) ± SEM of 2 independent experiments; [b] Values are the mean ± SEM of 3 independent experiments; [c] Selectivity index (SI): ratio of experimental IC_{50} (MAO-A)/IC_{50} (MAO-B); CLO = Clorgyline, SEL = Selegiline, PCPA = Tranylcypromine; NT = Not tested.

SAR of MAO-A inhibition

- The attempted modification at the N-terminal aryl ring yielded compounds with variable MAO-A inhibitory potential. 2-hydroxy analog (**SMH07**) has emerged as the lead MAO-A inhibitor with an IC_{50} value of 0.076 ± 0.009 µM.
- Introduction of mono chloro group at *ortho* and *para* position of terminal aryl ring resulted in (**SMH02** & **SMH03**) increased MAO-A inhibition compared to unsubstituted analog (**SMH01**).
- Further, analogs with dichloro substitution at 2,3 and 2,6 positions (**SMH04** & **SMH06**) drastically reduced MAO-A inhibitory activity while 2,4-dichloro substitution (**SMH05**) slightly favored MAO-A inhibition.
- Substitution of hydroxy or methoxy at *para* position (**SMH08** & **SMH09**) favored MAO-A inhibition while 4-nitro group substitution (**SMH10**) drastically decreased activity.
- Replacement of the aryl ring with hetero aryl ring increased MAO-A inhibition by ~8 fold (**SMH11** & **SMH12**).
- Conversion of the imine group from aldimine to ketimine resulted in analogs with enhanced MAO-A inhibitory activity (~20 fold) (**SMH13**).
- Increased bulkiness at the terminal aryl ring of ketimine analogs caused a reduction in MAO-A inhibitory activity than unsubstituted ketimine analogs.

SAR of MAO-B inhibition

- Attempted modification at the N-terminal aryl ring yielded analogs with variable MAO-B inhibitory potential. Analog substituted with 2,6-dichloro group emerged as the lead MAO-B inhibitor among all the tested ligands with an IC_{50} value of 0.064 ± 0.003 µM.
- Introduction of mono chlorine atom at the *ortho* position of terminal aryl ring in aldimines caused 2-fold increased MAO-B inhibition (**SMH02**) while at *para* position enhanced the activity by 27-fold.
- Dichloro substitution at 2,3-position reduced MAO-B inhibition up to 2-fold (**SMH04**) while 2,4-dichloro substituted analog displayed a 3-fold increase in activity (**SMH05**) than mono chloro substituted analog at *para* position (**SMH03**).
- 2-hydroxy substitution increased the activity of the resulting analog by 15-fold (**SMH07**) while 4-hydroxy, 4-methoxy and 4-nitro group diminished MAO-B inhibitory activity of resulting analogs (**SMH08**, **SMH09** and **SMH10**) compared to **SMH07**.
- Replacement of terminal aryl ring with hetero aryl ring resulted in increased MAO-B inhibitory potency of analogs; **SMH11** & **SMH12** by 17 & 12-fold, respectively.
- Conversion of the imine group from aldimine to ketimine resulted in analogs with enhanced MAO-B inhibitory activity (~4 fold) (**SMH13**).
- 4-Fluoro substitution at the aryl ring highly favored MAO-B inhibition (**SMH14**) whereas 4-chloro and 4-nitro substitution has slightly enhanced activity (**SMH15** and **SMH17**), and 4-bromo substitution has drastically decreased the MAO-B activity (**SMH16)**.

3.4.2.1.4. *In vitro* ChE inhibition assay (SMH series)

Compounds **SMH01-SMH17** were screened against acetylcholinesterase and compound **SMH06** was also screened against BChE to evaluate the selectivity of compound **SMH06**.

The obtained results against AChE inhibition studies indicate that IC_{50} values fall in a narrow range near 1-2 μM. Compound **SMH12** emerged as the lead AChE inhibitor compound with IC_{50} value of 1.227 ± 0.001 μM.

SAR of dual MAO and AChE inhibition

- The introduction of different substituent(s) at the N-terminal aryl ring yielded compounds with variable MAO-A, MAO-B and AChE inhibitory potential.
- The introduction of *ortho* chloro group (compound **SMH02**) increased the activity of the resulting analog against both MAO-A and MAO-B but reduced the potency against AChE (compound **SMH02**) compared to unsubstituted analog (compound **SMH01**).
- 4-chloro substitution has slightly reduced the MAO-A inhibition activity while highly favoring MAO-B and AChE inhibitory activity (compound **SMH03**) compared to *ortho* chloro analog (compound **SMH02**).
- Enriching the terminal aryl ring with 2,3-dichloro group (compound **SMH04**) has drastically decreased the MAO-A inhibition activity, and moderately reduced MAO-B and AChE inhibition activity compared to the 4-chloro analog (compound **SMH03**).
- 2,4-dichloro substitution (compound **SMH05**) resulted in an increased MAO-A & MAO-B inhibition activity but did not change potency towards AChE as compared to the 2,3-substituted analog (compound **SMH04**).
- 2,6-dichloro substitution (compound **SMH06**) has decreased the MAO-A and AChE inhibition activity but significantly enhanced MAO-B inhibition activity, yielding the most potent MAO-B inhibitor of the series.

- 2-hydroxy substitution (compound **SMH07**) significantly enhanced the MAO inhibition (compound **SMH07**) but did not affect MAO-B and AChE activity compared to unsubstituted analog (compound **SMH01**).
- Analog with 4-hydroxy substitution decreased MAO-A and MAO-B activity but slightly improved AChE activity (compound **SMH08**) while 4-methoxy analog (compound **SMH09**) enhanced MAO-A, reduced MAO-B but did not cause any change in AChE inhibition compared to the 2-hydroxy analog (compound **SMH07**).
- 4-nitro substitution (compound **SMH10**) has reduced MAO-A inhibition but enhanced MAO-B and AChE inhibition activity compared to the unsubstituted analog (compound **SMH01**).
- Replacement of terminal phenyl ring with heteroaryl ring such as pyridine (compound **SMH11**) or furan (compound **SMH12**) ring has enhanced potency towards all three targets.
- Conversion of the imine group from aldimine to ketimine resulted in analogs with enhanced MAO-A, and MAO-B inhibitory activity but did not affect AChE activity (compound **SMH13**).
- Analogs with 4-fluoro (compound **SMH14)** and 4-chloro (compound **SMH15**) groups enhanced the potency towards MAO-A, and MAO-B but did not influence the AChE activity.
- Substitution with 4-bromo or 4-nitro group has resulted in a decrease in the MAO-A & MAO-B activity but slightly improved the AChE inhibition activity (compounds **SMH16** & **SMH17**).

3.4.2.1.5. Enzyme kinetics and reversibility

The lead inhibitors (compounds **SMA09** and **SMH06**) were subjected to enzyme kinetics and time-dependent reversibility studies against MAO-B and AChE enzymes to draw the

mechanism of action against each target enzyme. A double reciprocal or Lineweaver-Burk plot was constructed to deduce the type of inhibition (competitive or non-competitive or mixed type). The graphs indicate that compound **SMA09** acts through competitive inhibition against MAO-B and AChE (**Figure 3.7A** & **3.7D**) while the kinetics graph of compound **SMH06** shows mixed-type inhibition against both MAO-B and AChE enzymes (**Figure 3.8A** & **3.8D**). Further, the time-dependent reversibility study was conducted to evaluate the binding mode (reversible or irreversible) of the ligand. The resultant plots of time-dependent reversibility indicate that the compound **SMA09** inhibits MAO-B in reversible and AChE in an irreversible manner (**Figure 3.7C** & **3.7F**) while compound **SMH06** was reversible against MAO-B and AChE for at least 60 minutes (**Figure 3.8C & 3.8F**). The obtained experimental Ki values for compounds **SMA09** and **SMH06** (through a Dixon plot) against MAO-B were 40.73, 29.05 µM, for AChE 6.25 and 12.10 µM, respectively.

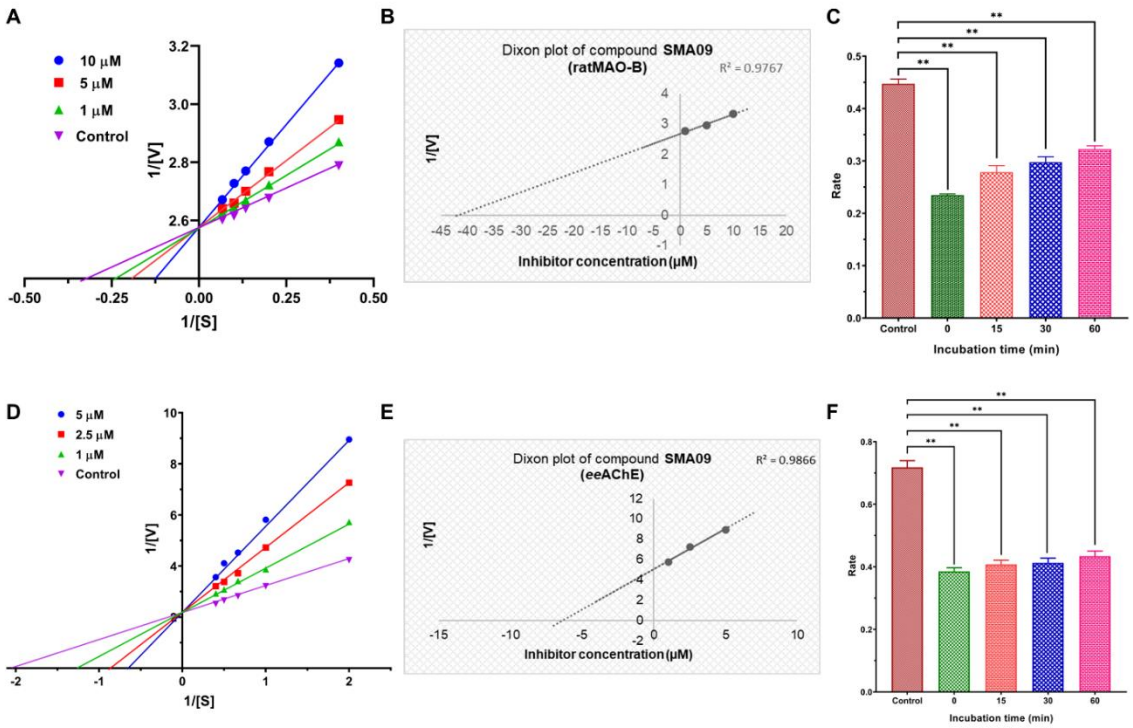

Figure 3.7. Enzyme kinetics, time-dependent reversibility study and Dixon plot of compound **SMA09** with MAO-B and AChE; A) Enzyme kinetics graph of compound **SMA09** with MAO-B; B) Dixon plot of compound **SMA09** with MAO-B; C) Time-

dependent reversibility graph of compound **SMA09** with MAO-B enzyme; D) Enzyme kinetics graph of compound **SMA09** with AChE; E) Dixon plot of compound **SMA09** with AChE; F) Time-dependent reversibility graph of compound **SMA09** with AChE enzyme.

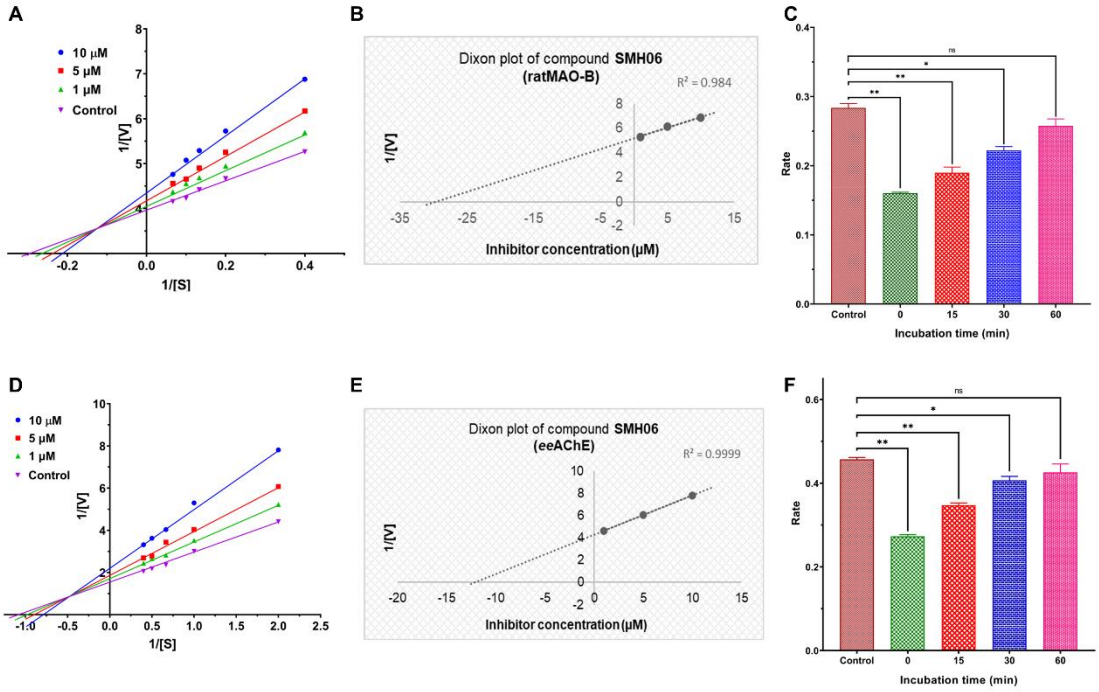

Figure 3.8. Enzyme kinetics, time-dependent reversibility study and Dixon plot of compound **SMH06** with MAO-B and AChE; A) Enzyme kinetics graph of compound **SMH06** with MAO-B; B) Dixon plot of compound **SMH06** with MAO-B; C) Time-dependent reversibility graph of compound **SMH06** with MAO-B enzyme; D) Enzyme kinetics graph of compound **SMH06** with AChE; E) Dixon plot of compound **SMH06** with AChE; F) Time-dependent reversibility graph of compound **SMH06** with AChE enzyme.

3.4.2.1.6. *In vitro* antioxidant assay

The antioxidant potential of selected compounds of **SMA series** (compounds **SMA01, SMA03-SMA06, SMA08**, **SMA09** and **SMA11**) and **SMH series** (compounds **SMH03**, **SMH04**, **SMH05**, **SMH06**, **SMH07**, **SMH11**, **SMH12** and **SMH14**) along with marketed drug molecules donepezil (DPZ), selegiline (SEL), tranylcypromine (PCPA) was evaluated through DPPH assay. Ascorbic acid (AA) was used as a reference antioxidant compound. The percent free radical scavenging activity graph of tested molecules is shown in **Figure 3.9** while the EC_{50} values are listed in **Table 3.6.**

Compound **SMA11** exhibited the highest free radical scavenging activity (~54 %) among all the tested compounds of the **SMA series** while compound **SMA09** displayed 53 %

activity. Most of the tested compounds showed weak to moderate antioxidant activity while marketed drugs displayed poor antioxidant activity (**Table 3.6**).

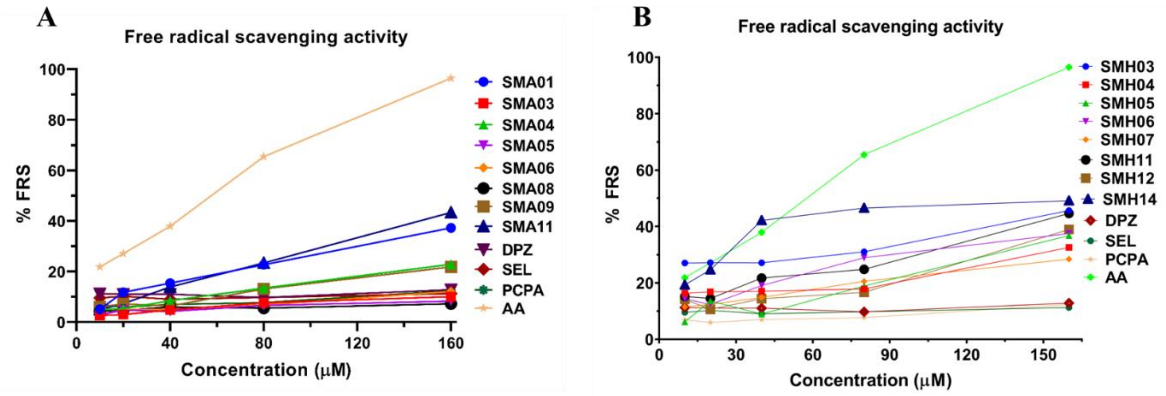

Figure 3.9. Free radical scavenging activity of selected compounds of A) **SMA series** and B) **SMH series**.

Compound **SMH14** exhibited the highest free radical scavenging activity with an FRS value of 61 % among all the tested molecules of the **SMH series** while compound **SMH06** displayed about 47 % of FRS. Most of the test molecules showed weak to moderate activity. The obtained % FRS and EC_{50} of all the tested molecules are listed in **Table 3.6**. The percent FRS graph of **SMH series** compounds is given in **Figure 3.9B.**

Table 3.6. Antioxidant activity (% FRS) of selected compounds

Compound code	Antioxidant activity by DPPH assay	
	% FRS[a]	EC_{50} (μM)
SMA01	45.90 ± 0.987	220.76 ± 6.985
SMA03	11.69 ± 0.918	932.01 ± 8.710
SMA04	22.53 ± 0.588	513.8908963
SMA05	10.28 ± 0.424	1457.853944
SMA06	15.033 ± 0.861	714.4678492
SMA08	7.67 ± 0.263	1798.302912
SMA09	28.77 ± 0.441	435.9718258
SMA11	53.80 ± 0.162	185.09 ± 0.822
SMH03	50.04 ± 0.946	199.71 ± 7.436
SMH04	36.29 ± 1.483	309.97 ± 8.722
SMH05	45.82 ± 2.464	215.06 ± 9.687
SMH06	46.95 ± 1.211	217.83 ± 7.424
SMH07	35.59 ± 2.177	287.112 ± 3.242
SMH11	53.09 ± 1.637	184.62 ± 8.049

SMH12	45.48 ± 2.259	208.11 ± 9.807
SMH14	61.60 ± 0.321	135.17 ± 2.428
Donepezil	11.70 ± 0.810	2174.10 ± 79.56
Selegiline	11.26 ± 0.150	1613.30 ± 46.04
Tranylcypromine	12.68 ± 0.736	1324.80 ± 40.54
Ascorbic acid[b]	66.89 ± 2.070	62.14 ± 0.36

[a] % FRS at a concentration of 200 μM; [b] % FRS at a concentration of 100 μM.

3.4.2.1.7. *In vitro* metal chelation assay

The impaired homeostasis of metal ions in the brain of aged patients leads to increased misfolding of proteins (β-amyloid) and production of hydroxyl radical (ROS) by catalyzing the Fenton reaction. The removal of excess iron by chelation will reduce load due to oxidative stress. The metal chelation property of the molecule depends on its electron-donating capacity and the position of the functional group it contains. Selected molecules of **SMA series** (compounds **SMA05**, **SMA08**, and **SMA09**) and **SMH series** (compounds **SMH06** and **SMH14**) were subjected to a metal chelation study using a UV-Vis spectrophotometer. The UV spectrum of the compound alone, ferric chloride and the mixture of compound and ferric chloride shows the shift of peak due to the chelation of iron from λ 360 nm to other respective positions (**Figure 3.10**). The UV spectrum of the mixture of compounds and $FeCl_3$ clearly shows the absence of a peak at λ 360 nm due to ferric chloride which indicates that the test compounds have the ability to chelate the free iron present in the solution.

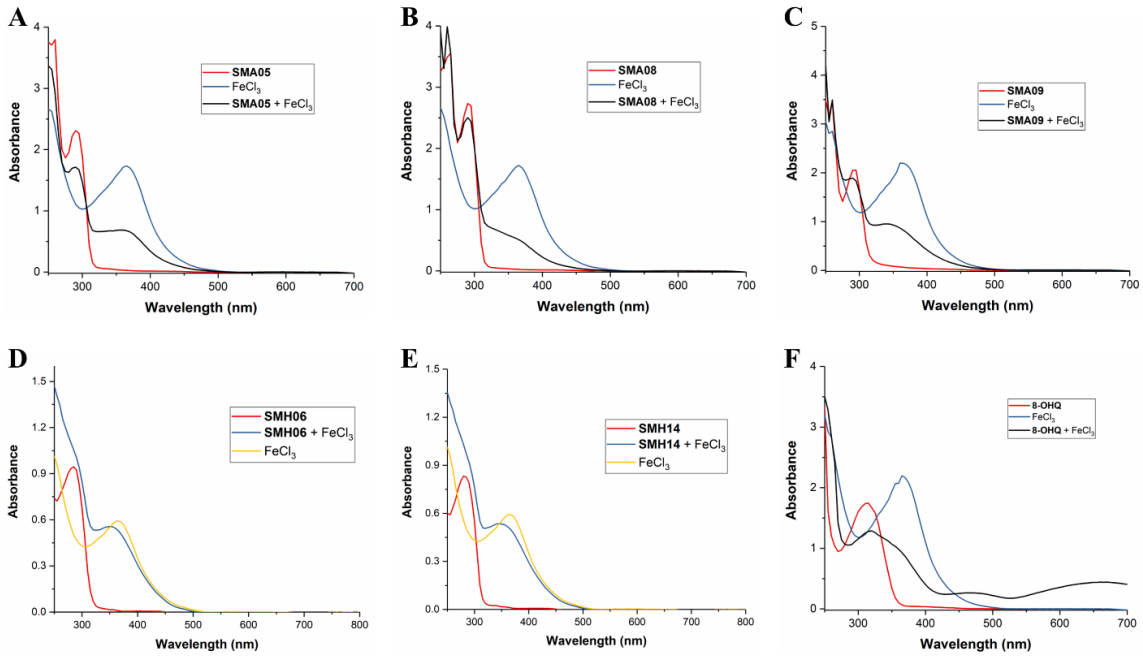

Figure 3.10. UV absorption spectra of compounds **SMA05**, **SMA08**, **SMA09**, **SMH06** and **SMH14** alone and with $FeCl_3$; A) Compound **SMA05**; B) Compound **SMA08**; C) Compound **SMA09** and D**)** Compound **SMH06**; E) Compound **SMH14**; and F) 8-**OHQ** (8-Hydroxyquinoline) as reference iron chelator.

3.4.2.1.8. *In vitro* blood-brain-barrier permeation assay

Each newly designed chemical entity targeting the brain is required to reach at site of action. The validation of brain accessibility of new molecules is done through *in vitro* passive permeation-based PAMPA-BBB assay. Compounds **SMA09** and **SMH06** were evaluated for their *in vitro* blood-brain barrier permeability using selegiline and donepezil as reference drugs while imipramine and tenoxicam were used as permeability controls, respectively. Compounds **SMA09** and **SMH06** exhibited an effective permeability (P_e) of 7.147 ±0.133 $\times 10^{-6}$ cm/s and 8.305 ± 0.020$\times 10^{-6}$ cm/s after 18 h of incubation, respectively. The effective permeability values of test and reference compounds are presented in **Table 3.7**. As reported by Di et al., the molecule with $P_e > 4.0 \times 10^{-6}$ cm/s is considered CNS+ while the molecule with $P_e < 2.0 \times 10^{-6}$ cm/s is considered CNS-. Whereas a molecule with $Pe < 4.0 \times 10^{-6}$ cm/s and $Pe > 2.0 \times 10^{-6}$ cm/s is considered CNS±. However, compound

SMA09 has a P_e value of greater than 4 which falls under the CNS+ class and indicates that the molecules **SMA09** and **SMH06** have the potential to passively cross BBB.

Table 3.7. PAMPA-BBB assay result of compound **SMA09** and **SMH06**

Compound ID	P_e ($\times 10^{-6}$ cm/s)[a]	Reference P_e ($\times 10^{-6}$ cm/s)[b]	*In Silico* Predicted BBB permeability[c]	CNS Category[d]	Literature CNS category[b]
SMA09	7.147 ±0.133	NA	0.247	CNS+	NA
SMH06	8.305 ± 0.020	NA	0.274	CNS+	NA
Donepezil	7.504 ± 0.305	6.80	0.188	CNS+	CNS+
Selegiline	6.417 ± 0.205	5.69	4.435	CNS+	CNS+
Imipramine[e]	14.922 ± 0.131	13	2.920	CNS+	CNS+
Tenoxicam[e]	1.267 ± 0.168	0.1	0.095	CNS-	CNS-

[a] P_e values as mean ± SD of two independent experiments in duplicate.
[b] Values are cited from Di *et.al.*, 2003.
[c] BBB permeability using PreADMET web-based server (accessed on 08.08.2024).
[d] CNS+ ($P_e > 4.0 \times 10^{-6}$ cm/s), CNS± ($P_e > 2.0 \times 10^{-6}$ cm/s $< 4.0 \times 10^{-6}$ cm/s), CNS- ($P_e < 2.0 \times 10^{-6}$ cm/s)
[e] Used as positive and negative permeability controls respectively.

3.4.2.1.9. Cell-based neurotoxicity assay

The cytotoxicity study of compounds **SMA09** and **SMH06** was performed with fibroblast cells (L929) and neuroblastoma cell line (SH-SY5Y) using an MTT assay. Different concentrations (0.1, 1, 10, 50 and 100 µM) of the compounds **SMA09** and **SMH06** were used to treat the cells for 24 h followed by an MTT assay. The obtained results indicate that compound **SMA09** was non-toxic to the fibroblast and neuroblastoma cells up to 50 µM concentration while compound **SMH06** was found non-toxic to fibroblast cells up to 50 µM, for neuroblastoma cells up to 10 µM. The percent cell viability versus concentration of test compounds **SMA09** and **SMH06** graphs for fibroblast and neuroblastoma cells are given in **Figures 3.13A**, **3.13B, 3.13C,** and **3.13D,** respectively. The inverted microscopic brightfield image, and fluorescence image of fibroblast cells 24 h post-treatment with compound **SMA09** at 0 µM (Control) and 50 µM concentration are shown in **Figures 3.11A** & **3.11B** while the inverted microscopic brightfield image of neuroblastoma cells 24 h post-

treatment with **SMA09** at 0 µM (Control) and 50 µM concentration are shown in the **Figures 3.11C** & **3.11D**.

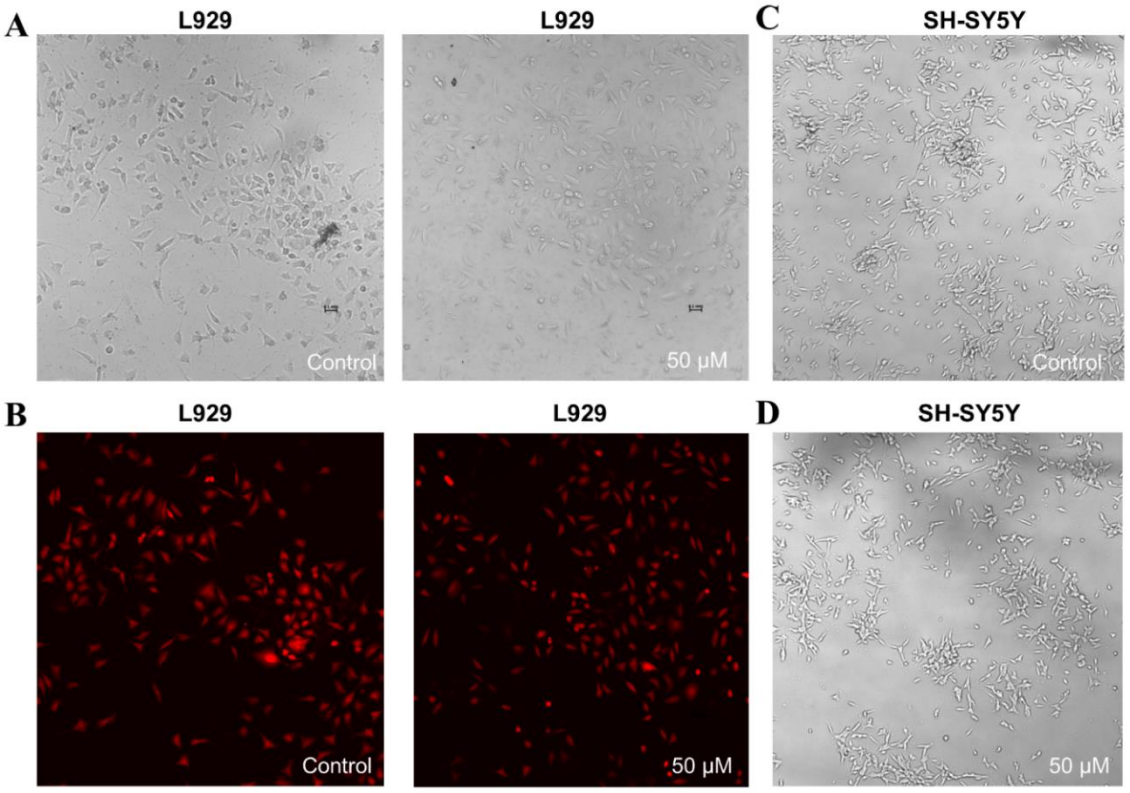

Figure 3.11. *In vitro* toxicity assay of compound **SMA09** in fibroblast (L929) and neuroblastoma (SH-SY5Y) cells; A) inverted microscopic brightfield image of L929 cell 24 h post-treatment with compound **SMA09** at 0 µM (Control) and 50 µM concentration; B) inverted microscopic fluorescence image of L929 cell 24 h post-treatment with compound **SMA09** at 0 µM (Control) and 50 µM concentration; C) microscopic brightfield image of SH-SY5Y cell 24 h post-treatment with compound **SMA09** at 0 µM (Control) and D) 50 µM concentration.

The inverted microscopic brightfield image, and fluorescence image of fibroblast cells 24 h post-treatment with compound **SMH06** at 0 µM (Control) and 50 µM concentration are shown in **Figures 3.12A** & **3.12B** while the inverted microscopic brightfield image of neuroblastoma cells 24 h post-treatment with **SMH06** at 0 µM (Control) and 50 µM concentration are shown in the **Figure 3.12C** & **3.12D**.

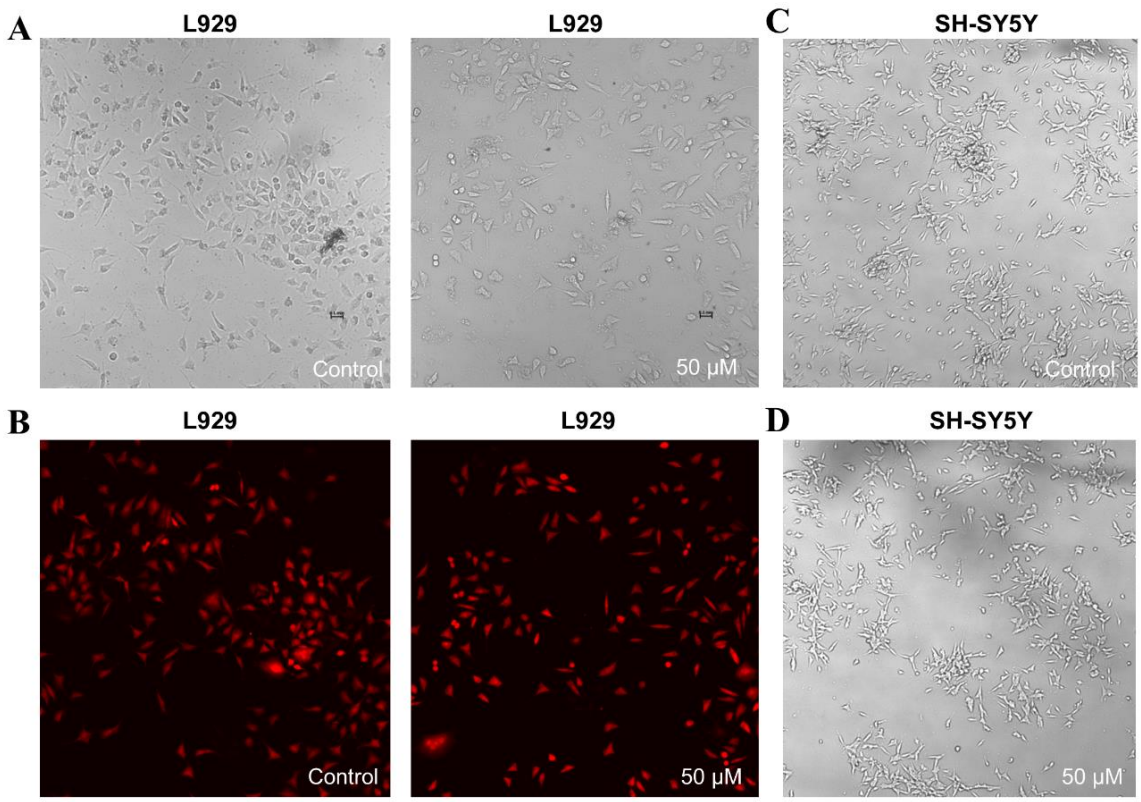

Figure 3.12. *In vitro* neurotoxicity assay of compound **SMH06** in fibroblast (L929) and neuroblastoma (SH-SY5Y) cells; A) inverted microscopic brightfield image of L929 cell 24 h post-treatment with compound **SMH06** at 0 µM (Control) and 50 µM concentration; B) inverted microscopic fluorescence image of L929 cell 24 h post-treatment with compound **SMH06** at 0 µM (Control) and 50 µM concentration; C) microscopic brightfield image of SH-SY5Y cell 24 h post-treatment with compound **SMH06** at 0 µM (Control) and D) 50 µM concentration.

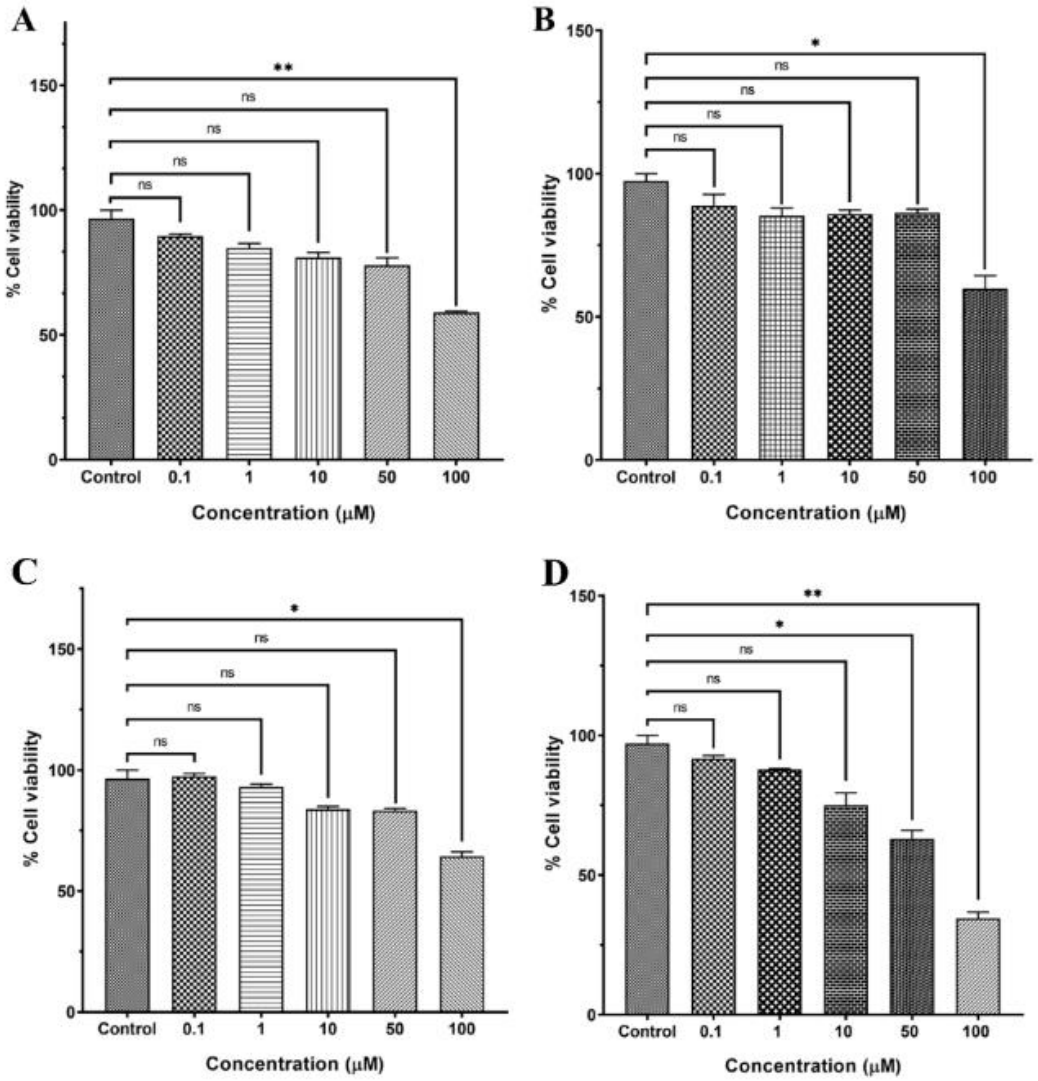

Figure 3.13. Cell viability graphs of compounds **SMA09** and **SMH06** against fibroblast (L929) A & B); and neuroblastoma cell line (SH-SY5Y) C & D).

3.4.2.1.10. Neuroprotection assay using neuroblastoma cell line

Post *in vitro* cytotoxicity and neurotoxicity assessment, compound **SMA09** was evaluated for its neuroprotective potential against dexamethasone-induced oxidative stress in neuroblastoma cell lines (SH-SY5Y). Dexamethasone (a cellular stressor) is a fluorinated glucocorticoid that acts through the glucocorticoid receptor (nuclear receptor) in the cell and causes an increase of MAO-B activity in the cells, as well as apoptosis. Cells were loaded into a 96-well cell culture plate and treated with three different concentrations of test compound **SMA09** (0.25, 100 and 200 nM) prepared in DMEM media containing 2 μM of dexamethasone for 72 h except for control wells (containing only cell culture medium). The cell survival plot

indicates that cells treated with compound **SMA09** displayed significant dose-dependent recovery as compared to dexamethasone-treated cells. From the graph, it can be inferred that compound **SMA09** exhibits a neuroprotective effect against dexamethasone-induced oxidative stress and elevated MAO-B levels in SH-SY5Y cells (**Figure 3.14**)

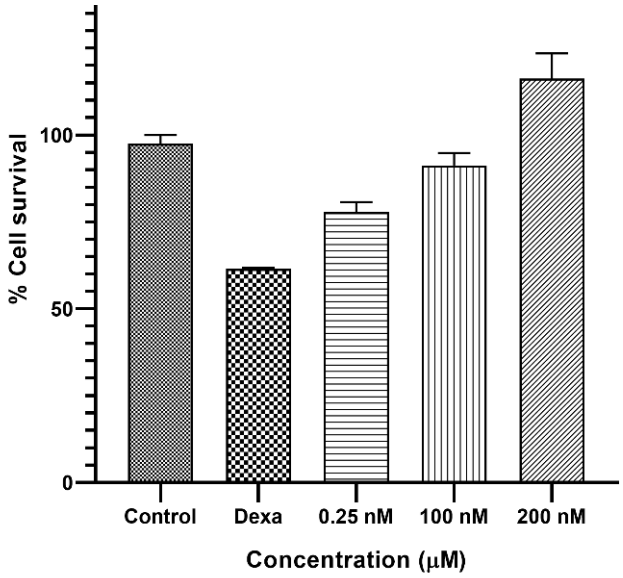

Figure 3.14. *In vitro* neuroprotection assay of compound **SMA09** in SH-SY5Y cells against dexamethasone-induced oxidative stress, % cell survival vs. different concentrations (0.25, 100 and 200 nM) of compound **SMA09** with 2 μM concentration of dexamethasone.

3.4.2.2. *In vivo* studies

3.4.2.2.1. Scopolamine induced amnesia model

Further compounds **SMA09** and **SMH06** were evaluated for their *in vivo* efficacy against the ameliorative potential of cognitive and memory dysfunction in a scopolamine-induced cognition deficit model. The activity of spontaneous alteration behavior of compound **SMA09** (5, 10 and 20 mg/kg BW) along with donepezil (5 mg/kg BW) was determined (**Figure 3.15A & 3.15B**).

3.4.2.2.2. Y-maze test

An initial study was conducted with 5 mg/kg BW of compounds **SMA09** and **SMH06** for *in vivo* neuroprotective efficacy. Scopolamine-induced amnesia model was used as a disease model while animal behavior and memory deficit were measured through the Y-

maze test. Significant improvement was observed in the animals treated with compounds **SMA09** and **SMH06** as compared to the scopolamine-treated group. Further, the dose dose-dependent effect of compound **SMA09** was evaluated with 5, 10 and 20 mg/kg BW along with donepezil (5 mg/kg), and percentage spontaneous alteration was recorded and a graph was plotted. The results were analyzed using one-way ANOVA and revealed significant differences among the groups. The scopolamine (SCO) treated group displayed a significantly decreased percentage of alteration ($p < 0.05$) as compared to the control group, indicating scopolamine-induced cognitive impairment. The animal treated with 5, 10 and 20 mg/kg BW of compound **SMA09** showed a significant increase in the percentage alteration as compared to the scopolamine (SCO) treated group indicating the reversal of scopolamine-induced memory deficit (**Figure 3.15B**). The above findings disclosed that administration of compound **SMA09** at different doses (5, 10 and 20 mg/kg) and compound **SMH06** at 5 mg/kg BW produced significant improvement in the memory deficit induced with scopolamine.

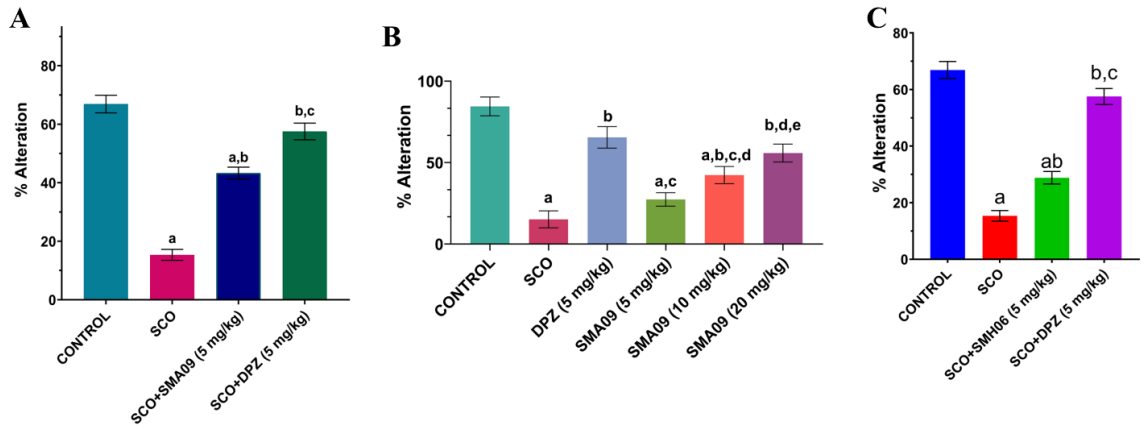

Figure 3.15. Effect of compound **SMA09** and **SMH06** on scopolamine-induced cognition and memory impairment showing effect on spontaneous alteration A) % $^{a}P < 0.05$ vs. control; $^{b}P < 0.05$ vs. scopolamine; $^{c}P < 0.05$ vs. compound **SMA09** (5 mg/kg), $^{d}P < 0.05$ vs. **DPZ** (5 mg/kg); B) Effect of different doses of compound **SMA09** on scopolamine-induced cognition and memory impairment showing effect on spontaneous alteration % $^{a}P < 0.05$ vs. control; $^{b}P < 0.05$ vs. scopolamine; $^{c}P < 0.05$ vs. compound **DPZ** (5 mg/kg), $^{d}P < 0.05$ vs. compound **SMA09** (5 mg/kg), $^{e}P < 0.05$ vs. compound **SMA09** (10 mg/kg), $^{f}P <$

0.05 vs. compound **SMA09** (20 mg/kg); C) % [a]P < 0.05 vs. control; [b]P < 0.05 vs. scopolamine; [c]P < 0.05 vs. compound **SMH06** (5 mg/kg), [d]P < 0.05 vs. **DPZ** (5 mg/kg).

3.4.2.2.3. *Ex vivo* biochemical analysis

The impact of compound **SMA09** on neurochemical levels was determined through the estimation of biochemical parameters like enzyme (AChE), neurotransmitter (ACh), cell stressor (MDA) and cell protector (CAT). The hippocampal tissue homogenate was used for the determination of biochemicals. The results indicate a decreased level of ACh with enhanced activity of AChE in the animal group treated with scopolamine (SCO) as compared to the control group ($p < 0.05$). However, the animal group treated with compound **SMA09** displayed a significant increase in the level of ACh while reducing the level of AChE compared to scopolamine treated group ($p < 0.05$) (**Figure 3.16A** & **3.16B**). Further, the antioxidant activity of compound **SMA09** was accessed by evaluating the level of oxidative biochemical markers malondialdehyde (MDA) and catalase (CAT). The graphs demonstrated that the scopolamine-treated group significantly decreased CAT level with increased MDA level as compared to the control group ($p < 0.05$) (**Figure 3.16C** & **3.16D**). The animal group treated with compound **SMA09** attenuated MDA and significantly enhanced CAT level as compared to the scopolamine-treated group. Overall, the obtained *ex vivo* biochemical results suggest the AChE inhibitory potential of compound **SMA09** along with antioxidant activity.

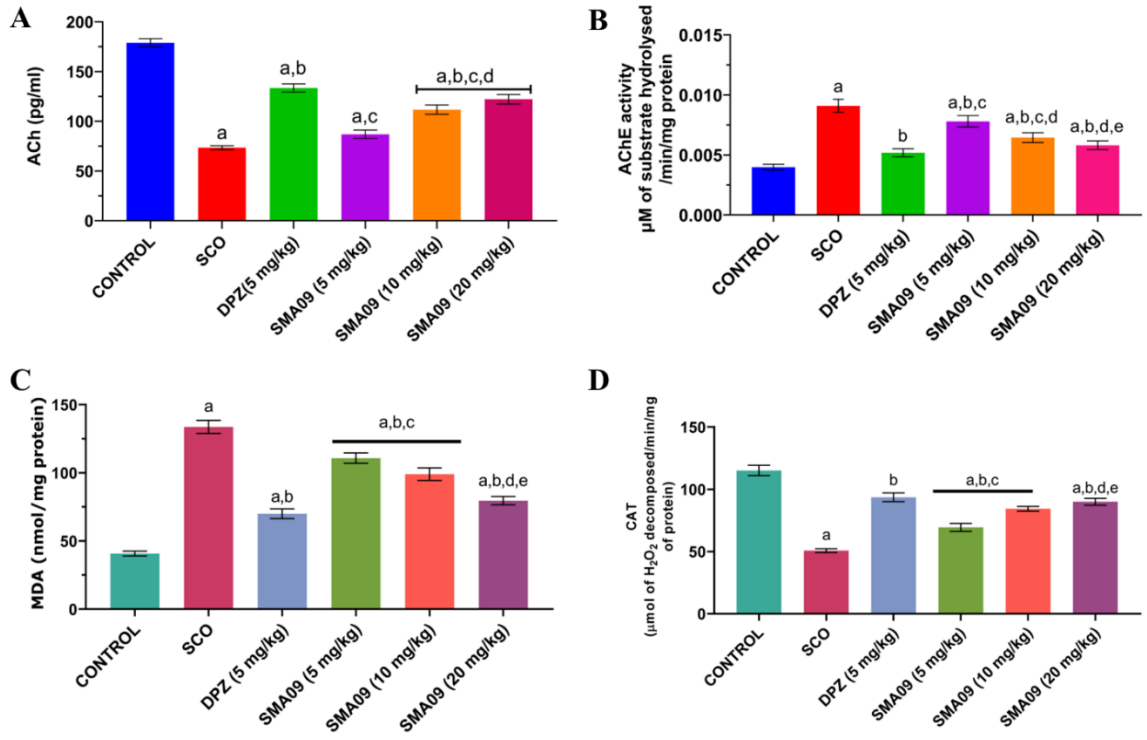

Figure 3.16. Scopolamine-induced memory deficit in mice; (A) Effect of compound **SMA09** on the level of ACh; (B) Impact of compound **SMA09** on the activity of AChE; (C) Role of compound **SMA09** on MDA level and; (D) CAT activity. $^{a}P < 0.05$ vs. control; $^{b}P < 0.05$ vs. scopolamine; $^{c}P < 0.05$ vs. compound **SMA09** (5, 10 and 20 mg/kg).

3.4.2.2.4. *In vivo* acute oral toxicity of compound SMA09

As per OECD guideline 423 (Acute Toxic Class Method) [154], the acute oral toxicity assessment was carried out on adult female albino mice to determine the *in vivo* safety and median lethal dose or LD_{50}. No animal was found dead or in a moribund state within 14 days of administration of the compound at a dose of 300 mg/kg and 2000 mg/kg BW, suggesting that compound **SMA09** was safe for all the animals at given doses.

At the end of the study, the effect of a single dose of compound **SMA09** 300 mg/kg and 2000 mg/kg BW on the organ coefficient of highly perfused organs including the brain, heart, kidney and liver were examined. The organ weight of animals is a crucial parameter in *in vivo* toxicological investigations; variation in the weight of organs especially highly perfused ones may undergo morphological change due to systemic toxicity. The accurate method for calculating any change in the organ is organ weight in relation to its body weight

during toxicological studies. Following animal sacrifice, the effect of a single oral dose of compound **SMA09** (300 mg/kg and 2000 mg/kg BW) on the organ coefficients of the crucial organs—the brain, heart, kidneys, and liver is shown in **Figure 3.17**. From the graph, it is clear that compound **SMA09** does not significantly alter the organ coefficient of these highly perfused organs in any of the groups. The organ coefficients of the brain, heart, kidneys, and liver did not significantly change among the groups, according to statistical analysis using the one-way ANOVA. We also performed a histopathology analysis as per OECD 423 criteria to look for any tissue damage our test substance might have caused to the aforementioned organs.

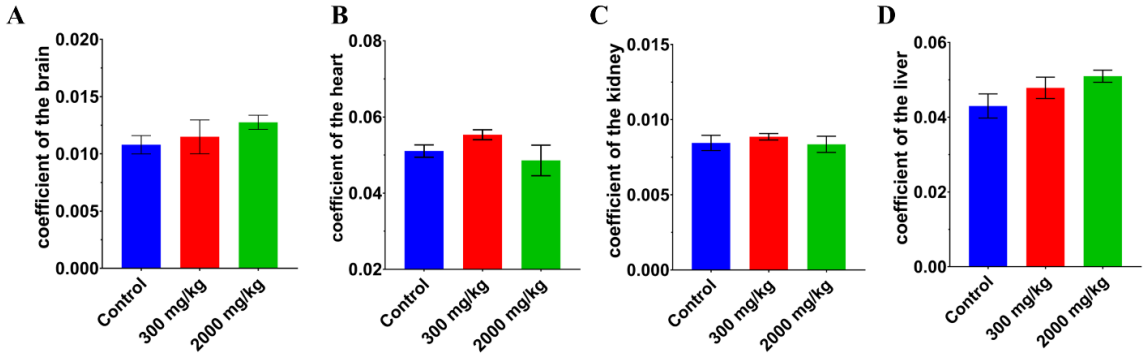

Figure 3.17. Effect of single-dose oral administration of **SMA09** (300 mg/kg BW and 2000 mg/kg BW) on organ coefficient of the brain (A), heart (B), liver (C), and kidneys, (D) at the end of the experiment.

At the end of the study, a single oral administration of a dose of 300 mg/kg and 2000 mg/kg BW of compound **SMA09** did not cause any damage to the tissue architecture of the brain, heart, kidneys, and liver, none of these highly perfused organs showed any histopathological changes, as can be seen from the microphotographs in **Figure 3.18**. Normal brain cortex neurons, normal hepatocytes with acidophilic cytoplasm, intact vesicular nucleus radiating from the central vein surrounding the portal tract, and proper sinusoids in the liver sections were all present. The heart sections also showed normal myocardial muscle bundles with thin fibro collagenous stroma and the normal renal tubules in the kidney sections in all the study groups were observed.

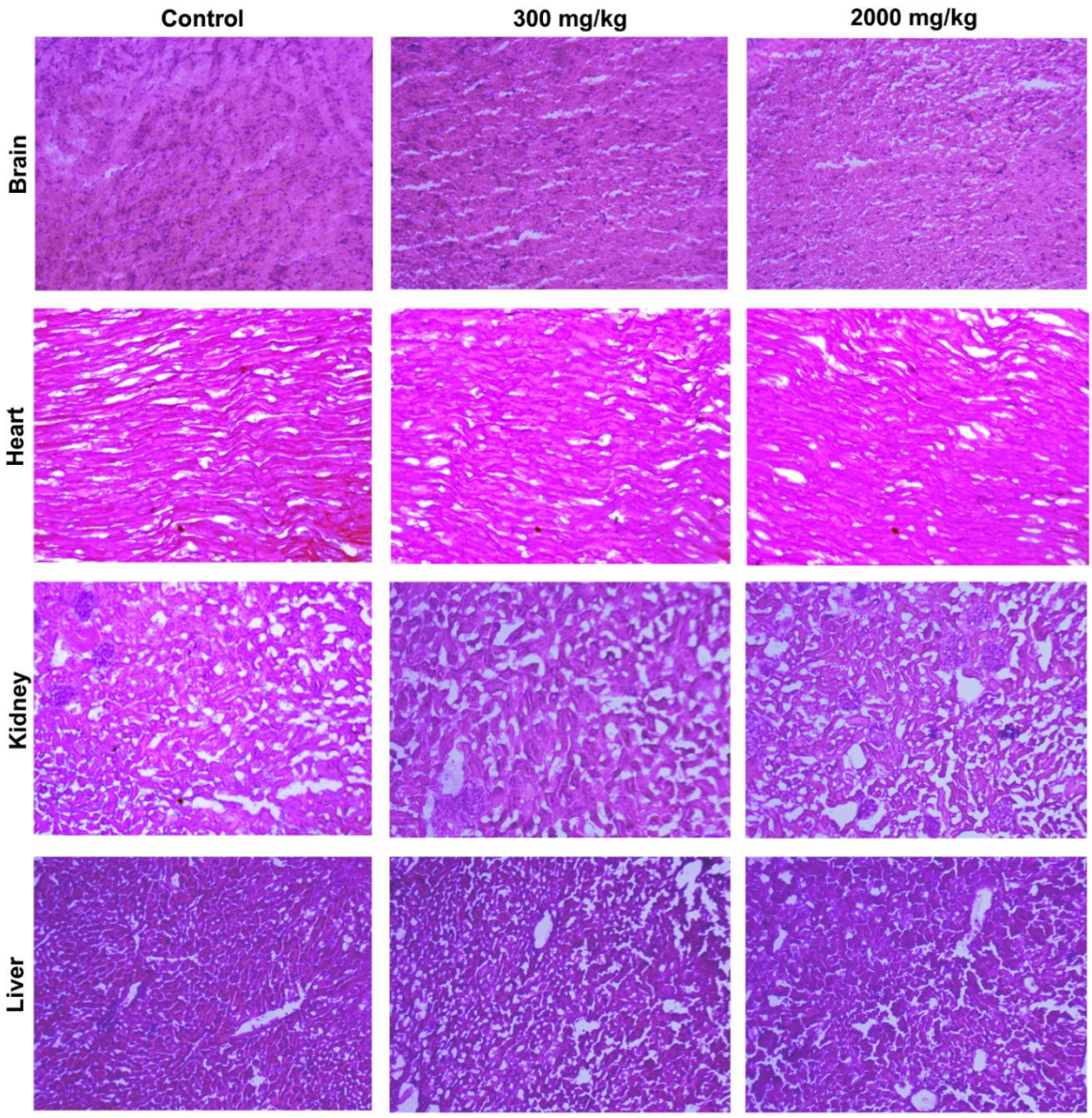

Figure 3.18. Effect of single-dose oral administration of compound **SMA09** (at a dose of 300 and 2000 mg/kg BW) along with vehicle control on the brain of adult female albino mice and other highly perfused organs viz. heart, kidney and liver tissue stained with hematoxylin and eosin (H & E) dye at the end of 14 days. Microphotographs of each organ were taken at 10X resolution.

3.4.3. Computational studies

3.4.3.1. Molecular docking

To understand the binding of sesamol-derived O-acetamides and extended carbohydrazones within the active sites of MAO-A MAO-B, AChE and BChE, docking runs were performed using co-crystallized human MAO-A, MAO-B, AChE and BChE through structure-based

molecular modeling approach. The crystal structures of targets of interest were obtained from the Protein Data Bank (PDB). Suitable crystal structures of AChE (PDB ID: 4EY7), MAO-A (PDB ID: 2Z5X) and MAO-B (PDB ID: 2V5Z) were selected and utilized in the molecular docking study using AutoDock 4.2 [155, 156, 188, 189]. Further, binding mode and ligand-protein interaction analysis were performed on the resulting conformers possessing the best docking score. The calculated molecular docking parameters; inhibition constant (K_i) and binding free energy (ΔG) are presented in **Table 3.8** and **Table 3.9.**

3.4.3.1.1. Molecular docking studies against MAO-A

The visual inspection of virtual enzyme binding studies of compounds **SMA01-SMA11** and **SMH01-SMH17** against MAO-A reveals that all the ligands are well accommodated within the active site and bind to the same cavity as the co-crystallized ligand. The benzodioxole moiety of most of the ligands was oriented towards the isoalloxazine ring of FAD (**Figure 3.19A**).

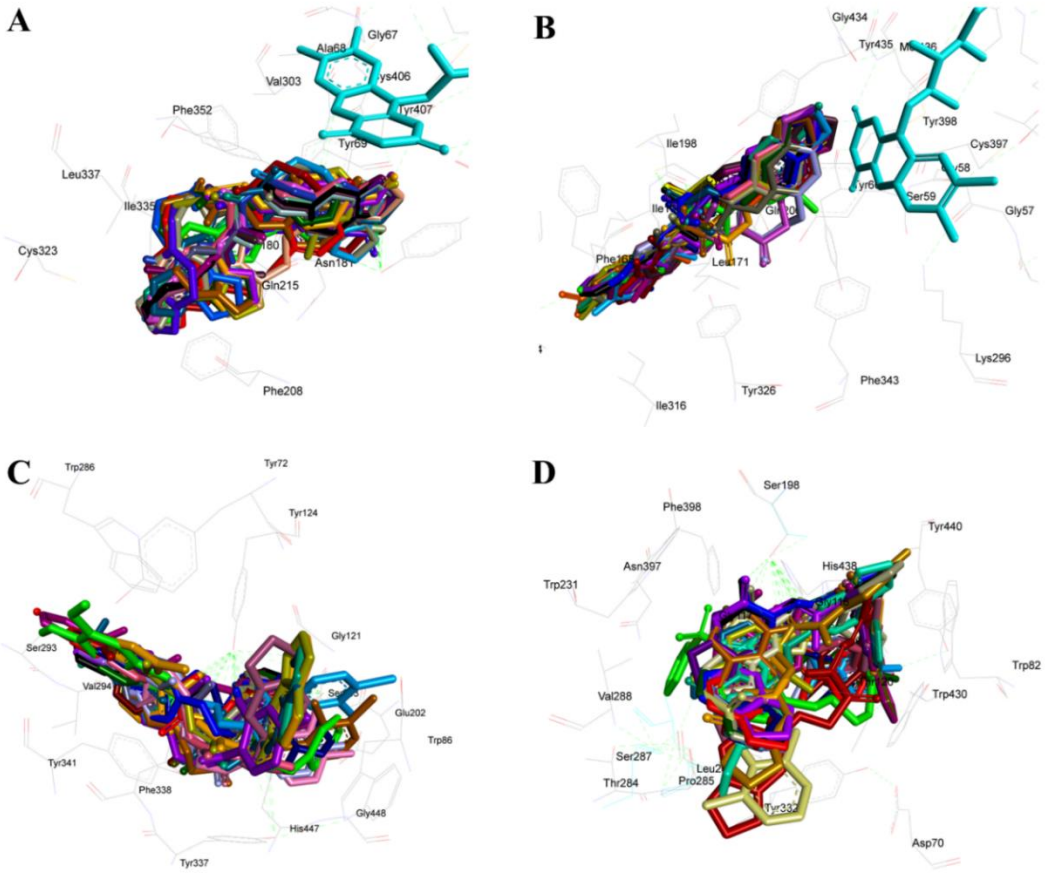

Figure 3.19. Superimposed docked solutions of compounds **SMA01-SMA11** and **SMH01-SMH17** in the active site gorge of A) MAO-A (PDB ID: 2Z5X) active site; B) MAO-B (PDB ID: 2V5Z) active site; C) AChE (PDB ID: 4EY7) active site and D) BChE (PDB ID: 7AWG) active site.

3.4.3.1.2. Binding mode of compounds SMA09 and SMH06 with MAO-A

The visual inspection of the docked MAO-A-compound **SMA09** complex reveals that compound **SMA09** occupies the same cavity as harmine (reference inhibitor) and lies throughout the active site. The benzodioxole moiety is oriented toward the isoalloxazine ring of FAD while the terminal aryl ring is pointed towards the entrance site (**Figure 3.20A**). The 2D interaction map shows that compound **SMA09** is well stabilized by hydrophobic (pi-alkyl, pi-pi stacked, pi-pi T-shaped, pi-sigma and pi-sulfur) interactions. Methylene of benzodioxole moiety interacts with FAD, Tyr407, Gly443 and Tyr444 through pi-alkyl and carbon-hydrogen bonding interactions whereas phenyl ring interacts

with FAD, Tyr407 and Tyr444 through pi-pi stacking and carbon-hydrogen bonding interaction, respectively. The N-terminal aryl ring interacts with Phe208, Gln215, Cys323 and Ile335 through pi-pi stacking, pi-alkyl, pi-sulfur and pi-donor hydrogen bonding interactions. The chloro group at the *p*-position of the terminal aryl ring interacts with Phe208, Cys323 and Ile325 through pi-alkyl interaction. Further, residues Tyr69, Asn181, Ile207, Leu337, Met350 and Phe352 interact with compound **SMA09** through van der Waals interactions (**Figure 3.20C**).

The visual examination of the 3D orientation image of MAO-A and compound **SMH06** complex revealed that the position of the ligand was tightly closed to the co-crystallized inhibitor harmine. The position of compound **SMH06** indicates proper accommodation within the active site. Benzodioxole moiety of the ligand was oriented towards the isoalloxazine ring of FAD while the terminal aryl ring was pointed towards the entrance of the active site (**Figure 3.20A**). 2D interaction map of compound **SMH06** displayed hydrogen bonding and hydrophobic interactions (pi-alkyl, pi-pi-stacking, pi-sigma and pi-sulfur). Tyr197 interacts with the oxygen of the dioxole ring through hydrogen bonding whereas Asn181 interacts with the methylene group of the dioxole ring by forming a carbon-hydrogen bond. The methylene group of the dioxole ring also interacts with Ile207, Tyr407 and Tyr444 through a pi-alkyl bond. The benzene ring of benzodioxole moiety interacts with Tyr407 and Tyr444 through pi-pi stacking interaction. Terminal aryl ring of ligand interacts with Ile180, Phe208, Cys323 and Ile335 through pi-alkyl, pi-pi stacking, pi-sulfur and pi-sigma interactions, respectively (**Figure 3.20E**).

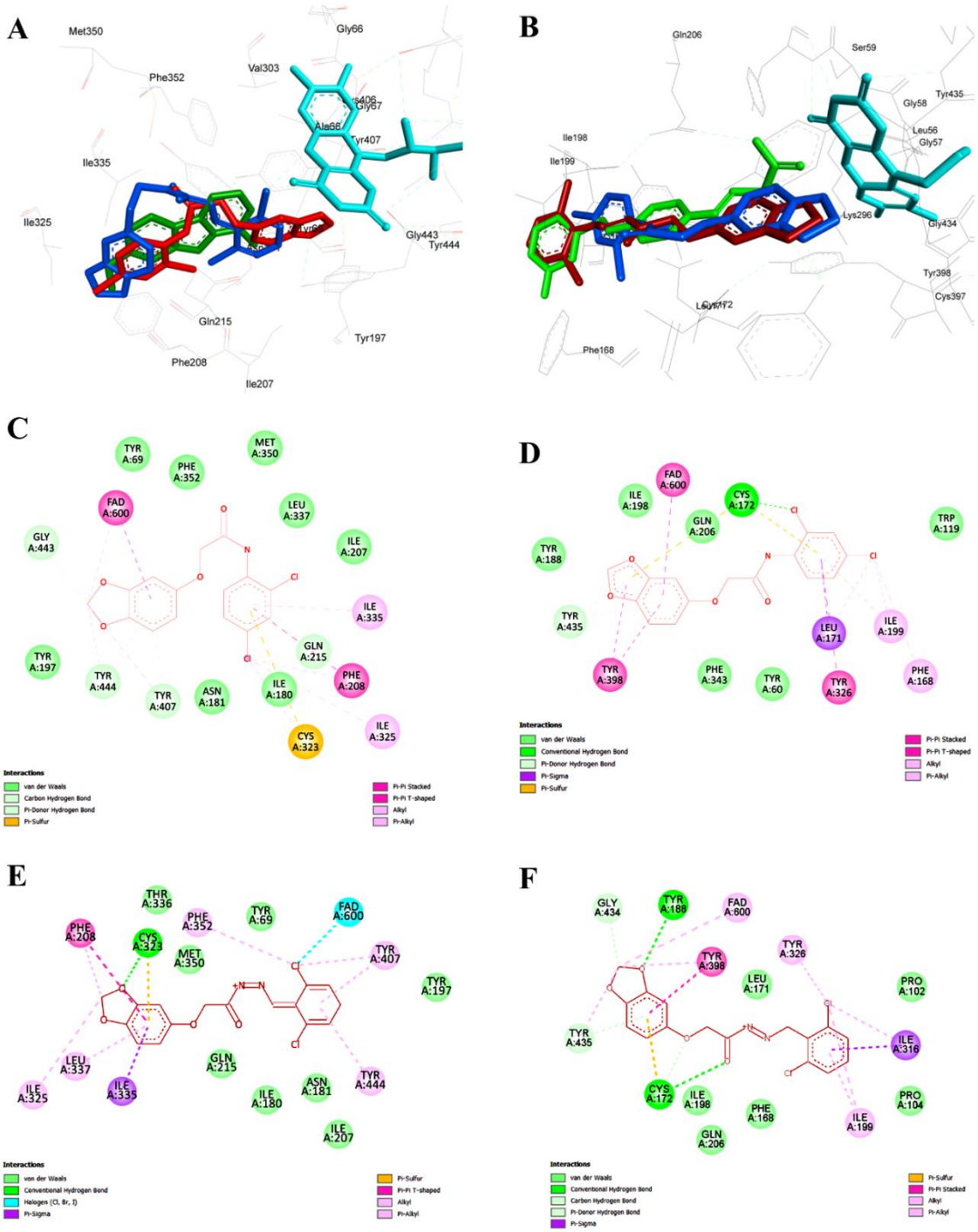

Figure 3.20. Binding mode and 2D interaction map of compound **SMA09** and **SMH06** in the active site of MAO-A, MAO-B; A) 3D orientation of compound **SMA09** (red) and **SMH06** (blue) in MAO-A active along with harmine (green); B) 3D orientation map of compound **SMA09** (red) and **SMH06** (blue) in the active site gorge of MAO-B with reference compound safinamide (green); C) 2D interaction map of compound **SMA09** with MAO-A; D) 2D interaction of compound **SMA09** with MAO-B; E) 2D interaction of compound **SMH06** with MAO-A; F) 2D interaction of compound **SMH06** with MAO-B.

3.4.3.1.3. Molecular docking studies against MAO-B

The visual examination of superimposed docking images of all ligands **SMA01-SMA11** and **SMH01-SMH17** indicates the position and orientation of ligands within the active site. In general, the bulky hydrophobic benzodioxole moiety of each ligand orients toward the isoalloxazine ring of FAD while variable aryl moiety is pointed toward the opening of the entrance cavity (**Figure 3.19B**).

3.4.3.1.4. Binding mode of compounds SMA09 and SMH06 with MAO-B

Visual analysis of the docked solution of compound **SMA09**-MAO-B complex indicates that the molecule occupies both entrance and substrate cavities similar to the reference inhibitor safinamide. The benzodioxole ring of the ligand orients towards the isoalloxazine ring of FAD, while the N-terminal aryl ring orients towards the opening of the entrance cavity (**Figure 3.20B**). The 2D interaction diagram shows that compound **SMA09** is well stabilized by H-bond, and hydrophobic (pi-alkyl, pi-pi stacked, pi-pi T-shaped, pi-sigma and pi-sulfur) interactions. The dioxole ring of benzodioxole moiety interacts with Cys172, Tyr398 and Tyr435 through pi-sulfur, pi-pi stacking and van der Waals (pi-donor hydrogen bonding) interactions, respectively, whereas, the aryl ring of benzodioxole moiety interacts with FAD, Tyr398 and Tyr435 through pi-pi T-shaped, pi-pi stacking and pi-donor hydrogen bonding interactions, respectively. The 2-chloro group of the N-terminal aryl ring interacts with Cys172 through hydrogen bonding interaction while the 4-chloro group interacts with Phe168, Leu171, and Ile199 through pi-alkyl interaction. Further, the N-terminal aryl ring interacts with Leu171, Cys172, Ile199 and Tyr326 through pi-sigma, pi-sulfur, pi-alkyl and pi-pi stacking interactions (**Figure 3.20D**).

Visualization of molecular docking results and 3D alignment image of MAO-B and compound **SMH06** complex displayed that ligand was well accommodated and occupied the same region of the active site as co-crystallized inhibitor safinamide. Benzodioxole

moiety of ligand was pointed towards FAD while the aryl ring was oriented towards the opening of the entrance cavity of the active site (**Figure 3.20B**). The 2D interaction map of compound **SMH06** shows different types of interaction including hydrogen bonding and hydrophobic (pi-alkyl, pi-pi stacking, pi-sigma, pi-sulfur and van der Waals interaction). The methylene group of the dioxole ring interacts with FAD, Tyr398 and Tyr435 through pi-alkyl interaction while with Gly434 through a carbon-hydrogen bond. The benzene ring of benzodioxole moiety formed a pi-donor hydrogen bond with Tyr435, pi-pi stacking with Tyr398 and pi-sulfur with Cys172. Tyr188 formed a hydrogen bond with the oxygen atom of the dioxole ring. Cys172 also interacts with the oxygen atom of linker carbonyl through a hydrogen bond while with ether oxygen through the carbon-hydrogen bond. One of the chloro group at the terminal aryl ring interacts with Ile199, Ile316 and Tyr326 through pi-alkyl interaction. Ile199 and Ile316 also interact with terminal aryl through pi-alkyl and pi-sigma interaction, respectively. Furthermore, residues Pro102, Pro104, Phe168, Leu171, Ile198 and Gln206 interact through van der Waals forces (**Figure 3.20F**).

3.4.3.1.5. Molecular docking studies against AChE

The molecular docking of each compound of the **SMA** and **SMH series** (**SMA01-SMA11** and **SMH01-SMH17**) was performed against AChE (PDB ID: 4EY7) by using AutoDock 4.2. The superimposed poses of test and reference ligands are provided in **Figure 3.19C**. Visual inspection of superimposed conformers reveals that all the ligands are well accommodated in the active site gorge of AChE.

3.4.3.1.6. Binding mode of compounds SMA09 and SMH06 with AChE

The visual examination of the docked solution of the AChE-compound **SMA09** complex reveals that the molecule **SMA09** shares a similar orientation pattern as that of donepezil and traverses through all the crucial regions of the active site. The benzodioxole moiety of the ligand points toward the peripheral anionic site (PAS) of the cavity while the terminal

aryl ring orients toward the catalytic triad are located near the bottom of the active site (**Figure 3.21A**). The 2D interaction diagram shows that compound **SMA09** is well stabilized by H-bond, hydrophobic (pi-alkyl, pi-pi stacked, pi-pi T-shaped and pi-sulfur) interactions. The methylene group of benzodioxole moiety interacts with Trp286 and Val296 through pi-alkyl interaction while the phenyl ring interacts with Tyr341 through pi-pi stacking. Terminal aryl ring interacts with Tyr337 and His447 through pi-pi T-shaped stacking, and pi-sulfur interaction, respectively. The chloro group at the 4th position of the terminal aryl ring interacts with Trp86 and Glu202 through pi-alkyl and alkyl-hydrogen interaction (**Figure 3.21C**)

Analysis of molecular docking results of compound **SMH06** and AChE docked complex disclosed that compound **SMH06** occupied the same cavity of the active site as a co-crystallized inhibitor and accommodated well. The bulky benzodioxole moiety of the ligand was found to be oriented toward the opening of the active site near the PAS region while the terminal aryl ring was pointed towards the bottom of the gorge closure to the catalytic triad (**Figure 3.21A**). 2D interaction map of the compound **SMH06** showed different types of molecular interactions including hydrogen bond and hydrophobic interaction (pi-alkyl, pi-pi stacking, pi-pi T shaped, pi-cation and carbon-hydrogen bond) which stabilize the ligand within the active site. The terminal aryl ring of the ligand interacts with Trp86 and His447 through pi-pi T-shaped interaction. The chloro group at the terminal aryl ring interacts with His447 through pi-alkyl interaction. The benzene ring of benzodioxole moiety interacts with Trp286 through pi-pi stacking interaction. The methylene group of the dioxole ring interacts with Trp286, Leu289, and Arg296 through pi-alkyl interaction while with Ser293 by forming a carbon-hydrogen bond. Additionally, residues Gly121, Gly122, Tyr124, Glu202, Ser203, Ala204, Val294, Phe297, Tyr337, Phe338, Tyr341 and Tyr448 interact through van der Waals forces (**Figure 3.21E**).

.

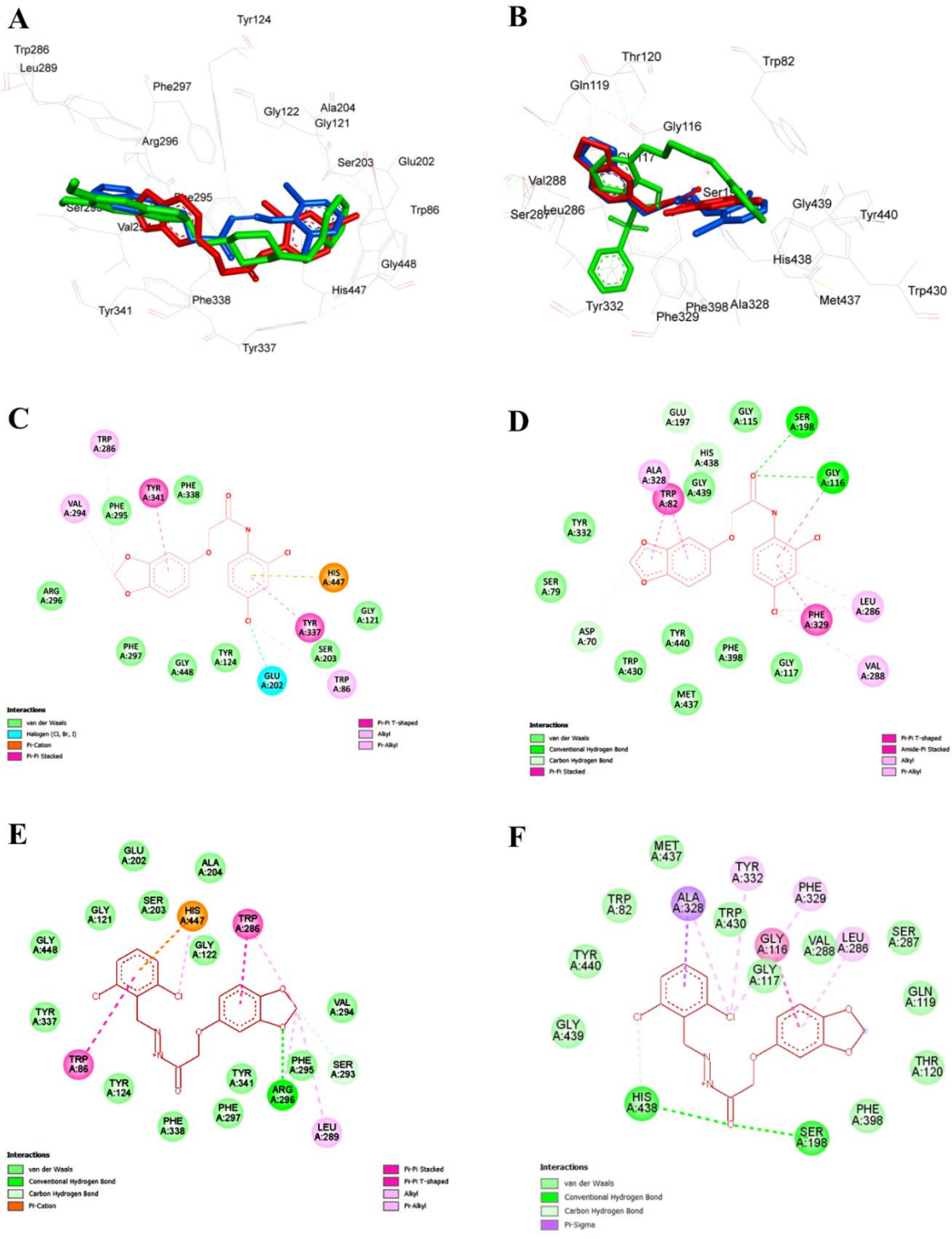

Figure 3.21. Binding mode and 2D interaction map of compound **SMA09** and **SMH06** in the active site of AChE and BChE; A) 3D orientation map of compound **SMA09** (red) and **SMH06** (blue) in AChE active along with donepezil (green); B) 3D orientation map of compound **SMA09** (red) and **SMH06** (blue) in the active site gorge of BChE with reference compound S6Q (green); C) 2D interaction map of compound **SMA09** with AChE; D) 2D

interaction map of compound **SMA09** with BChE; E) 2D interaction map of compound **SMH06** with AChE; F) 2D interaction map of compound **SMH06** with BChE;

3.4.3.1.7. Molecular docking studies against BChE

The molecular docking studies of the synthesized ligands (compounds **SMA01-SMA11** and **SMH01-SMH17**) were performed against BChE (PDB ID: 7AWG) to understand the binding pattern and orientation of the ligand in the active site of the enzyme. The superimposed conformations of ligands are shown in **Figure 3.19D** and indicate that the ligands are well accommodated within the active site. The obtained molecular docking results are listed in **Table 3.8** and **Table 3.9.**

3.4.3.1.8. Binding mode of compounds SMA09 and SMH06 with BChE

The visualization of the docked solution of compound **SMA09-**BChE complex reveals that the compound **SMA09** is well accommodated within the active of BChE and occupies the same cavity as the reference ligand. The benzodioxole moiety of the ligand points towards the opening of the active site while the terminal aryl ring orients towards the bottom of the active site gorge (**Figure 3.21B**). Analysis of the 2D interaction map unveils that the compound **SMA09** is stabilized by H-bond, hydrophobic (pi-alkyl, pi-pi stacked, pi-pi T-shaped, and pi-sulfur) interactions. The methylene group of the dioxole ring interacts with Asp70 through carbon-hydrogen bonding interaction and the benzodioxole moiety interacts with Trp82 and Ala328 through pi-pi and pi-alkyl stacking interactions. Further, the ether oxygen and methylene spacer of the linker interacts with Glu197 and His438 through carbon-hydrogen bonding interaction while the amide carbonyl oxygen of the linker interacts with Gly116 and Ser198 through hydrogen bonding. On the other hand, the N-terminal aryl ring of ligand molecule interacts with Gly116, Ilu286, and Phe329 through hydrogen bonding, pi-alkyl, and pi-pi-stacking interactions, respectively. The chloro group

at the terminal aryl ring interacts with Leu286 and Val288 through pi-alkyl interaction (**Figure 3.21D**).

Visual inspection of the 3D alignment image of compound **SMH06** and BChE docked complex showed that compound **SMH06** was well accommodated within the active site of BChE. The bulky hydrophobic benzodioxole moiety was pointed toward the indole moiety of the co-crystallized ligand while the terminal aryl ring was found to lie near the benzyl ring of S6Q (co-crystallized ligand) (**Figure 3.21B**). The 2D interaction diagram of compound **SMH06** displayed several types of molecular interactions including hydrogen bonding and hydrophobic interactions (pi-alkyl, amide-pi stacking, carbon-hydrogen bond and van der Waals interaction). The oxygen atom of the carbonyl group interacts through hydrogen bonding with Ser198 and His438. One chloro group at the terminal aryl ring interacts with His438 through a carbon-hydrogen bond while another chloro group interacts with Ala328, Phe329 and Tyr332 through pi-alkyl interaction. Terminal aryl ring interacts with Ala328 through pi-sigma interaction while the benzene ring of benzodioxole moiety interacts with Gly116 and Leu286 through amide-pi stacking and pi-alkyl interaction, respectively. Furthermore, van der Waals interaction were observed with Trp82, Gly117, Gln119, Thr120, Ser287, Val288, Phe398, Trp430, Met437, Gly439 and Tyr440 residues (**Figure 3.21F**).

Table 3.8 Results of *in silico* docking studies of compounds **SMA01-SMA11**

Compd. code	MAO-A		MAO-B		AChE		BChE	
	ΔG **(kcal/mol)**	***Ki*** **(μM)**	***ΔG*** **(kcal/mol)**	***Ki*** **(μM)**	***ΔG*** **(kcal/mol)**	***Ki*** **(μM)**	***ΔG*** **(kcal/mol)**	***Ki*** **(μM)**
SMA01	-7.77	2.01	-8.35	0.76	-7.88	1.69	-7.80	1.92
SMA02	-7.53	3.02	-8.39	0.71	-7.32	4.34	-7.14	5.79
SMA03	-8.31	0.82	-9.04	0.24	-7.98	1.41	-7.78	1.97
SMA04	-8.44	0.65	-9.42	0.12	-8.31	0.81	-8.16	1.04
SMA05	-7.95	1.49	-8.66	0.45	-7.77	2.02	-7.49	3.24
SMA06	-7.67	2.38	-8.44	0.65	-8.16	1.04	-7.23	5.02
SMA07	-7.37	3.97	-8.03	1.31	-7.43	3.58	-7.04	6.97

SMA08	-8.73	0.40	-9.69	0.08	-8.40	0.70	-8.39	0.71
SMA09	-8.80	0.36	-9.47	0.11	-8.41	0.68	-7.92	1.57
SMA10	-8.43	0.67	-9.33	0.15	-8.07	1.21	-7.93	1.53
SMA11	-8.44	0.65	-8.97	0.26	-8.00	1.37	-8.07	1.21
Std.[a]	-7.34	4.16	-8.95	0.28	-10.50	0.02	-10.11	0.04

[a] Docking score of co-crystallized ligand (MAO-A, PDB ID: 2Z5X, Harmine; MAO-B, PDB ID: 2V5Z, Safinamide; AChE, PDB ID: 4EY7, Donepezil; BChE, PDB ID: 7AWG, S6Q).

Table 3.9. Results of *in silico* docking studies of compounds **SMH01-SMH17**

Mol. ID	MAO-A (2Z5X)		MAO-B (2V5Z)		AChE (4EY7)		BChE (7AWG)	
	ΔG (kcal/mol	K_i (μM)	ΔG (kcal/mol	K_i (μM)	ΔG (kcal/mol	K_i (μM)	ΔG (kcal/mol	K_i (μM)
SMH01	-8.63	0.469	-9.80	0.066	-8.24	0.912	-8.70	0.422
SMH02	-8.57	0.524	-10.56	0.018	-8.51	0.575	-6.00	39.860
SMH03	-8.73	0.397	-10.35	0.026	-8.43	0.662	-8.35	0.756
SMH04	-8.42	0.669	-10.55	0.018	-8.86	0.322	-9.11	0.208
SMH05	-8.48	0.604	-10.77	0.012	-8.98	0.260	-8.60	0.497
SMH06	-8.19	0.989	-10.70	0.014	-8.86	0.318	-9.36	0.137
SMH07	-8.28	0.850	-9.83	0.063	-8.25	0.898	-8.37	0.734
SMH08	-7.93	1.540	-9.59	0.093	-8.25	0.899	-8.57	0.520
SMH09	-8.58	0.517	-9.70	0.077	-8.31	0.811	-8.11	1.140
SMH10	-8.47	0.623	-9.70	0.077	-8.36	0.746	-7.71	2.230
SMH11	-9.14	0.199	-10.35	0.026	-8.56	0.533	-9.22	0.174
SMH12	-8.36	0.750	-10.47	0.021	-8.43	0.658	-8.63	0.468
SMH13	-8.49	0.603	-10.74	0.013	-8.78	0.369	-8.64	0.463
SMH14	-8.37	0.729	-10.81	0.012	-9.19	0.184	-8.50	0.585
SMH15	-7.49	3.220	-10.50	0.020	-9.25	0.163	-7.98	1.410
SMH16	-8.17	1.030	-9.31	0.150	-8.08	1.200	-8.14	1.070
SMH17	-7.57	2.810	-8.80	0.355	-7.93	1.540	-8.67	0.441
Std[a]	-7.34	4.160	-8.95	0.280	-10.50	0.020	-10.11	0.040

[a] Docking score of the co-crystallized ligand with the respective target protein (MAO-A, PDB ID: 2Z5X, Harmine; MAO-B, PDB ID: 2V5Z, Safinamide; AChE, PDB ID: 4EY7, Donepezil; BChE, PDB ID: 7AWG, S6Q).

3.4.3.2. Molecular dynamics simulation

To evaluate the reliability and robustness of the molecular docking studies we have performed molecular dynamic (MD) simulation studies of lead molecules **SMA09** and **SMH06** with MAO-B (PDB ID: 2V5Z) and AChE (PDB ID: 4EY7) enzymes. The Desmond module (Version 12.7.156, Schrodinger Release 2021.1: Desmond Molecular Dynamics System, D. E. Shaw Research, New York, NY, 2021) was utilized for 100 ns of MD simulation. The preparation of all the input files, visual analysis, and processing of

simulation results was done using the Maestro graphical user interface (Maestro, Schrodinger, LLC, New York, NY, 2021).

The stability of the docked protein-ligand complexes was evaluated by the root mean square deviation (RMSD) and root mean square fluctuation (RMSF) of the protein and ligand complex. Furthermore, the secondary structure elements (SSE) of the protein like α-helices and β-strands, the torsional profile of the ligand, and properties like the radius of gyration (rGyr), intramolecular hydrogen bonding (intraHB), polar surface area (PSA), solvent accessible surface area (SASA) were additionally analyzed for complexes any significant conformational change in the protein structure.

3.4.3.2.1. MD simulation of compound SMA09-MAO-B complex

The visual examination of the simulated protein-ligand complex revealed the formation of several types of interactions between active site residues of protein and ligand molecules. These interactions include hydrogen bonding, hydrophobic interaction as well as water bridges. Compound **SMA09** is well accommodated within the active site of MAO-B by making six hydrogen bonds with Leu171, Cys172, Ser200, Thr201, Gln206, Tyr326 and Tyr435 and various hydrophobic interactions with Leu88, His90, Phe99, Pro102, Pro104, Trp119, Leu167, Phe168, Leu171, Ile199, Ile316, Tyr326, Phe343, Leu345, Tyr398 and Tyr435. The molecule is also stabilized by several water bridges with residues His90, Gly101, Pro102, Leu171, Cys172, Ile198, Ile199, Ser200, Thr201, Gly205, Gln206, Tyr326, Tyr398 and Tyr435 (**Figure 3.22B**). A good degree of contact between protein and ligand is observed during the simulation period with residues Phe168, Leu171, Ile199, Tyr326 and Tyr435 (**Figure 3.22C**). The RMSD of both protein and ligand is found within the acceptable range (1-3 Å). The RMSD graph indicates that there is no conformation change in the protein structure during simulation (**Figure 3.22D**).

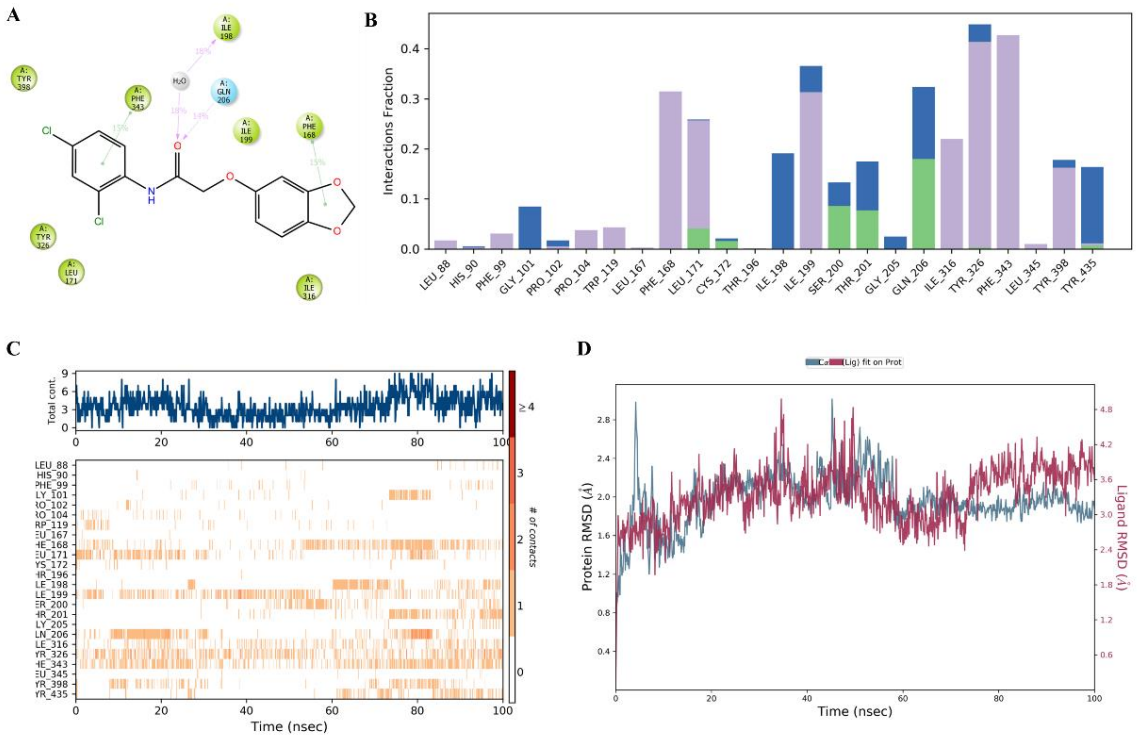

Figure 3.22. Protein-ligand contact diagrams generated through MD simulation of compound **SMA09** with MAO-B (PDB ID: 2V5Z); A) 2D interaction diagram showing percent interaction with residues around ligand: hydrogen bonding (purple arrow), hydrophobic interaction (green arrow); B) Stacked bar chart represents different types of protein-ligand contacts: hydrogen bonding (green), hydrophobic interaction (violet), water bridge (blue); C) Protein-ligand contacts timeline diagram of 100 ns MD simulation; D) RMSD graph of protein (blue) and ligand (maroon).

3.4.3.2.2. MD simulation of compound SMH06-MAO-B complex

Analysis and visual examination of results obtained from MD simulation of MAO-B-compound **SMH06** complex indicate stability of compound **SMH06** within the active site of MAO-B through different types of molecular interactions. Protein-ligand contact diagram shows that compound **SMH06** interacts with Pro102, Pro104, Trp119 and Ile199 through hydrophobic interaction while Ile199 and Tyr326 interact through hydrogen bonding for 69 % and through pi-pi stacking for 35 % of simulation time, respectively (**Figure 3.23A**). Compound **SMH06** interacts with Cys172, Tyr188, Ile199, Ser200, Thr201, Gln20, Tyr326 and Tyr398 through hydrogen bonding while with residues Tyr60, Pro102, Phe103, Pro104, Leu164, Leu167, Phe168, Leu171, Ile199, Ile316, Tyr326,

Leu328, Phe343, Leu345, Tyr398 and Tyr435 through hydrophobic interaction. The ligand also formed water bridges with residues Tyr60, Pro102, Leu171, Ile199, Ser200, Thr201, Gln206, Tyr326, Tyr398 and Tyr435 (**Figure 3.23B**). A good degree of contact was observed with residues Trp119, Ile199 and Tyr326 during the simulation period (**Figure 3.23C**). Furthermore, the RMSD graph of compound **SMH06** and MAO-B shows the stability of the protein-ligand complex without any significant conformational change (**Figure 3.23D**).

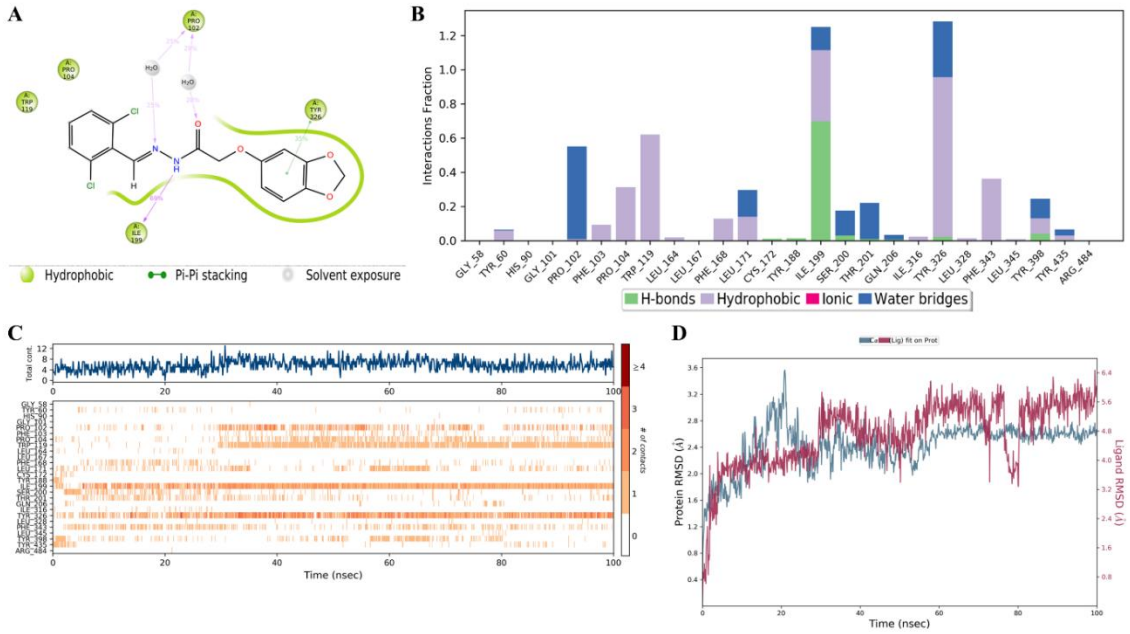

Figure 3.23. Protein-ligand contact diagrams generated through MD simulation of compound **SMH06** with MAO-B (PDB ID: 2V5Z); A) 2D interaction diagram showing percent interaction with residues around ligand: hydrogen bonding (purple arrow), hydrophobic interaction (green arrow), solvent-exposed area (grey); B) Stacked bar chart represents different types of protein-ligand contacts: hydrogen bonding (green), hydrophobic interaction (violet), water bridge (blue); C) Protein-ligand contacts timeline diagram of 100 ns MD simulation; D) RMSD graph of protein (blue) and ligand (maroon).

3.4.3.2.3. MD simulation of compound SMA09-AChE complex

The results obtained from the MD simulation of compound **SMA09**-AChE complex were analyzed to understand the interactions between protein-ligand and assess the stability of the complex throughout the simulation period (100 ns). The crucial interactions observed between the ligand and AChE are hydrogen bonding, hydrophobic interaction and water

bridges. Compound **SMA09** is well lodged within the AChE active site through one hydrogen bond formed by Tyr124, eleven hydrophobic interactions with Leu76, Trp86, Tyr124, His284, Trp286, Val294, Phe295, Phe297, Tyr337, Phe338 and Tyr341 along with several water bridges formed with Tyr72, Val73, Asp74, Thr75, Tyr124, His284, Trp286, Glu292, Phe296, Ser298, Tyr337, Phe338, Tyr341 and Gly342 (**Figure 3.24B**). An appreciable protein-ligand interaction has been observed with Trp86, Tyr124, Trp286, Phe295, Tyr337, Phe338 and Tyr341 during the simulation period (**Figure 3.24C**). The RMSD graph shows that both protein and ligand were stable during the simulation period and indicates no conformational change in the protein structure (**Figure 3.24D**).

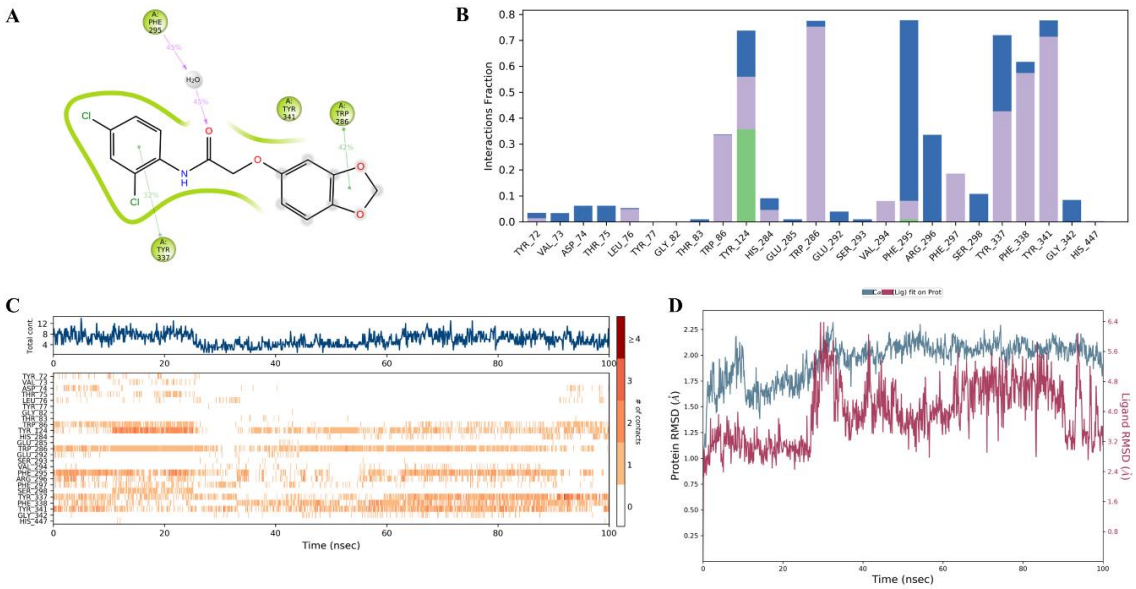

Figure 3.24. Protein-ligand contact diagrams generated through MD simulation of compound **SMA09** with AChE (PDB ID: 4EY7); A) 2D interaction diagram showing percent interaction with residues around ligand: hydrogen bonding (purple arrow), hydrophobic interaction (green arrow), solvent-exposed area (grey); B) Stacked bar chart represents different types of protein-ligand contacts: hydrogen bonding (green), hydrophobic interaction (violet), water bridge (blue); C) Protein-ligand contacts timeline diagram of 100 ns MD simulation; D) RMSD graph of protein (blue) and ligand (maroon).

3.4.3.2.4. MD simulation of compound SMH06-AChE complex

Analysis and examination of results obtained from MD simulation of compound **SMH06** and AChE indicate that it was well accommodated within the active site of AChE.

Compound **SMH06** was stabilized through hydrogen bonding and hydrophobic interactions, bulky benzodioxole moiety showed pi-pi stacking with Tyr337 for 31 % while terminal aryl ring formed pi-pi stacking with Phe80 and Trp286 for 59 % and 42 % of the total simulation period (**Figure 3.25A**). Compound **SMH06** formed hydrogen bond with Glu81, Gly82, Gly121, Gly122, Tyr124, Ser293 and Tyr337 residues while with residues Val73, Leu76, Tyr77, Phee80, Met85, Trp86, Tyr124, Trp286, His287, Leu289, Phe297, Tyr337, Phe338 and His447 hydrophobic interaction was observed. Residues Tyr72, Thr75, Tyr77, Glu81, Gly82, Gly121, Gly122, Tyr124, Glu202, Ser203, Ala204, Gln291, Glu292, Ser293, Phe295, Arg296, Tyr337, Phe338, Tyr341, Gly342 and His447 formed water bridges with compound **SMH06** (**Figure 3.25B**). A good degree of contact was observed between protein and ligand with residues Phe80, Glu81, Trp86, Tyr124, Trp286, Phe296, Arh296, Tyr337, Phe338, and Tyr341 (**Figure 3.25C**). The RMSD graph compound **SMH06** with AChE indicates that both protein and ligand were stabilized near 30 ns simulation and remained stable for the rest of the simulation period (**Figure 3.25D**).

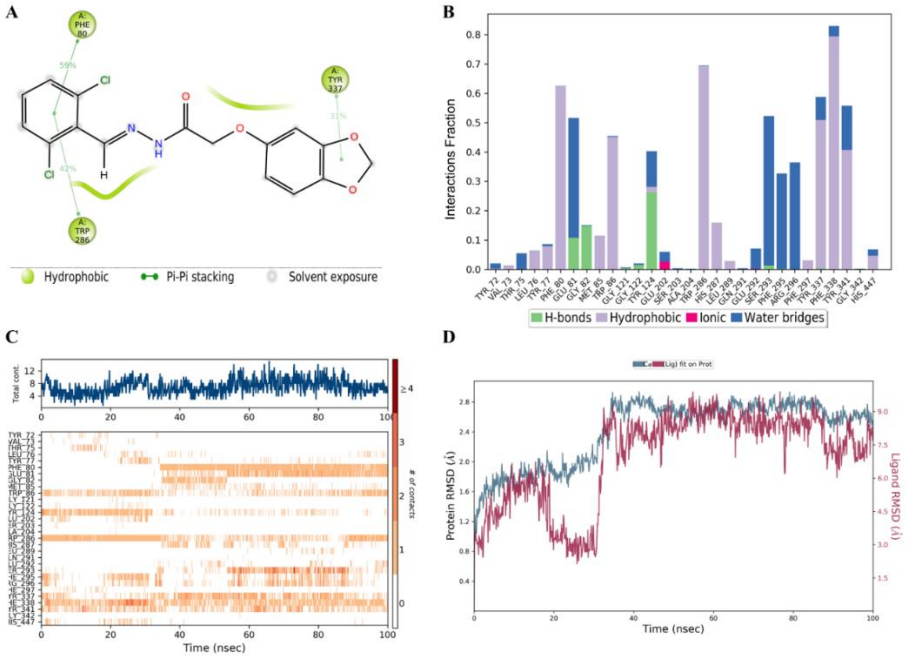

Figure 3.25. Protein-ligand contact diagrams generated through MD simulation of compound **SMH06** with AChE (PDB ID: 4EY7); A) 2D interaction diagram showing percent interaction with residues around ligand: hydrogen bonding (purple arrow),

hydrophobic interaction (green arrow), solvent-exposed area (grey); B) Stacked bar chart represents different types of protein-ligand contacts: hydrogen bonding (green), hydrophobic interaction (violet), water bridge (blue); C) Protein-ligand contacts timeline diagram of 100 ns MD simulation; D) RMSD graph of protein (blue) and ligand (maroon).

3.4.3.3. Ligand binding efficiency

Ligand efficiency is the ratio of free energy of binding over the number of heavy atoms in a ligand. The impact of the size and number of heavy atoms in the ligand over the potency of the molecule is considered as an important metric in drug discovery. As the number of heavy atoms increases, the potency of the ligand is compromised after a certain limit due to an increase in the polar surface area of the ligand. The ligand with either very less or more heavy atom counts is generally not suitable due to the huge difference in the accessible surface area of the receptor site. All the compounds of **SMA series** (**SMA01-SMA11)** and **SMH series (SMH01-SMH17)** were subjected to the calculation of ligand binding efficiency using the MedChem calculator web server (http://www.vulpinescience.co.uk/). The obtained ligand efficiency data indicate that most of the compounds lie near 0.4 ligand efficiency similar to reference inhibitors which in turn suggests that the number of heavy atoms in the designed ligands is in the acceptable range (**Figure 3.26**).

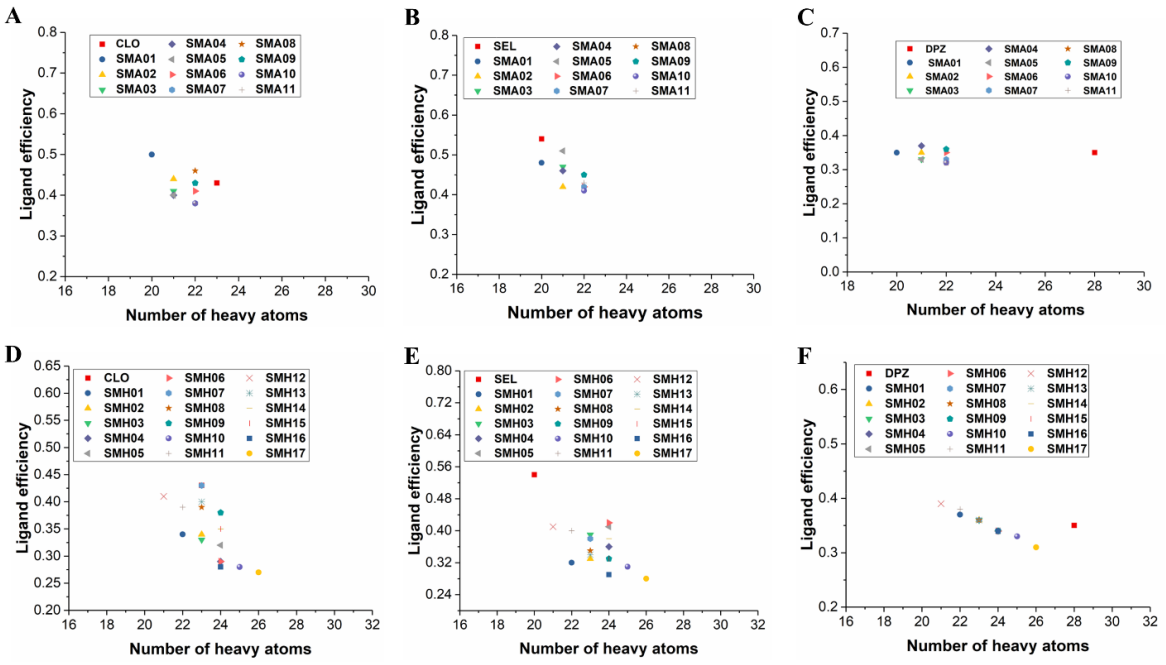

Figure 3.26. Ligand binding efficiency of compounds **SMA01-SMA11** and **SMH01-SMH17** along with standard inhibitors of MAO-A (Clorgyline), MAO-B (Selegiline) and AChE (Donepezil); A) ligand efficiency of compounds **SMA01-SMA11** against MAO-A; B) ligand efficiency of compounds **SMA01-SMA11** against MAO-B; C) ligand efficiency of compounds **SMA01-SMA11** against AChE; D) ligand efficiency of compounds **SMH01-SMH17** against MAO-A; E) ligand efficiency of compounds **SMH01-SMH17** against MAO-B; F) ligand efficiency of compounds **SMH01-SMH17** against AChE.

3.4.3.4. Predicted ADMET properties

To understand the pharmacokinetic profile of the synthesized series of compounds we have performed the prediction of ADMET properties. These properties provide us an insight into how these new molecules are going to behave in the living system. The predicted ADME properties are given in **Table 3.10** & **Table 3.11** while the predicted toxicity properties are presented in **Table 3.12 & Table 3.13**. Most of the compounds showed more than 95 % absorption from the human intestine which indicates good permeability through the intestinal wall. Caco2 cell permeability prediction shows that most of the compound falls in the moderate permeability range which indicates that all the compounds will easily pass through the epithelial barrier of the intestine. The compounds **SMA01**, **SMA03**, **SMA05**, **SMA06**, and **SMA10** shows moderate and rest of the compounds (**SMA02**, **SMA04**, **SMA07-SMA11**) showed low MDCK permeability. All compounds showed negative skin

permeability which means these compounds are not suitable for transdermal administration. Most of the compounds exhibited moderate BBB permeability except a few (**SMA01**, **SMA02** and **SMA05**). Compound **SMA09** showed a high degree of plasma protein binding while all other compounds showed moderate plasma binding. Furthermore, all the predicted compounds of the **SMA series** were non-inhibitors for CYP2C9, CYP2C19 and CYP3A4 enzymes whereas, most of the compounds of the **SMH series** were predicted as inhibitors of CYP2C9, CYP2C19, and CYP3A4 except compounds **SMH10** and **SMH15.**

Table 3.10. Predicted ADME parameters of compounds **SMA01-SMA11**

Compd. code	HIA (%)	Caco2	MDCK (nm/s)	SP (logKp, cm/h)	BBB	PPB (%)	CYP2C9	CYP2C19	CYP3A4
SMA01	95.49	48.81	219.563	-3.59	0.058	76.67	non	non	non
SMA02	95.49	48.47	22.890	-3.86	0.089	79.07	non	non	non
SMA03	95.68	36.80	77.537	-3.65	0.117	84.67	non	non	non
SMA04	95.93	34.04	0.310	-3.53	0.125	85.49	non	non	non
SMA05	95.51	49.45	114.238	3.53	0.085	81.43	non	non	non
SMA06	95.96	51.76	43.878	-3.73	0.113	73.31	non	non	non
SMA07	95.49	49.23	0.683	-3.99	0.120	82.90	non	non	non
SMA08	96.06	41.32	11.245	-3.58	0.216	87.08	non	non	non
SMA09	96.06	40.89	1.307	-3.57	0.247	90.28	non	non	non
SMA10	95.54	50.17	29.004	-3.46	0.139	84.85	non	non	non
SMA11	95.54	50.26	0.266	-3.42	0.134	82.70	non	non	Non

Table 3.11. Predicted ADME properties of compounds **SMH01-SMH17**

Comp. code	HIA (%)	Caco2	MDCK (nm/s)	SP (logKp, cm/h)	BBB	PPB (%)	CYP2C9	CYP2C19	CYP3A4
SMH01	95.97	33.951	278.224	-3.40	0.277	86.365	Inhibitor	Inhibitor	Inhibitor
SMH02	95.96	26.669	158.827	-3.41	0.267	88.030	Inhibitor	Inhibitor	Inhibitor
SMH03	95.96	24.844	170.838	-3.44	0.312	86.743	Inhibitor	Inhibitor	Inhibitor
SMH04	96.10	29.078	48.643	-3.34	0.198	88.775	Inhibitor	Inhibitor	Inhibitor
SMH05	96.10	28.783	68.938	-3.36	0.306	88.63	Inhibitor	Inhibitor	Inhibitor
SMH06	96.10	29.678	65.660	-3.33	0.274	89.03	Inhibitor	Inhibitor	Inhibitor
SMH07	92.86	21.600	57.111	-3.70	0.165	80.34	Inhibitor	Inhibitor	Inhibitor
SMH08	92.86	17.574	111.214	-3.73	0.181	81.18	Inhibitor	Inhibitor	Inhibitor
SMH09	96.36	36.013	170.960	-3.53	0.310	84.47	Inhibitor	Inhibitor	Inhibitor
SMH10	87.89	14.647	22.484	-3.33	0.123	89.36	non	non	non
SMH11	95.99	37.649	119.274	-3.38	0.147	84.03	Inhibitor	Inhibitor	Inhibitor
SMH12	95.99	33.675	20.377	-3.68	0.175	84.29	Inhibitor	Inhibitor	Inhibitor
SMH13	95.99	26.480	70.806	-3.42	0.160	86.10	Inhibitor	Inhibitor	Inhibitor
SMH14	96.08	25.843	0.267	-3.28	0.159	87.76	Inhibitor	Inhibitor	Inhibitor

SMH15	89.44	16.180	5.997	-3.30	0.117	88.04	non	non	non
SMH16	95.75	29.390	24.840	-3.98	0.191	71.12	Inhibitor	Inhibitor	Inhibitor
SMH17	94.36	24.700	217.547	-3.85	0.338	73.43	Inhibitor	Inhibitor	Inhibitor
E20	97.95	55.51	0.138	-3.04	0.187	84.61	non	non	Non
SAG	93.59	10.27	16.903	-3.11	0.134	89.45	non	non	inhibitor

HIA = Human intestinal absorption (%), Rule: 0-20 (poor), 20-70 (moderate) and 70-100 (well); **Caco2** = *In vitro* permeability of Caco2 cell (nm/s), Rule: <4 (low), 4-70 (moderate), >70 (high); **MDCK** = Maden Darby canine kidney cell permeability (nm/s), Rule: <25 (low), 25-500 (moderate), >500 (high); **SP**: *In vitro* skin permeability (cm/h); **BBB** = Blood-brain barrier permeability (C_{brain}/C_{blood}), Rule: <0.1 (low), 0.1-2.0 (moderate), >2.0 (High); **PPB** = *In vitro* plasma protein binding (%), Rule: <90 (moderate bound), >90 (strong bound); non = non inhibitor.

Furthermore, the mutagenicity test of synthesized compounds using the Ames test shows all compounds as mutagen. The carcinogenicity test in animals (mice and rats) is done to assess the tumorigenic potential of the compounds. The inhibitors are predicted as positive in the mouse carcinogenicity screen whereas in rat carcinogenicity all the compounds were predicted as negative. Additionally, the hERG test predicted that all compounds possess a medium risk to cardiac function. The predicted toxicity properties of all compounds are given in **Table 3.12** and **Table 3.13**.

Table 3.12. Predicted toxicity parameters of compounds **SMA01-SMA11**

Compd. code	Ames test	Carcinogenicity (Mouse)	Carcinogenicity (Rat)	hERG inhibition
SMA01	Mutagen	Positive	Negative	Medium risk
SMA02	Mutagen	Positive	Negative	Medium risk
SMA03	Mutagen	Positive	Negative	Medium risk
SMA04	Mutagen	Positive	Negative	Medium risk
SMA05	Mutagen	Positive	Negative	Medium risk
SMA06	Mutagen	Positive	Negative	Medium risk
SMA07	Mutagen	Positive	Negative	Medium risk
SMA08	Mutagen	Positive	Negative	Medium risk
SMA09	Mutagen	Positive	Negative	Medium risk
SMA10	Mutagen	Positive	Negative	Medium risk
SMA11	Mutagen	Positive	Negative	Medium risk

Table 3.13. Predicted toxicity properties of compounds **SMH01-SMH17**

Compd. Code	Ames test	Carcinogenicity (Mouse)	Carcinogenicity (Rat)	hERG inhibition
SMH01	mutagen	positive	negative	medium risk
SMH02	mutagen	positive	negative	medium risk
SMH03	mutagen	positive	negative	medium risk
SMH04	mutagen	positive	negative	medium risk
SMH05	mutagen	positive	negative	medium risk

SMH06	mutagen	positive	negative	medium risk
SMH07	mutagen	positive	negative	medium risk
SMH08	mutagen	negative	negative	medium risk
SMH09	mutagen	negative	negative	medium risk
SMH10	mutagen	negative	negative	medium risk
SMH11	mutagen	positive	negative	medium risk
SMH12	mutagen	positive	negative	medium risk
SMH13	mutagen	positive	negative	medium risk
SMH14	mutagen	positive	positive	medium risk
SMH15	mutagen	negative	negative	medium risk
SMH16	mutagen	positive	negative	medium risk
SMH17	mutagen	negative	negative	medium risk
E20	mutagen	negative	negative	medium risk
SAG	mutagen	positive	negative	medium risk

Ames test: Ames test for mutagenicity in Salmonella typhimurium, **Carcinogenicity (Mouse):** 2 years carcinogenicity bioassay in mouse, **Carcinogenicity (Rat):** 2 years carcinogenicity bioassay in rat, **hERG Inhibition:** *In Vitro* Human Ether-a-go-go Related Gene Channel Inhibition; **E20 =** Donepezil, **SAG** = Safinamide.

3.5. Summary

In summary, a set of 11 analogs of sesamol-derived O-acetamides (**SMA01-SMA11**) and 17 analogs (**SMH01-SMH17**) of sesamol-derived extended carbohydrazones were designed by employing a linker modification and molecular hybridization strategy from an in-house dual inhibitory lead molecule with an aim to improve MAO-B potency (**SMA series**) and investigate the role of the linker (**SMH series**) of resultant analogs. The molecular structure of synthesized compounds was confirmed through FTIR, ^{1}H, ^{13}C NMR spectroscopy and HRMS techniques. The synthesized library was evaluated against *in vitro* MAO-A, MAO-B and AChE enzymes. Compound **SMA08** was identified as the most potent MAO-A inhibitor (MAO-A IC_{50} = 0.053 ± 0.001 μM) while compound **SMA05** emerged as the most potent MAO-B inhibitor (MAO-B IC_{50} = 0.019 ± 0.001 μM) while compound **SMA04** exhibited highest activity towards AChE among all the tested compounds with IC_{50} value of 2.541 ± 0.120 μM. Compound **SMA09** emerged as most selective towards MAO-B and balance lead with multifunctional (MAO-A IC_{50} = 0.160 ± 0.009 μM, MAO-B IC_{50} = 0.071 ± 0.002 μM, AChE IC_{50} = 2.611 ± 0.086 μM and BChE IC_{50} = 4.223 ± 0.162 μM). BChE inhibition of compound **SMA09** was determined to

evaluate the selectivity of the molecule towards AChE. Compound **SMH07** emerged as the most potent MAO-A inhibitor (MAO-A IC_{50} = 0.076 ± 0.009 µM) among all the tested compounds while compound **SMH06** was identified as the most active MAO-B inhibitor (MAO-B IC_{50} = 0.064 ± 0.003 µM). Compound **SMH10** displayed the highest AChE inhibitory activity among all the tested compounds (AChE IC_{50} = 1.257 ± 0.001 µM). Compound **SMH06** emerged as the balanced lead multifunctional molecule (MAO-A IC_{50} = 11.145 ± 0.305 µM, MAO-B IC_{50} = 0.064 ± 0.003 µM, AChE IC_{50} = 1.555 ± 0.013 µM, BChE IC_{50} = 9.936 ± 0.105 µM). BChE inhibition of compound **SMH06** was performed to evaluate the selectivity of the compound towards AChE. Enzyme kinetics and time-dependent reversibility study revealed a competitive reversible nature of compound **SMA09** towards MAO-B while a competitive irreversible nature towards AChE whereas compound **SMH06** displayed mixed and reversible inhibition nature towards both enzymes. Furthermore**,** antioxidant and metal chelation studies of compounds **SMA09** and **SMH06** suggest moderate antioxidant activity and chelation of iron.

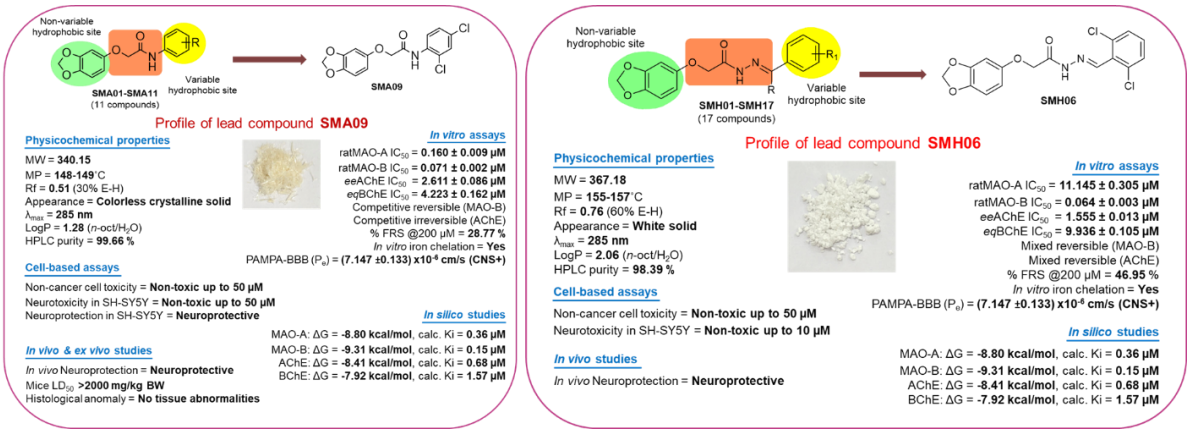

Figure 3.27. Summary of key outcomes from the **SMA** and **SMH series**

Additionally, a brain permeation study of compounds **SMA09** and **SMH06** indicates them as CNS+ molecules whereas *in cellulo* toxicity studies revealed that compound **SMA09** was non-toxic to fibroblast (L929) and neuroblastoma (SH-SY5Y) cells up to 50 µM concentration while compound **SMH06** was found as non-toxic to fibroblast up to 50 µM

and for neuroblastoma up to 10 µM. Moreover, compound **SMA09** displayed *in cellulo* and *in vivo* neuroprotection against dexamethasone-induced oxidative stress in cells and scopolamine-induced amnesia model in mice, respectively. Both compounds **SMA09** and **SMH06** produced *in vivo* neuroprotection against the scopolamine-induced amnesia model. The acute oral toxicity study suggests that compound **SMA09** was not toxic to animals up to a dose of 2000 mg/kg BW (**Figure 3.27**).